Karlsruhe Institute of Technology

Tobias Messer

On 3D Laser Printing Beyond the Common –

Compact Printers, Novel Materials, Special Applications

2023
Dissertation

On 3D Laser Printing Beyond the Common –

Compact Printers, Novel Materials, Special Applications

Zur Erlangung des akademischen Grades eines
DOKTORS DER NATURWISSENSCHAFTEN
von der KIT-Fakultät für Physik des
Karlsruher Instituts für Technologie (KIT)

genehmigte

DISSERTATION

von

M. Sc. Tobias Sebastian Messer
geboren in Öhringen

Tag der mündlichen Prüfung: 15. Dezember 2023
Referent: Prof. Dr. Martin Wegener
Korreferent: Prof. Dr. Eva Blasco

Contents

Publications

Parts of this thesis have already been published ...
... in scientific journals:

- R. Batchelor[†], T. Messer[†], M. Hippler, M. Wegener, C. Barner-Kowollik, and E. Blasco, "Two in One: Light as a Tool for 3D Printing and Erasing at the Microscale", *Adv. Mater.* **31**, 1904085 (2019).
- V. Hahn, T. Messer, N. M. Bojanowski, E. R. Curticean, I. Wacker, R. R. Schröder, E. Blasco, and M. Wegener, "Two-step absorption instead of two-photon absorption in 3D nanoprinting", *Nat. Photonics* **15**, 932-938 (2021).
- U. T. Sanli[†], T. Messer[†], M. Weigand, L. Lötgering, G. Schütz, M. Wegener, C. Kern, and K. Keskinbora, "High-Resolution Kinoform X-Ray Optics Printed via 405 nm 3D Laser Lithography", *Adv. Mater. Technol.* **7**, 2101695 (2022).
- T. Abele, T. Messer, K. Jahnke, M. Hippler, M. Bastmeyer, M. Wegener, and K. Göpfrich, "Two-Photon 3D Laser Printing Inside Synthetic Cells", *Adv. Mater.* **34**, 2106709 (2022).
- T. Messer, M. Hippe, J. Gao, A. Naber, and M. Wegener, "A shoe-box-sized 3D laser nanoprinter based on two-step absorption", *Light Adv. Man.* **5**, 269-276 (2024).

... in patent applications:

- V. Hahn, T. Messer, and M. Wegener "Photoresist Composition, System Comprising a Photoresist Composition, Method for Producing a Three-Dimensional Structure and Use of a Photoresist Composition in 3D-Printing", pat. 21 205 242.7 (Karlsruhe Institute of Technology).
- K. Göpfrich, T. Abele, K. Jahnke, T. Walther, M. Wegener, T. Messer, and M. Hippler "Method for Non-Invasive Production of Defined Structures Inside Compartements and Compartment", WO 2023/052442 (Max-Planck-Gesellschaft zur Förderung der Wissenschaften e.V. and Karlsruhe Institute of Technology, April 6, 2023).

[†] These authors contributed equally.

... at scientific conferences (only own oral presentations):

- T. Messer, R. Batchelor, M. Hippler, C. Barner-Kowollik, M. Wegener, and E. Blasco "Light as a Tool for 3D Additive and Subtractive Manufacturing on the Microscale – With a Single Photoresist", SPIE Photonics West, United States of America, San Fransisco, February 2020.
- T. Messer, M. Blaicher, M. Thiel, and M. Wegener "Two Steps Towards Compact 3D Laser Nanoprinters" (invited talk), SPIE Photonics West, United States of America, San Fransisco, February 2023.

ADDITIONAL RELATED WORK HAS ALREADY BEEN PUBLISHED ...
... in scientific journals:

- N. M. Bojanowski, A. Vranic, V. Hahn, P. Rietz, T. Messer, J. Brückel, C. Barner-Kowollik, E. Blasco, S. Bräse, and M. Wegener, "Search for Alternative Two-Step-Absorption Photoinitiators for 3D Laser Nanoprinting", *Adv. Funct. Mater.* **33**, 2212482 (2022).
- A. Mauri, P. Kiefer, P. Neidinger, T. Messer, N. M. Bojanowski, L. Yang, S. Walden, A.-N. Unterreiner, C. Barner-Kowollik, M. Wegener, W. Wenzel, and M. Kozlowska, "Two-and three-photon processes during photopolymerization in 3D laser printing", *Chem. Sci.* **15**, 12695-12709 (2024).
- S. Braun, R. Zvagelsky, T. Messer, M. Holsten, P. Kollenz, A. de la Cruz Garcia, C. Selhuber-Unkel, M. Mastalerz, J. Freudenberg, M. Wegener, and U. H. F. Bunz, "Vinylcyclopropane Inks for Direct Laser Writing: Shrinkage Reduction", in preparation.

Chapter 1

1 Introduction

3D laser (micro- and nano-)printing, 3D laser lithography, direct laser writing, multi-photon polymerization – nowadays, there are various terms for the three-dimensional manufacturing of microstructures employing a tightly-focused beam of light. While the nomenclatures often changed over the years, and still are not uniformly used, something else remained very constant instead: the general setup of a corresponding 3D laser printer.

Already during the '17th Congress of the International Commission for Optics: Optics for Science and New Technology' in Taejon, Republic of Korea back in August 1996, Shoji Maruo presented a first setup with a drawing under the naming 'Three-dimensional microfabrication with two-photon absorbed photopolymerization' [1]. Together with his Optics Letters publication with co-workers in 1997 under the same title [2], this is often stated as the birth of this novel lithographic process exceeding the micropatterning under UV illumination which was state-of-the-art back in the time.

The system they describe still serves as the basis of the vast majority of 3D laser printers and is consisting of the following components: First a mode-locked, femtosecond-pulsed Ti:Sapphire laser as a light source, set to an oscillation wavelength of 790 nm. Second, a computer-controlled shutter followed by a lens system for beam expansion. Finally, the laser beam is focused into a liquid 'UV photopolymerizing resin' by an objective lens with a numerical aperture of NA $= 0.85$. For three-dimensional fabrication, their sample is mounted on a computer-controlled 3D scanning stage and can be observed during printing with a camera system. Even their described resist system comprised of acrylatic monomers with an additional photoinitiator is today's standard [3, 4]. Thus, I would refer to such a system as the common printer, common resist, and standard excitation mechanism for today's 3D laser printing.

Of course, huge advancements were reached throughout the years for example in terms of the achievable print speeds [5] and especially the huge amount of applicable materials [3, 4]. These developments together with the intrinsic potential of the two-photon process to directly create almost arbitrary three-dimensional structures led 'three-dimensional microfabrication with two-photon

absorbed photopolymerization' become one of the most versatile techniques in micro- and nanoscale additive manufacturing nowadays. Therefore, an immense amount of applications emerged, ranging from optics and photonics across biology to mechanics and especially metamaterials [6–8]. Even conductive and stimuli-responsive materials are readily usable [9, 10].

In contrast, only comparative minor advancements could be made in regard to other characteristics. For example, the reported first experiments show high-aspect-ratio line structures with a feature size of 500 nm and a minimum pitch, hence resolution, of 800 nm [11]. Within thirty years of progress, the resolution has not even been surpassed by a factor of 10 [12], which is explained by the fundamental limitation of optical resolution by the diffraction limit due to the wave nature of light. Even by employing approaches from high-resolution microscopy such as stimulated-emission depletion (STED), which theoretically should enable unlimited resolution, the latter remains stuck above a range of 100 nm [13–15].

Besides the minor advancements in resolution, the capability of the reverse process – to erase material again, i. e. subtractive manufacturing – as a two-photon induced photochemical process was sparsely investigated throughout the years. Here, most research focused on the laser induced but thermally activated ablation mechanism [16]. Yet, merging light-induced additive and subtractive three-dimensional microfabrication is of great interest. However, different requirements on the setup usually hinder a simultaneous approach which led to the general understanding that the processes are 'incompatible with each other' [17].

For two-photon-based additive manufacturing, the setups were highly optimized and even commercialized resulting in consumer-friendly, nearly plug-and-play devices [18–20]. This, of course, tremendously pushed 3D laser printing since also non-specialists without detailed expertise on optics and physics can utilize it to facilitate research in other fields for example biology or material science. Still, further democratization, similar to the enormous success of filament-based extrusion printing or stereolithographic printing during the last decade, is limited due to the high costs and big size of the devices. It remains interesting, why reaching smaller scales is always coming along with large devices, independent of whether in terms of microscopy with large scanning electron microscopes or as in our case in terms of nanostructuring, as I discussed with my colleague Vincent Hahn often.

Therefore, the aim of this thesis is to investigate some of the open questions going *beyond* the common and widely used 3D laser printing. In more detail, a competing excitation mechanism to standard two-photon excitation is found, which enables compact 3D laser printers. The achievable level of compactness and simultaneous cost reduction is studied. Second, a novel resist system is studied in regard to merging two-photon-induced additive and subtractive manufacturing. Third, a special application is researched on: delicate structures requiring high-resolution 3D laser printing beyond the standard.

Outline of this thesis

In chapter 2, I will start with describing common 3D laser printing. Here, a state-of-the-art printer is presented in detail, as well as the general workflow. Further, common materials and the underlying two-photon excitation mechanism are explained along important models for 3D laser printing. The chapter concludes with discussions on the resolution in 3D laser printing together with its limitations, common applications, and open challenges.

The remainder of this thesis is split into three parts. Part I covers the topic of compact 3D laser printers. In chapter 3, I will present two-step absorption as an alternative excitation mechanism to two-photon absorption. I will discuss important characteristics like the effective nonlinearity and their resulting current limitations of two-step-absorption-based 3D printing in theory and present the photoinitiator benzil as a real system. Based on this, chapter 4 will cover the approach of building a shoe-box-sized 3D laser printer, to proof that the need of large and expensive devices in 3D laser printing can be overcome. To this end, the implementation of a compact optical setup as well as a compact control unit will be shown. The chapter, and thereby the first part of my thesis, will conclude with performance tests of the realized printer and an analysis of the achievable resolution.

Part II will seize the topic of novel materials. While also all other chapters cover beyond-standard materials to fulfill special purposes, the research conducted in chapter 5 directly focuses on the material itself. Here, I will present our novel material which enables merging two-photon-based additive and subtractive manufacturing. I will start with experiments to verify the 3D laser printability of the material. Then, one-photon cleaving experiments are shown as a proof of concept and experiments employing two-photon cleaving reveal the full spatial control of the cleaving process.

Finally, Part III will briefly handle a special application. In chapter 6, I will summarize the printing of high-resolution kinoform lenses for x-ray applications. Here, the exploitation of a reduced wavelength for two-photon-based 3D laser printing leads to an improved manufacturing in comparison to previous work on 3D printing such lenses.

In chapter 7, I will conclude my thesis with a summary of the achievements and an outlook for future challenges and developments.

Chapter 2

2 Fundamentals – Common 3D Laser Printing

In this chapter, I will introduce the concepts of common 3D laser printing. First, I will explain a state-of-the-art 3D laser printer and its crucial components. After discussing standard material systems, I will introduce two-photon absorption as the underlaying excitation mechanism. Finally, discussions about the general workflow and common challenges will conclude this part.

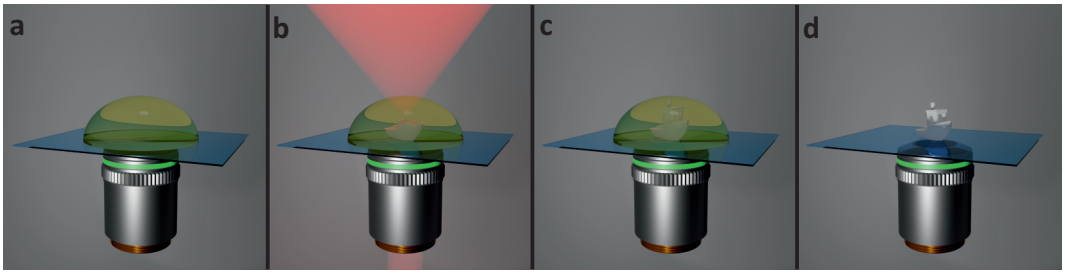

Figure 2.1: **Generalized workflow of 3D laser printing.** Starting with a reservoir of liquid photoresist (**a**), a laser is tightly focused to induce a polymerization reaction in the vicinity of the focus (**b**). Scanning desired three-dimensional trajectories allow for fabrication of almost arbitrary 3D structures (**c**). A final development step removes the unpolymerized material (**d**).

2.1 A State-of-the-Art 3D Laser Printer

High-resolution 3D laser printing is a versatile technology in 3D micro- and nanofabrication. To reach high precision at fast print speeds is demanding. Therefore, highly engineered devices are employed. Independent of whether they are home-built or commercial systems, they comprise the same fundamental architecture [4]. Here, we will put emphasis on focus scanning 3D laser printers only, although huge effort is also made in the field of projection based volumetric 3D laser printing [21–26]. However, they slightly differ in some of the crucial elements due to the different working principle. Thus, I will refer to the focus scanning based approach and its corresponding setup when using the term 3D laser printing and 3D laser printer, respectively, throughout this thesis.

The general workflow in short is shown in Figure 2.1 and is as follows: In focus scanning 3D laser printing, a laser beam is tightly focused into a reservoir of photoresist. At the focal position, a chemical reaction is induced and the material is polymerized. To obtain three-dimensional structures, focus and sample need to be scanned against each other along desired trajectories. Finally, the sample is developed and the printed structure remains. Further details on this workflow will be given in the following sections.

For such 3D laser printer, we identify five major components being crucial for the overall performance: light source, power modulation, focusing unit, scan unit, and control unit. A schematic of a very basic state-of-the-art 3D laser printer is shown in Figure 2.2. Of course, it comprises further elements like lenses or mirrors that are needed in the optical printing setup. In addition, components to enable or change certain properties of the printer and ease the handling are often added especially in home-built setups. However, they are not fundamental. In the following, we will discuss the mentioned five major components in more detail.

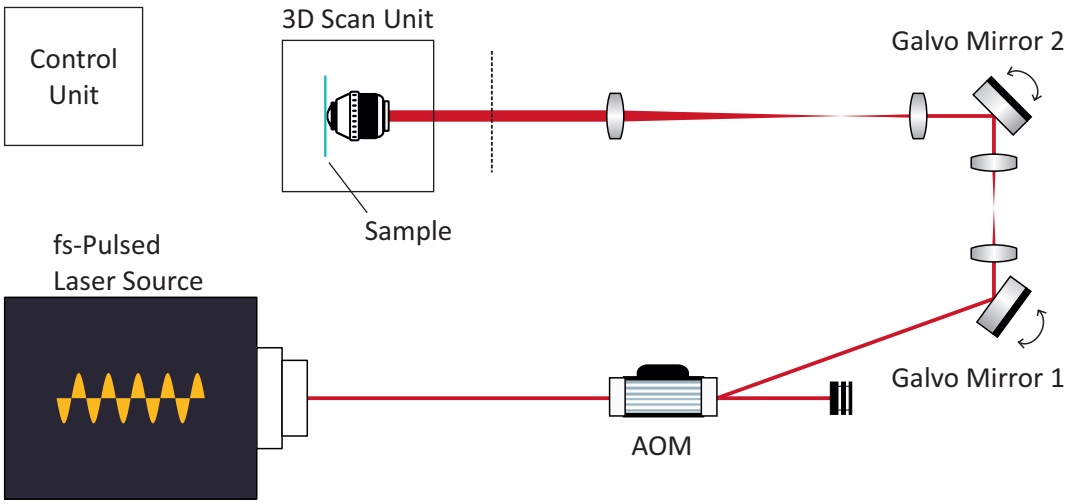

Figure 2.2: **Schematic of a very basic state-of-the-art 3D laser printer.** The five major components light source, power modulation, focusing unit, scan unit, and control unit are shown. Here, an AOM is shown as it is most often used for power modulation. Further, both possible solutions for the scan unit are depicted with galvo scanners for beam scanning and a 3D scanning stage to move the sample and or the objective lens. As explained in the main text, also different configurations for example with fixed mirrors are conceivable.

Light Source

Femtosecond-pulsed lasers are the standard light source in 3D laser printers [27]. Picosecond-pulsed lasers are reported to work as well [28]. Most often, Ti:Sapphire laser oscillators are used. They produce pulse widths of $70 - 140$ fs at a repetition rate of 80 MHz in the red and near-infrared. A typical average power is around $3 - 4$ W at 800 nm wavelength [29, 30]. Therefore, they offer high peak intensities in combination with a high spatial mode of the beam. One main advantage of Ti:Sapphire oscillators is their ability for tuning the output wavelength. This adds flexibility to the 3D laser printer, since different materials may require different wavelengths for processing.

However, a drawback of such femtosecond-pulsed lasers is their cost and their size (see Figure 2.3). In fact, with a cost of around 100 000 Euros they are more than an order of magnitude more expensive than the second most expensive part, the often used microscope body or the objective lens. Taken all parts (laser head, electronics, and chiller) together, they also take up a considerably large space.

There are alternative options with a fixed wavelength being more compact and less expensive. However, they also come at a significantly lower average output power. Commercial systems for example use 780 nm (Nanoscribe, Femtika, UpNano) [18–20] or 515 nm (Femtika) [19] usually. Still, the femtosecond-pulsed

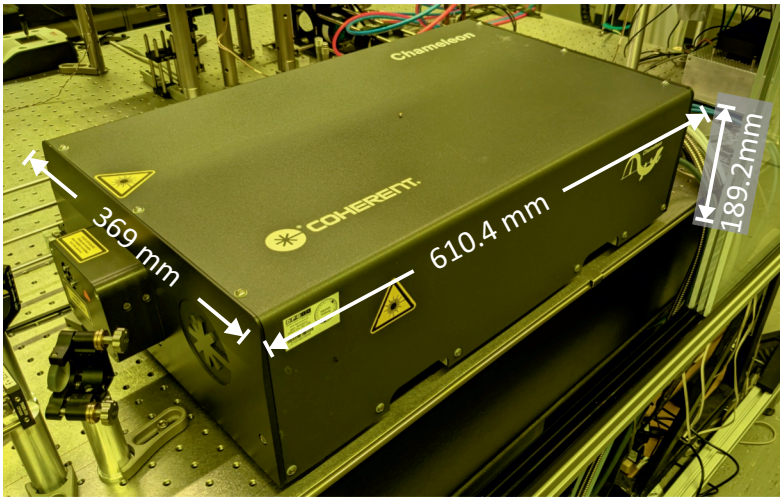

Figure 2.3: **Photograph of a Ti:Sapphire laser oscillator.** These high-power, femtosecond-pulsed laser sources are state-of-the-art in home-built 3D laser printing setups. The image shows the laser oscillator but does not show the additional control and cooling unit.

lasers in general strongly limit the minimum cost and size of a 3D laser printer.

Power Modulation

During 3D laser printing, the output power has to be modulated. First, it has to be switched on and off after every printed trajectory. At high print speeds, this switching must be adequately fast. For example, printing 5 µm lines with a common print speed of a commercial system of $0.4\,\mathrm{m\,s^{-1}}$ [5] results in a required modulation frequency of 125 kHz. At the same time, a modulation of the output power between on and off is highly desirable for matching print speed and output power to the specific structure. Thus, acousto-optic (see Figure 2.4) or electro-optic modulators are employed instead of slow mechanical binary shutters. They both can easily get to modulation frequencies in the range of 100 MHz.

Acousto-optic modulators exploit the density fluctuations of a crystal under influence of a standing acoustic wave. These form a diffraction lattice for the input beam resulting in a general diffraction pattern. Since the zeroth order is always present, it is blocked and only the first order beam is used. Differently, electro-optic modulators impose the modulation on either amplitude, frequency, phase, or polarization of the beam. Here, local electric fields are applied to crystals whose refractive index is dependent on the strength of these fields.

Focusing Unit

For high-resolution 3D laser printing, the laser beam needs to be tightly focused into the photoresist. The resulting minimal polymerizable volume is referred to as

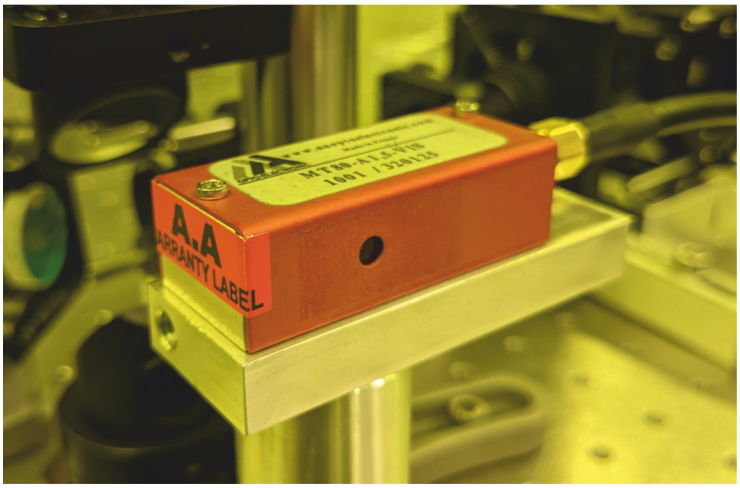

Figure 2.4: **Photograph of an acousto-optic modulator.** Due to their high modulation frequency, they are often employed as high-speed shutters and for power modulation in 3D laser printers. Alternatively, electro-optic modulators can be utilized.

a voxel. Here, microscope objective lenses with a high numerical aperture (NA) are widely used. To obtain highest resolution with a diffraction limited focus, 100 × / NA 1.4 objective lenses are employed [12, 13, 31]. In turn, the capability of exploiting 3D laser printing with low-NA objective lenses down to NA = 0.16 was shown using a 5 × / NA 0.16 objective lens recently [32]. This comes along with a larger focus, thus, a lowered resolution which is well acceptable for many applications. The change of the focus size with changing numerical aperture is shown in panel **a** of Figure 2.5. A more detailed discussion concerning this matter will follow in section 2.7 when dealing with the resolution of 3D laser printing.

However, the limitation for 3D laser printing is that the voxel needs to be smaller than the minimum feature size of the desired structure. Of course, the smaller the voxel is compared to the smallest feature, the smoother the feature can be reproduced, increasing the manufacturing time in turn. Thus, objective lenses with higher NA lead to less layering or staircasing artifacts in multi-layer structures, hence, smoother surfaces. Another way to circumvent the staircasing is the so-called *grayscale lithography* [34, 35]. Here, the voxel size is steadily adapted during printing by a variable beam expander for example [27]. In general, best focusing conditions of the objective lens are met when the entrance pupil of the objective lens is overfilled to achieve homogeneous illumination [36].

Another important prerequisite on the objective lens is a minimized field curvature. The larger the field curvature the higher the variance of the axial focus point over different positions within the field of view of the objective lens. Hence, the printing plane would be curved. Therefore, objective lenses with flat-field correction such as plan apochromats are usually employed.

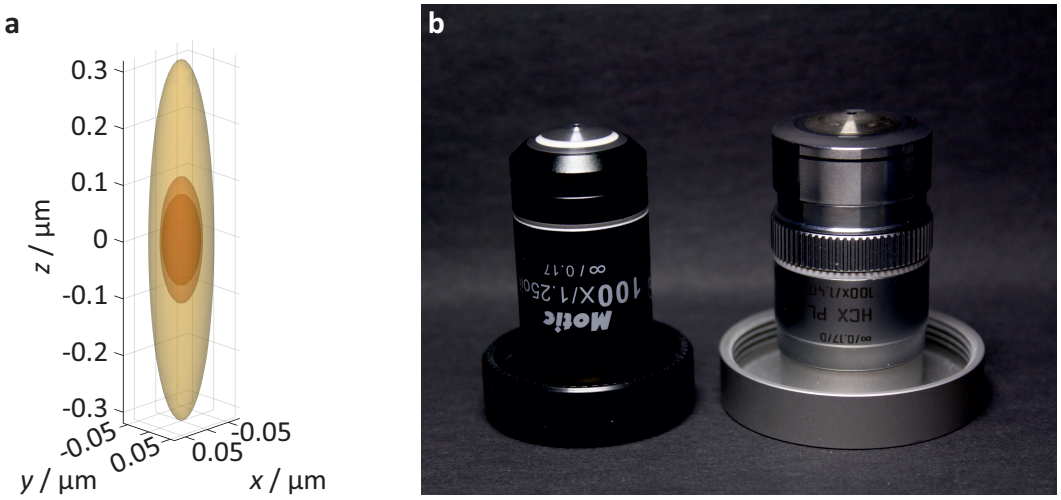

Figure 2.5: **Plot of calculated iso-intensity surfaces for three objective lenses: 100 × / NA 1.4, 100 × / NA 1.25, and 25 × / NA 0.8 (a) and photograph of two objective lenses used within this thesis (b). a** The vectorial field distribution in the focal region is calculated along the lines of van de Nes et al. [33] and further converted into the corresponding intensity distribution. The plot shows iso-intensity surfaces at the same intensity. The difference solely comes from the change in the numerical aperture. The smallest voxel is achieved by the highest NA with NA = 1.4. A difference to the slightly smaller NA of NA = 1.25 is visible but not very pronounced compared to the much larger voxel resulting with NA = 0.8. Note that the effect is by far stronger in axial (z) direction compared to the lateral direction. **b** Photograph of a 100 × / NA 1.25 (left) and 100 × / NA 1.4 (right) objective lens.

Scan Unit

One of the most important parts of a focus scanning 3D laser printer is the scan unit. In general, the focus position of the laser and the sample need to be moved against each other. There are three major principles for that: scanning the laser beam while fixing the sample position, scanning the sample position while fixing the laser beam, or a superposition of both. Each of the principles allows for different implementations itself.

We start with discussing **scanning the sample position with a fixed laser beam**. This approach allows for the simplest 3D laser printing setup. In fact, such a setup could comprise as little as a laser, an acousto-optic modulator, an objective lens, a 3D-movable stage, and two lenses for beam expansion in front of the objective lens. Even less corrected objective lenses could be employed, since the focus position would be fixed. Field curvature, for example, would be meaningless due to the fixed focus position. At the same time, the size of the printed structure is not limited to the field of view of the objective lens but to the travel range of the stage which usually is much larger. Therefore, they are often used in 3D laser printers.

Different types of actuation are possible. General requirements for the applicability of a stage are minimum step size, repeatability, maximum velocity, maximum acceleration, settling time, and travel range. Starting at the rear end of precision, motorized stages with simple **stepper motors** break the ground. They usually allow for large travel ranges far in the centimeter range. In turn, they are comparably slow on a small scale and barely get below 1 µm with the minimum step size. This is too coarse for normal 3D laser printing applications.

A second kind are **voice coil actuators**. Here, a magnet and coil assembly is employed to generate a linear displacement dependent on the current through the coil. In the bachelor thesis of Julian Haarer which was supervised by me, we investigated this effect in a home-built linear stage. Crucial is the accuracy of setting the current connected with the position feedback loop from an encoder. Commercial systems allow for high-speed positioning with an accuracy of tens of nanometers. Travel ranges in the low centimeter range are possible at that precision. However, they are mostly implemented in linear instead of three-dimensional stages.

The highest precision is reached for **piezoelectric actuators**. They utilize the converse piezoelectric effect, where an electric field is applied to a suitable crystal causing a mechanical deformation [37]. Minimum step sizes in the single-digit nanometer range are well attainable. However, the possible deformation at reasonable voltages is limited to the micrometer scale. Thus, stacks of crystals are common. For large travel ranges on the millimeter scale, additional techniques like the slip-stick or walk-drive principles are applied [38]. This opens up the possibility of adopting piezoelectric stages for 3D laser printing.

While especially the piezoelectric actuated stages reach the required precision and large travel ranges are possible, all stage types suffer from the same drawback: most often they are bulky. Figure 2.6 shows three commonly used scan units next to each other for size comparison. Here, the size of the bulky scanning stage on the right vastly overexceeds the size of the movable mirrors employed in the alternative method of scanning the laser beam with a fixed sample position. Besides the size disadvantage, the scanning stages usually are also vulnerable to internal vibrations, and possible print speeds are rather slow. The latter is not surprising due to inertia, since a comparably high weight has to be accelerated all the time. Instead, when **scanning the laser beam with a fixed sample position**, the moved mass reduces to the mass of the movable mirror. In principle, almost infinite scan speeds can be achieved since only the angle passed per time unit is limited and the scan speed further depends on the imaging of the mirror onto the lens.

Commonly, **galvanometric mirrors** are used. They allow for extremely fast angular changes and a high accuracy. However, they are only rotatable around a single axis. Therefore, two mirrors are needed for scanning a 2D plane. Since the

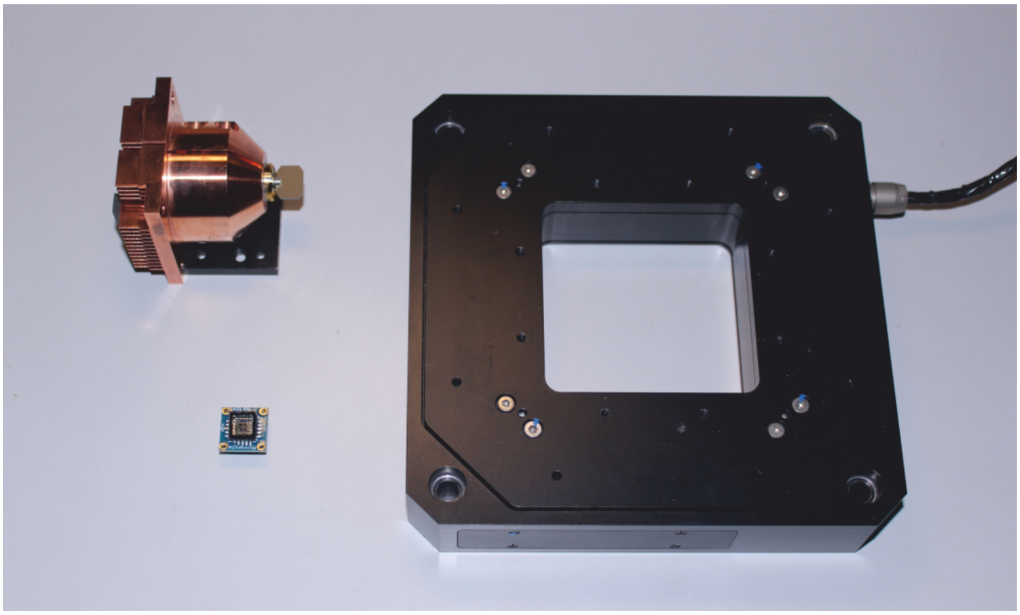

Figure 2.6: **Photograph of three common scan units.** On the right, a 3D piezoelectric scan stage with the dimensions of $15 \times 15 \times 3\,\mathrm{cm}^3$ is placed as a standard solution for the sample scanning method. On the upper left, a galvanometric mirror with its cooling unit is positioned. Note, that the movable mirror itself is only the small reflecting part designed for a 6 mm beam right of the larger copper unit. Finally, the lower left side shows a two-axes micro-electro-mechanical-system (MEMS) scanner. Again, the actual movable mirror is only a small part of the overall visible small component. With its size of around 1 mm it is barely visible in this size comparison photograph.

mirror plane has to be perfectly imaged onto the entrance pupil of the objective lens for wobble-free scanning in the focal plane, utilizing two mirrors enhances the complexity of the optical setup. To be more specific, the plane of the first movable mirror for one axis has to be imaged onto the second mirror which then again has to be imaged onto the objective lens.

An alternative are two-dimensional tiltable mirrors. They are realized in so-called two-axes micro-electro-mechanical-system (MEMS) scanners. **MEMS scanners** are small mirrors connected to electrostatic actuators for tilting in x- and y-direction simultaneously. This enables a simpler optical setup as compared to the two galvanometric mirrors. In the bachelor thesis of Philipp Ohl, which I supervised, we examined the capabilities of such a scanner for a 3D laser printer. Due to the small power consumption the MEMS scanner exhibit, our special interest was to check the possibility of controlling the MEMS scanner by a microcontroller. In this scope, Andreas Naber helped out with his knowledge by setting up the code for the microcontroller. It is a delicate work since output values have to be given at a high frequency and especially syncronization on the microcontroller

is much more complicated than using a normal lab computer. Parts of the code had to be written in assembler therefore. With this program, steering of a MEMS scanner via a microcontroller was successfully proven. However, the maximum rotation speed of the MEMS scanner is smaller than for galvanometric mirrors. In addition, the mirror diameter is in the low single-digit millimeter range requiring a small beam diameter upfront.

Both applications employing the scanning of light are purely two-dimensional. Thus, an additional stage for the third dimension in axial direction is compulsory for 3D laser printing. Most often, the objective lens is mounted on a linear translation stage in such a case. The movement of the objective lens in axial direction negates the perfect imaging of the mirror onto the entrance pupil though. Yet, the influence is not too severe if the movement is in the micrometer range only.

In addition, by scanning the laser beam, the structure size is limited to the field of view of the objective lens. Therefore, most often a **superposition** of scanning the laser beam and scanning the sample position is found in a 3D laser printer taking the advantages of both principles. Hence, the laser beam is scanned for fast printing on a small scale and a coarse stage helps stitching multiple print fields together to a larger structure. Other 3D laser printers attempt to synchronize coarse linear stages with a large scan range and fast scanning of galvanometric mirrors [39].

Control Unit

All electronic components need to be controlled and synchronized. Usually, it is a rack full of controllers. The main question is which component serves as master for the 3D laser printer. Some high precision stages come along with highly specialized controllers. They allow for setting certain parameters but remain a black box regarding the actual processing of input data. Moreover, their interface to a computer very often is a special software. Thus, setting up a main program for the 3D laser printer is not as easy with such devices.

Instead, it is desired to have high control about the system and processes. Therefore, usually a lab computer acts as the master and communicates with all other controllers of the single components. It performs as much of the data conversion as possible and delivers final output values and corresponding triggers. If possible even via analog signals. Mostly, this communication is implemented via data acquisition devices.

2.2 General 3D Laser Printing Workflow

While the core element – the 3D printing itself – and its involved components was just explained, the procedures upfront and afterwards should briefly be treated as well. Before the actual lithographic process, the structure to be printed has to be created and converted into a job file for the respective 3D laser printer. Most home-built printers use easy coded job files where all trajectories that comprise the structure are split into points. These points are then added to the job file as a list of *xyz*-coordinates. A header in the job file allows for setting specific parameters such as laser power and print speed.

The trajectories of the structure can be generated in different ways. In case of simple structures, they are most often hard coded via MATLAB (MathWorks) or the like. Otherwise, more complicated structures are usually generated as .stl-files. However, the .stl-files need additional processing and cannot be directly used. Here, common commercial software for 3D printers such as DeScribe (Nanoscribe GmbH) can be employed to cut the 3D model into slices which then again get hatched into lines with the desired slicing and hatching distances, respectively. These ordinarily match the requirements for the 3D laser printer and the structure can be manufactured by solidifying a liquid resist in a polymerization reaction [40] as will be described in more detail in the next sections.

Most often, the structures are printed on glass substrates. Due to their optical transparency in the visible range, they allow for printing on the far side of the objective lens. Alternatively, the structures can be fabricated in so-called *dip-in* mode [41], or in a sandwich-like configuration [42]. The choice for the right configuration usually is governed by the exact resist composition to not damage the objective lens, the desired height of the structure, and the index matching of the resist. The resist aspects will be revisited later in this chapter.

Finally, after successful printing, the structure is developed. In case of 3D laser printing this means that the substrate is immersed in solvent to dissolve the non-polymerized resist. Subsequently, special treatments like critical point drying can follow in case of delicate structures. Afterwards, the final 3D structure is achieved and can be checked by optical or scanning electron microscopy, or further reviewed for special properties.

2.3 Common Materials for 3D Laser Printing

3D laser printing works with photoresists. As its name implies, these are substances that undergo a chemical reaction under illumination with light. In general, there are two types of photoresists: negative tone and positive tone photoresists. They differ in their underlying chemical mechanism. Negative tone photoresists consist of small monomers which crosslink and form larger polymer networks

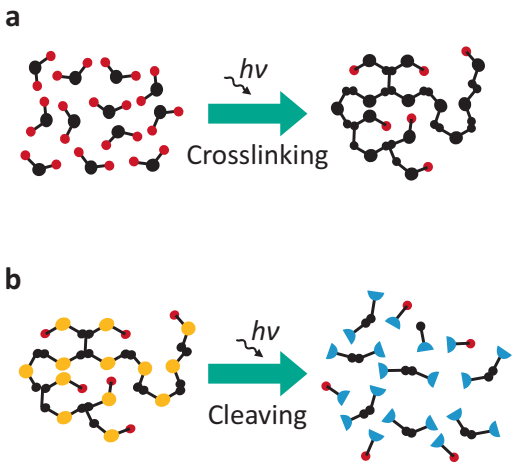

Figure 2.7: **Schematics of the reaction mechanisms of negative tone (a) and positive tone photoresists (b).** **a** Negative tone photoresists consist of small molecules with a center motif (black) and reactive units (red). Under light exposure they crosslink to a dense polymer network. **b** In contrast, positive tone photoresists are large molecules with photolabile groups (yellow) incorporated. Under irradiation with light, they break into small fragments.

when exposed with light. In contrast, positive tone photoresists comprise large polymeric chains which break into smaller molecules during exposure. More common in 3D laser printing are negative tone photoresists [43]. A scheme of both mechanisms is shown in Figure 2.7.

2.3.1 *Negative Tone Photoresist*

In principle, one can break down negative tone photoresists into two components [44]. First, a monomer is required. Monomers are small molecules which can be crosslinked to a dense polymer network. For that, reactive groups are required in the monomer structure. Typical reactive groups are acrylates, thiols, vinyls, or acrylamides [45]. They are all capable for radical polymerization and usually liquid or highly viscous at standard conditions. A single reactive group, however, only allows for linear chain growth. Thus, for the required dense polymer network in 3D laser printing at least bifunctional monomers are required. Most often, even monomers with three or four reactive units are employed. In addition, mixtures of monomers can be used to trigger the final properties of the material. Here, even monofunctional monomers can be added. Examples for widely used acrylatic monomers are pentaerythritol triacrylate (PETA), pentaerythritol tetraacrylate (PETTA), trimethylolpropane triacrylate (TMPTA), or polyethylene glycol diacrylate (PEGDA).

A second group of monomers is based on cationic polymerization [46]. These are most often epoxy-based or vinyl ethers. Similar to the first group, they undergo a chain growth transferring a charge from monomer to monomer instead of a free radical. For epoxy-based systems, this chain growth involves a ring opening of the previously protonated epoxy group. But, polymerization does not take place

upon light exposure but only a photoacid is generated. The polymerization itself is triggered by a subsequent heating process, the so-called *postexposure bake* [47]. A typical example for such monomers is SU 8 [48].

Furthermore, hybrid materials can be used as monomers [49] as well as hydrogels [50], metals [51, 52], and fused silica [53] are employed in 3D laser printing beyond normal monomers. However, all these systems are not very sensitive for excitation in the used wavelength range themselves. Therefore, a second component is required in the photoresist to absorb the light and trigger the polymerization reaction. These molecules are called photoinitiators. Usually, they are solid. Good photoinitiators have a high absorption at the desired wavelength. Once excited, they are prone to undergo a bond-cleavage reaction and break into free radicals or built a photoacid. These Initiators (I) trigger the respective chain-growth reaction employing the reactive groups of the monomer (M). The general chain-growth mechanism includes three steps as explained exemplary for the radical chain-growth [54, 55]:

Initiation:	$\mathrm{I} \xrightarrow{h\nu} \mathrm{I}^* \longrightarrow 2\,\mathrm{R}^\bullet$	
	$\mathrm{R}^\bullet + \mathrm{M} \longrightarrow \mathrm{RM}^\bullet$	
Propagation:	$\mathrm{RM}^\bullet + \mathrm{M} \longrightarrow \mathrm{R(M)_2}^\bullet$	
	$\mathrm{R(M)}_n{}^\bullet + \mathrm{M} \longrightarrow \mathrm{R(M)}_{n+1}{}^\bullet$	
Termination:	$\mathrm{R}^\bullet + \mathrm{R}^\bullet \longrightarrow \mathrm{RR}$	(Recombination)
	$\mathrm{R(M)}_n{}^\bullet + \mathrm{R}^\bullet \longrightarrow \mathrm{R(M)}_n\mathrm{R}$	
	$\mathrm{R(M)}_n{}^\bullet + \mathrm{R(M)}_m{}^\bullet \longrightarrow \mathrm{R(M)}_{n+m}\mathrm{R}$	
	$\mathrm{R(M)}_n{}^\bullet + \mathrm{R(M)}_m{}^\bullet \longrightarrow \mathrm{R(M)}_n + \mathrm{R(M)}_m$	(Disproportionation)
	$\mathrm{R(M)}_n{}^\bullet + \mathrm{X} \longrightarrow \mathrm{R(M)}_n\mathrm{X}^\bullet$	(Incorporation)
	$\mathrm{R(M)}_n{}^\bullet + \mathrm{X} \longrightarrow \mathrm{R(M)}_n + \mathrm{X}^\bullet$	(Transfer)

The initiation describes the dissociation of the photoinitiator molecule (I) after optical excitation (I^*) into two free radicals $R^\bullet$. Each radical can break a bond of the reactive group of the monomer (M) and attach to it while the monomer remains with an unpaired electron. During propagation, further monomer molecules react with the previous chain, increasing the number of repeating units. The chain-growth reaction is typically extremely fast. The formation of chains with more than thousand repeating units within milliseconds are reported for some polymers [56]. The average number of monomers reacting with a single active center from initiation to termination is defined as kinetic chain length [57]. In contrast, the degree of polymerization additionally takes termination into account referring to the total number of monomeric units in a polymer network [56].

The termination removes the active center off the corresponding chain in different possible reactions: The two main termination reactions are radical-radical recombination and disproportionation [56]. For recombination, two molecules with active center react with each other by pairing the two respective unpaired electrons to form a covalent bond. These active molecules could be the initial radicals or any active chain. As a result, the previously two molecules form a new single molecule. In contrast, disproportionation does not merge the two original active molecules but involves a hydrogen atom transfer between the two. Thus, the resulting products remain unchanged in length, while being no longer free radicals.

Furthermore, termination can include additional species X. Here, the active chain takes an atom like Hydrogen of an inactive molecule to remain inactive itself afterwards. Instead, the second molecule acts as a new active center. There are two general routes: incorporation of the additive or chain transfer. Both pathways themselves are two-fold depending on the properties of the involved species. The newly generated radical $X^{\bullet}$ can either be highly reactive or stable [58]. The latter may yield to inhibition. A widely known example for inhibition is the bi-molecular reaction with molecular oxygen under the formation of a peroxy radical [59]

$$\mathrm{R(M)}_n{}^{\bullet} + \mathrm{O_2} \longrightarrow \mathrm{R(M)}_n\mathrm{OO}^{\bullet}\,.$$

The resulting peroxy radicals tend to readily terminate via recombination or disproportionation and are less prone to re-initiate a polymerization reaction [60]. Moreover, the inhibition reaction involving oxygen is extremely fast, such that during light exposure while 3D laser printing, the chain-growth initiation and propagation are highly suppressed until all oxygen molecules are consumed locally [59]. While oxygen is ubiquitous, additional inhibitors can be added to the photoresist to suppress certain unwanted side reactions as we will discuss later in subsection 3.4.3. They are usually referred to as quenchers or scavengers. In turn, the properties of inhibitor-free photoresists is experimentally investigated. While the polymerization threshold (see section 2.5) decreases, the missing scavenger molecules lead to a loss in resolution and controllability [61, 62].

The second pathway with external species X is the chain transfer reaction. Again, the active chain is deactivated by the assimilation of a single atom or a part of the additive. At the same time the latter is activated. This mechanism may yield to the start of a new chain-growth reaction in case of a reactive species. If the second molecule X is another polymer chain, for example, a macromolecule with a branched structure can be generated. Hence, multiple chain-growth reactions finally form a dense polymer network. Thus, structuring with a negative tone photoresists is a good method for additive manufacturing.

2.3.2 *Positive Tone Photoresist*

Positive tone photoresists work the other way round being a method for subtractive manufacturing. Here, we start with polymer networks or long chain polymers. Under irradiation with light, the molecules undergo bond scission forming smaller residual units. Depending on the deposited dose, the residual units can get small enough to become soluble in a developer. The unexposed or underexposed parts remain solid. Thus, a spatially controlled light-induced cleaving of structures is possible. Therefore, positive tone photoresists are commonly used in microchip fabrication to provide etching masks. A prominent and widely used example is polymethylmethacrylate (PMMA). Since common positive tone photoresists are sparely used in 3D laser printing [4, 63], a more detailed description is out of scope for this thesis.

2.3.3 *Solubility*

As mentioned, most photoinitiators for negative tone photoresists are solid. However, since most monomers are viscous liquids, the photoinitiator molecules can be directly dissolved in the monomer. In general, a good solubility is beneficial for a higher sensitivity of the resist [64]. Usually, mixing around 2 wt% of an initiator is well achieved. Some very efficient, hence widely used, photoinitiators in 3D laser printing such as 7-diethylamino-3-thenoylcoumarin (DETC) or (2E,6E)-2,6-Bis (4-(dimethylamino)-benzylidene)-4-methylcyclohexanone (MBK) feature a very limited solubility though [64]. There, only an order of magnitude lower concentrations are possible [65]. Thus, research focuses on enhancing the solubility of these very sensitive photoinitiator molecules by modifying non-functional side groups of the molecules with long alkyl groups for example [64, 66].

In addition, solubility is important in case of a solid monomer. Here, an additional solvent is required to mix monomer and photoinitiator. However, the solvent adds to the volume of the resist without being involved in the polymerization reaction. This leads to some drawbacks of resists which require solvents: First, they are prone for shrinkage because the solvent molecules are not incorporated into the polymer network during 3D laser printing. Instead, they get washed out during development leaving space for the polymer network to shrink.

Second, solvents increase the risk of micro-explosions. During the printing process, heat is generated in the voxel. In liquid monomers, this heat can cause additional polymerization. However, in solvent based resists, the heat can start evaporating the solvent leading to micro bubbles. They restrict further polymerization. Thus, solvents with high boiling points are preferable if solvents are inevitable. Finally, high boiling points are also good with respect to evaporation over time during time consuming print jobs. In case of low boiling points, the

composition changes drastically during printing [67]. Hence, writing parameters change over time rendering reproducibility very challenging. Thus, the amount of employed solvent should be minimized why it should provide good solubility for both substances.

2.4 Standard Excitation Mechanism for 3D Laser Printing

Common focus scanning 3D laser printing builds on two-photon absorption for excitation. This process was theoretically predicted by Maria Göppert-Mayer in 1931 [68] and experimentally realized first by Wolfgang Kaiser and Charles Geoffrey Blythe Garrett in 1961 [69]. First applications were found in high-resolution microscopy. However, only 1997, Shoji Maruo made first usage in 3D microfabrication of polymeric materials [2].

In two photon absorption, the energy of one photon at the employed wavelength is not sufficient to excite the photoinitiator molecule. Only the sum of the energy of two photons at this wavelength is larger than the energy gap between the molecule's ground state and its first excited state. However, this transition is not possible without an intermediate state.

Real intermediate states cannot just be generated to fill this gap, unfortunately. However, the interaction of laser light with the molecule generates light dressed states in terms of the Floquet picture [70, 71]. This means that in the presence of light, intermediate states exist enabling two-photon absorption. The probability for such a process remains immoderately small with typical two-photon absorption cross sections in the range of $10^{-50}\mathrm{cm}^4\,\mathrm{s\,photons}^{-1} = 1\,\mathrm{GM}$. Thus, extreme photon flux densities in the range of $10^{31}\,\mathrm{photons\,s}^{-1}\,\mathrm{cm}^{-2}$ are required, only achievable by pulsed laser sources [7].

Once excited to the first excited singlet state, the photoinitiator molecule can undergo different reactions. Two of them are non-radiative or radiative decays back to the ground state, where the latter is better known as fluorescence. Another possible route is intersystem crossing to the triplet manifold. Further, homolysis of the excited singlet state can happen [72]. The rates for each of the possible mechanisms depend on the corresponding energy levels of the molecule among other properties such as the conformation. Usually, photoinitiator molecules are classified into two types depending on their preferred decay reaction. These are Norrish type I and Norrish type II initiators.

Norrish Type I

In Norrish type I reactions, the photoinitiator molecule – most often aldehydes or ketones [72] – undergo a fragmentation into two free radicals via α-scission. Depending on the molecule structure, various secondary reactions can be triggered

by these fragments. However, sufficient energy must be provided, i.e. the energy level of the excited singlet has to be high enough. Typical bond-dissociation energies are in the range of $3 - 4\,\mathrm{eV}$ [73]. Most of the commercially available photoinitiators are Norrish type I initiators.

Norrish Type II

In contrast, Norrish type II reactions do not include bond scission [74]. Here, the provided energy of the excited state is beyond the bond-dissociation energy. Instead, the molecule undergoes an intramolecular hydrogen abstraction reaction. This process is less probable than the Norrish type I reaction. However, the efficiency can be increased by adding hydrogen-donating coinitiators to the system.

2.5 The Threshold Dose

While a single initiation of a radical chain growth can easily involve thousands of monomer molecules [75], it is still not sufficient for a branched and dense polymer network. Thus, multiple chain-growth reactions have to be triggered at the same time employing multiple optical excitation processes. In general, each of the involved chemical processes during the chain growth has a specific rate constant. Hence, exact numbers could be derived solving the corresponding differential equations. However, it shows that this is not an easy task [61, 65]. Instead, the complex system is often simplified with the threshold dose model.

Here, the assumption is that after depositing a certain light dose D_{th} into a certain volume, the degree of polymerization exceeds a value from whereon the polymer network withstands the development process. Looking at a single point exposure, a direct correlation between light intensity I, exposure time t_{exp}, and the resulting dose D can be found

$$D \propto I^N \cdot t_{\mathrm{exp}}\,, \tag{2.1}$$

where N is the optical nonlinearity of the excitation, i.e. $N = 2$ in case of a normal two-photon process. This connection of laser intensity, exposure time (or in printing experiments rather print speed instead), and deposited dose (related to the degree of monomer conversion) can also be found experimentally [76, 77]. Figure 2.8 shows the threshold model in a dose profile along the lateral direction of the focus with varying laser intensity at a fixed exposure time. Employing a normalized high intensity (solid line), the threshold is met by far. At 65 % of this intensity (dotted line), the threshold dose is just surpassed. A further reduction of the intensity to 55 % (dashed line) does not deposit enough dose which would result in no remaining polymer after development. Further, the threshold model

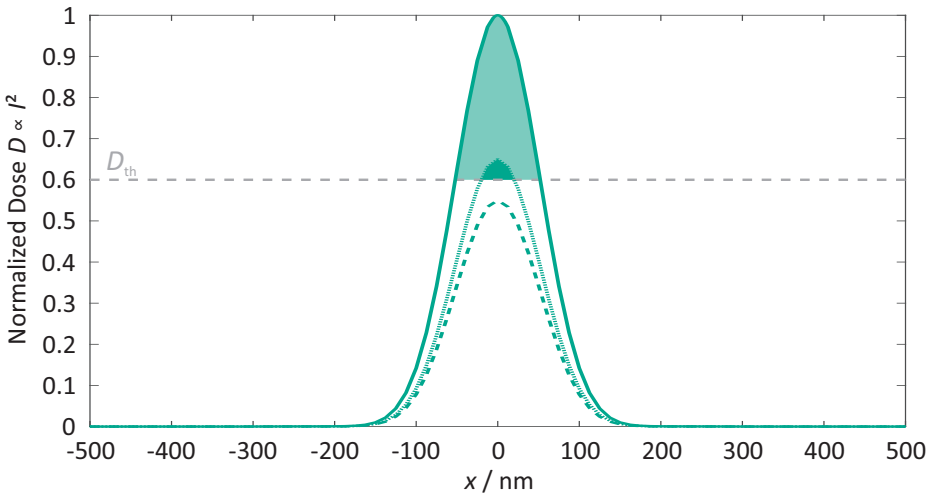

Figure 2.8: **Illustration of the threshold model.** The three-dimensional intensity profile is calculated for an NA = 1.4 objective lens at 405 nm wavelength, normalized, and squared to obtain the dose deposited in a voxel at a fixed exposure time. Plotted is a 1D cut in lateral direction showing the dose profile along the x-axis. Remarkably, the threshold model shows that there is no theoretical limit on how small a polimerized feature can get within a single exposure when depositing just more light than the threshold dose D_{th} requires.

nicely shows the influence of the intensity on the lateral width of the voxel. While the width at the threshold dose is 110 nm for the high intensity, it is only 40 nm using 65 % of the intensity. This shows the theoretically unlimited smallest feature size which can be produced by depositing a dose just above the threshold, hence a high spatial confinement of the polymerization.

2.6 Dose Accumulation

The threshold model, as discussed so far, only covers a point exposure with a given laser intensity and exposure time. Still, what needs to be discussed is the photoresist response on multiple subsequent point exposures at the same position or with a small distance. This is addressed in the dose accumulation model and is often referred to as the proximity effect [78]. It states that all dose deposited once in a certain volume remains in this volume. Additional dose by a following exposure locally adds up. Figure 2.9 depicts the accumulation behavior of multiple exposures which each would not deposit enough dose themselves. However, they sum up and exceed the threshold dose leading to solidified material.

This effect assigns a memory to the photoresist. The distinctness of the memory effect highly depends on the nonlinearity of the excitation process [79]. More

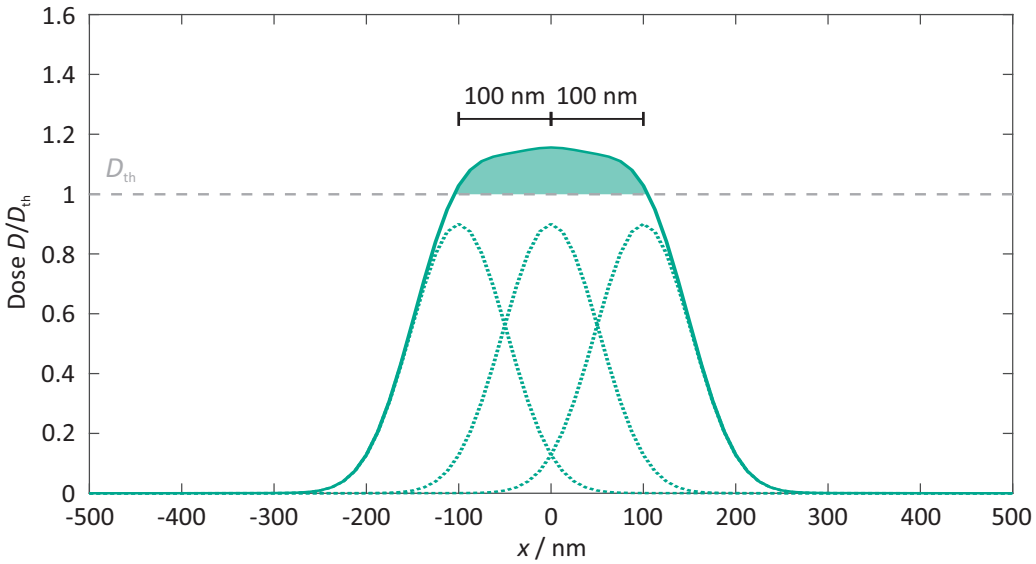

Figure 2.9: **Illustration of the dose accumulation model.** The deposited dose for three subsequent point exposures (dashed lines) shifted by 100 nm each is plotted together with their sum (solid line). The intensity for a single exposure is chosen such that it deposits 90 % of the threshold dose D_{th}. Therefore, a single exposure would not lead to solidified material. However, the totalized dose of all three exposures exceeds the threshold resulting in solidification. Here, the same intensity profile as for the threshold model is calculated for the single exposures and normalized to the threshold dose.

generally, the dose at a specific location can be calculated by integrating the time dependent local intensity $I(x, y, z, t)$ over time

$$D(x, y, z) \propto \int I^N(x, y, z, t)\, \mathrm{d}t\,. \tag{2.2}$$

It is not only a theoretical model but can be explained from a chemical point of view by the mentioned degree of polymerization. As explained, a single radical chain-growth reaction is not capable to sufficiently solidify the photoresist. However, each successfully two-photon excited photoinitiator molecule which subsequently fragments will still trigger such a chain growth. Thus, oligomers or small polymer chains originate. These will not magically disappear at a sudden but remain in the photoresist. This is the chemical reasoning of the resist's infinite memory. A next chain growth can incorporate these larger molecules similar to a normal monomer. Still, the pre-polymerized chains can freely move within the resist. Therefore, processes like diffusion limit the validity of the dose accumulation model and exacerbate calculations and predictions [61, 65].

A second type of dose accumulation gets relevant for excitation mechanisms other than two-photon absorption like (1+1)-photon processes. Here, the memory

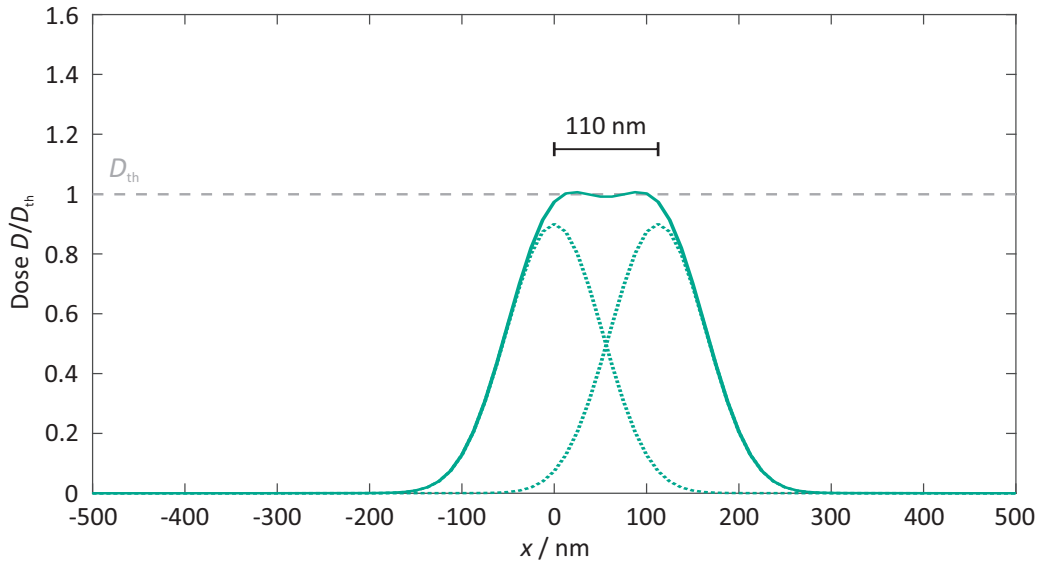

Figure 2.10: **Illustration of the Sparrow criterion.** The accumulated dose profile (solid line) of two shifted point exposures (dashed lines) shows a distinct minimum. Thus, the resolution criteria is met and two separate points are solidified. The depicted separation of the single exposures is 110 nm. Besides the change of the shift, no changes are made as compared to the illustration of the dose accumulation model in Figure 2.9. There, the shift was set to 100 nm resulting in no local minimum. The minimum emerges at a shift of around 105 nm nicely matching the calculated results from Table 2.1.

effect of the photoresist includes pre-activated initiator molecules due to their finite intermediate-state lifetime being in the µs range. More precisely, let us take a first exposure employing low intensity. Some of the initiator molecules undergo full excitation and fragment into radicals triggering chain growth. Let us further assume that not enough dose is deposited into the voxel to overcome the threshold with this first illumination. Still, some initiator molecules may already have been excited to the intermediate state. Under a second exposure within the intermediate-state lifetime, these pre-excited molecules can now accomplish the full excitation and form additional radicals. Thus, the additional chain growth reactions add to the degree of polymerization and might result in a dose larger than the threshold dose. This kind of dose accumulation will be discussed in further detail in chapter 3.

2.7 Resolution in 3D Laser Printing

As briefly mentioned in the threshold model section, the minimum linewidth is not limited fundamentally. Patterning of sub-10 nm features [80], and other

sub-diffraction lines [81] have been reported. However, it is important that the minimum achievable feature size must not be confused with the resolution of the printing process. Instead, the same constraints of the diffraction limit as for microscopy apply to high-resolution 3D laser printing.

First considerations on resolution in microscopy were made by Ernst Abbe on the smallest resolvable lattice constant of a periodic grating [82]. However, the Sparrow criterion, which was originally developed for astronomy [83], is the more relevant choice for 3D laser printing [36]. In contrast to the Abbe criterion, the claim is that two signals are still distinguishable as long as there remains a local minimum in the center of the sum of the signals.

This criteria can be directly translated to 3D laser printing with the dose accumulation model explained above. In particular, two shifted point exposures remain distinct with decreasing spacing as long as their accumulated dose shows a local minimum. The required local minimum is crucial even for a deposited dose just above the threshold, thus for a fine feature in case of a single exposure. This effect is schematically shown in Figure 2.10. Numerical approximations for both lateral and axial resolution can be derived from Abbe's resolution formula according to Ref. [36] as

$$\begin{aligned} a_x &= \frac{\lambda}{\sqrt{N} \cdot 2\mathrm{NA}} \quad \text{and} \\ a_z &= \frac{\lambda}{\sqrt{N} \cdot (n - \sqrt{n^2 - \mathrm{NA}^2})}, \end{aligned} \tag{2.3}$$

respectively, with the wavelength λ, the nonlinearity N, the refractive index n, and the numerical aperture NA. Here, the general nonlinearity N replaces the factor of 2 in Ref. [36]. Equation 2.3 shows the linear dependence of the resolution on the employed wavelength explaining the drive in lithography applications to exploit ever shorter wavelengths [84]. At the same time it reveals the necessity of utilizing high-NA objective lenses for high-resolution 3D laser printing. Table 2.1 summarizes calculated values for different configurations employed within this thesis. A constant nonlinearity of $N = 2$ and a refractive index of $n = 1.5$ is chosen.

Importantly, the restriction on the optical resolution in 3D laser printing bases on the dose accumulation, hence, the memory effect of the photoresist. In the theoretical case of a perfect system without any dose accumulation, the resolution would possibly be improved by orders of magnitude. However, such a photoresist is yet to be found. Moreover, in addition to the optical resolution limit, also chemical restrictions can influence the resulting resolution in 3D laser printing [85–88].

2.8 Limitations of 3D Laser Printing

While two-photon absorption based 3D laser printing has developed into a versatile micro-fabrication technique, it is still accompanied by some limitations. One are the required high intensities due to the extremely low probability of the two-photon absorption process. As discussed in the threshold model, the usual photoresist behavior in a point-exposure experiment at a fixed exposure time is as follows: Starting at a low intensity may not lead to any polymerization. While increasing the intensity, at some point the threshold dose will be reached and a tiny polymerized dot will appear. Further increase of the intensity will lead to larger polymerized voxels as discussed. However, what was not mentioned earlier is the increase of local heating which comes along with the higher intensity. At some point, yet higher intensities will yield micro-explosions of the monomer or the solvent in case of solvent based resists (see subsection 2.3.3). This is often referred to as the damage threshold of the resist [45, 65]. In fact, this heating sets an upper limit for the print speed for a given resist, since higher print speeds require higher laser intensities.

Also, 3D laser printing on the basis of two-photon absorption benefits from the vast amount of photoinitiator and monomer systems developed in one-photon UV lithography. It just exploits them at double the wavelength, hence half the photon energy. However, as discussed in the previous section, the optical resolution directly correlates with the exposure wavelength. Already in the very first experimental mentioning of two-photon lithography, Wu et al. address the resolution loss compared to one-photon absorption due to the doubling of the wavelength [11]. They calculate the final relative line broadening to a factor of 1.41. It is not a full factor of 2 due to the narrowing of the two-photon excitation function compared to the one-photon excitation function which partially compensates for some of the loss.

Still, the drastic reduction of the resolution in case of 780 nm wavelength as utilized in most commercial systems compared to 405 nm is set out in Table 2.1 when assuming the same excitation mechanism. Thus, two-photon 3D laser printing at

Table 2.1: **Calculated lateral and axial resolutions and their corresponding aspect ratio for the different 3D laser printing configurations employed within this thesis.**

λ in nm	NA	a_x in nm	a_z in nm	Aspect Ratio
405	1.4	102	298	2.91
405	1.25	115	427	3.71
700	1.4	177	515	2.91
780	1.4	197	574	2.91
900	1.4	227	662	2.91

a reduced wavelength would be beneficial. Most commonly used photoinitiators would undergo a simple one-photon absorption at these wavelengths though. However, a direct two-photon excitation of the monomer is possible at a wavelength of 405 nm [12, 89, 90]. A special application of this direct excitation of the monomer itself is presented in chapter 6, where high-resolution kinoform lenses for x-ray applications are 3D laser printed.

Over years, the surface smoothness of 3D laser printed structures was limited by the known staircasing effect. This effect is shared by all layer-by-layer manufacturing techniques. Volumetric approaches outperform common focus-scanning 3D laser printing in this regard. However, recent introduction of two-photon grayscale lithography [34] can overcome the staircasing effect for focus-scanning 3D laser printing resulting in extremely smooth surfaces [35].

Further requirements are on the transparency and the refractive index of the resist. The transparency constraint has a two-fold impact. First, in case of non-transparency at the employed wavelength, the resist absorbs energy while propagating through the resist. Thus, the focus intensity decreases and again heat is induced. Additionally, it limits size and concentration of additives in special resist systems[52, 91]. These additives can also cause spatial inhomogeneities of the refractive index of the resist resulting in optical abberations. Moreover, the refractive index of the entire resist is of importance. High-NA objective lenses usually are index matched to oil or water immersion media. Again, the resist should not deviate largely from the respective refractive index to avoid deformations of the focus. The latter was relevant in our work on 3D laser printing inside synthetic cells [92].

2.9 Common Applications

Over the last decade, applications of common 3D laser printing have exorbitantly increased. Thus, a complete overview is out of scope of this thesis. The applications reach over all kinds of disciplines: optics, photonics, biology, electronics, mechanics, acoustics, and metamaterials just to name a few of them. Even leaving 3D and adding a forth dimension – a responsiveness – is already widespread [10]. The reader is endorsed to look at some of the review articles in the field of 3D laser printing to get a better overview [4, 6–9, 93].

2.10 Open Challenges in 3D Laser Printing

Even though the list of applications is almost infinite, the open challenges are merely fewer. In general, they can be split into challenges for chemistry towards novel materials and material systems [3, 94] and challenges for physics towards improvements of the printing devices. The statement of the cluster of excellence

3DMM2O – finer, faster, more – nicely matches these open challenges: Further improvement of the resolution of 3D laser printing, pushing the print speeds to its limitations, and the development of new materials and material properties remain the overarching goals.

Within the scope of my thesis, I worked on both aspects – the challenges for chemistry and for physics. Different collaborations involved additional projects that tackled 3D laser printing in the vicinity of living cells employing resists that are capable of cleaving under biological conditions, two-photon induced structuring of surface-anchored metal-organic frameworks (SURMOFs), 3D microprinting of conductive polymers, two-photon induced carbonization, reducing shrinkage by introducing a novel material class [95], the cause of material-property changes by a variation of the excitation wavelength during printing, and 3D laser printing of hydrogel structures inside synthetic cells [92].

Especially the latter was a special application although it utilized a commercial 3D laser printer. Here, the challenge was the special resist system and printing condition. The resist is based on the prepolymer poly(ethylene glycol) diacrylate 575 (PEGDA) the water-soluble photoinitiator lithium phenyl-2,4,6-trimethylbenzoylphosphinate (LAP), both in extremely low concentrations. However, it is challenging to get stable synthetic cells with the resist incorporated. Additionally, printing structures across the shell of the synthetic cells were expected to cause damage. Still, after major optimization, successful 3D laser printing was achieved and small channels across the membrane functioning as pores allowed for substance exchange.

The main projects of research during my PhD will be discussed in more detail in the following chapters.

Part I

COMPACT 3D LASER PRINTING

Chapter 3

3 Enabling Compact 3D Laser Printing

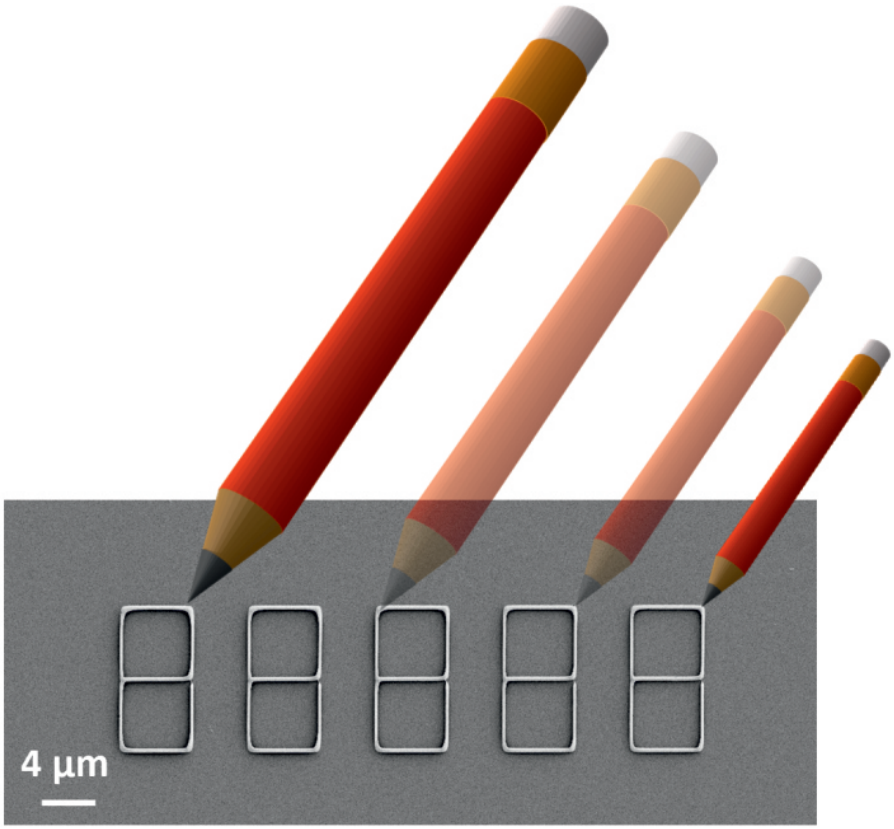

Artistic illustration of compacting the writing tool.

State-of-the-art 3D laser printers are bulky and expensive. The supersession of two-photon absorption by the sequential absorption of two photons – what we call two-step absorption – as a new excitation mechanism for 3D laser printing can change this and enable compact and less expensive devices. In this chapter, the challenges of two-step absorption and its differences compared to common two-photon absorption will be discussed.

3.1 Motivation

As discussed in section 2.4, two-photon absorption is used for excitation in common 3D laser printing. Within the last decade, a tremendous progress in devices, material systems, and applications on its basis was achieved. It allows for printing high-resolution 3D structures with voxel sizes well below 1 µm at print rates of above 10^5 voxels s^{-1} reaching even 10^8 voxels s^{-1} in case of parallelization and a highly-optimized 3D laser printing device [96]. Still, two-photon absorption comes at the cost of requiring femtosecond-pulsed laser sources leading to different draw-backs.

At a price of around 100 000 Euros, commonly used Ti:Sapphire oscillators are by far the main cost driver in most custom 3D laser printing setups. Next most expensive components like the control electronics or the microscope objective lens, at costs of 10 000 Euros and below, only add little to the overall cost in comparison. Further, the laser module not only takes up most of the cost but also most of the volume of a 3D laser printing setup. Taking laser head, electronics, chiller, and all other components together, it has already the size of a large suitcase – not to mention the weight it comes along with. Therefore, femtosecond-pulsed laser sources inherently cause fairly large and expensive 3D laser printers.

Besides these rather practical issues, also more fundamental problems are induced by the femtosecond-pulsed laser sources. Already the high intensities employed for efficient two-photon absorption cause problems in handling 3D laser printing. They do not only allow for the desired second-order process but at the same time increase the probability for higher-order processes. These processes, however, are undesired since they introduce effects like micro-explosions [97] rendering the printed structures unusable as discussed in section 2.8. Additionally, the continuous development in print speed and parallelization demands for ever higher laser intensities pushing them close to the damage threshold of the used optical elements like the microscope objective lens or the galvanometric mirror devices [98].

Early attempts to replace femtosecond-pulsed laser sources by a continuous-wave laser were conducted in our group years ago. Their incentive, however, was to exploit a reduced wavelength to improve the printing resolution. In a first experiment, Michael Thiel et al. employed a green continuous-wave laser at powers around 10 mW [99]. However, these high powers caused micro-explosions hindering further application. Therefore, Patrick Müller et al. electronically pulsed their continuous-wave blue diode laser retaining efficient two-photon absorption of the photoinitiator, as a trigger for the polymerization [12].

On the other hand, alternative excitation mechanisms utilizing multiple one-photon absorption processes in different ways [100] allow for continuous-wave lasers to be used as light sources. These show potential to solve some of the

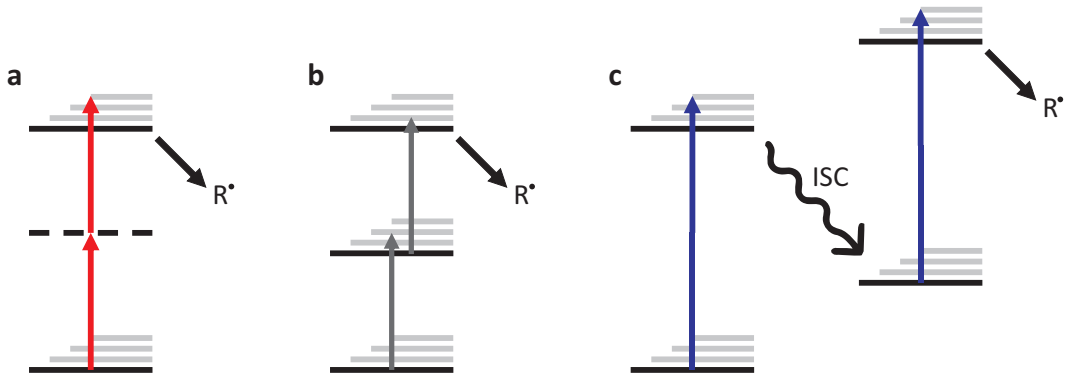

Figure 3.1: **Simplified energy-level diagrams for two-photon (a) and two-step excitation (b) of a photoinitiator molecule.** **a** Using two-photon absorption, the photoinitiator molecule is excited from its ground state to an upper electronic state via an optically dressed intermediate state (dashed line). Out of the upper electronic state, the molecule decays into free radicals $R^{\bullet}$ triggering the polymerization reaction. **b** For two-step absorption, a real electronic state (solid line) replaces the optically dressed intermediate state. **c** A more realistic diagram for two-step absorption. Real electronic states of a molecule cannot just be generated. Therefore, the first excited state, which is the upper state in **a**, constitutes the real intermediate state in case of two-step absorption. The second photon causes a transition in the triplet manifold after intersystem crossing takes place.

fundamental problems of two-photon absorption and especially the practical problems of femtosecond-pulsed laser sources having other disadvantages in return. The most straight-forward approach is what we call two-step absorption and will be discussed in the following sections.

3.2 Two-Photon Absorption *vs.* Two-Step Absorption

A crucial parameter for the probabilities of step-wise electronic transitions in molecules is the lifetime of the involved molecular states. For example shorter intermediate-state lifetimes correspond to lower probabilities of a further optical transition. This can easily be seen as with a shorter intermediate-state lifetime, the corresponding pre-excited molecule will more rapidly return to its ground state leading to a shorter period of time for a second photon to be absorbed. Thus, assuming a constant light intensity, hence a constant photon flux, the probability of the optical transition will decrease.

In section 2.4, two-photon absorption as the common initiation mechanism in 3D laser printing was discussed. Here, two photons are absorbed to optically excite the photoinitiator molecule from its ground state S_0 to the first excited state S_1 via an optically dressed intermediate state (see panel **a** in Figure 3.1) [68].

Optically dressed means that this intermediate state only exists while light is present. Therefore, the intermediate state's lifetime is the pulse duration of the femtosecond-pulsed laser source in this case, making the process very unlikely. In turn, high laser intensities are necessary to compensate for the small probability.

Another approach leading to higher probabilities is to increase the intermediate-state lifetime instead of the laser intensity. This can either be achieved by increasing the pulse duration of the laser pulse, or more fundamentally by replacing the optically dressed intermediate state by a real electronic state as depicted schematically in center panel **b** of Figure 3.1. The process exploiting such a real intermediate state while absorbing two photons is what we introduced as *two-step absorption* [31].

In fact, real electronic states cannot just be generated but existing electronic states of the photoinitiator molecule have to be employed. Therefore, the first step comprises the transition of the molecule from S_0 to S_1 similar to the full two-photon absorption process but this time only using a single photon. The subsequent second photon is absorbed after rapid intersystem crossing from S_1 to the ground-state triplet manifold T_1 inducing an excitation from T_1 to a higher triplet state T_n. This high-energy electronic state of the photoinitiator molecule readily decays into free radicals $R^\bullet$ triggering the polymerization reaction. A more realistic schematic following the latter is shown in panel **c** of Figure 3.1.

3.3 The Effective Nonlinearity in Two-Step Absorption

The open question remains in what nonlinearity exponent N or effective order of absorption [101] the two-step absorption process will result. As discussed in section 2.6, the crucial element for printing high-resolution three-dimensional structures in 3D laser printing is the second order, or more general, nonlinear dependence of the intensity I and the concentration of radicals $[R^\bullet]$ which corresponds to the deposited optical dose D

$$[R^\bullet] \propto D \propto I^N. \tag{3.1}$$

One-photon processes in contrast result in a nonlinearity exponent of $N = 1$. Depending on the exact structure, dose accumulation will severely influence the printing process making it harder if not impossible to spatially confine the polymerization given such a linear characteristic [64]. A resulting nonlinearity of $N = 2$ or higher is therefore highly desirable for the two-step process. The subsequent two one-photon absorption processes, however, inherently are not resulting in such an optical nonlinearity, because both absorption steps come along with a single photon.

Again, it is the intermediate-state lifetime which sheds light on the effective nonlinear exponent in two-step absorption. The two extreme cases for the lifetime help in understanding its role: One extreme is a very short intermediate-state

lifetime. Here, the molecule rapidly decays back into its ground state from the excited intermediate state after the first photon is absorbed, lowering the probability for the second absorption process. This builds the crossover to two-photon absorption resulting in good spatial confinement of the voxel. At the same time, again high laser intensities are required to compensate for the low probability.

The second edge case is an extremely long intermediate-state lifetime. Here, the decay of the intermediate state back to the ground state is very unlikely and the intermediate state is pretty stable. The result is a very high probability for the second absorption process, or in turn only necessitates extremely low laser intensities. At first sight, this looks beneficial since it allows for low power light sources, but it causes a big problem: The pre-excitation is not only achieved in the focal spot but also in the tails of the laser beam since it is a normal one-photon process. Eventually, all molecules are lifted into the intermediate state forming a kind of new ground state of the system [98]. Starting from there, a single one-photon absorption – having a nonlinearity exponent of $N = 1$ – is sufficient for the second step. This will fundamentally influence the maximum print speed. When scanning the laser focus along the desired trajectories, it would certainly hit such areas pre-excited by a previous tail. Assuming an infinite intermediate-state lifetime, a single one-photon absorption would trigger the second excitation and generate radicals, thus, hindering high resolution printing.

In summary, a good intermediate-state lifetime is always a tradeoff between spatial confinement and required laser intensity shifting the effective nonlinearity exponent between $N = 2$ and $N = 1$. This leads to a severe fundamental limitation of the system as will be discussed later in section 3.5.

3.4 Important Two-Step-Photoinitiator Properties

Besides a suitable intermediate-state liftetime, various other properties of the two-step photoinitiator molecule are important. One of them is solubility. As discussed in subsection 2.3.3 for common two-photon initiators, it is favored to be able to dissolve a sufficient amount of photoinitiator in the used liquid monomer for efficient polymerization [64]. Another property is the efficiency of the molecule to form radicals from the excited triplet state T_n. Concurrent transition pathways are for example radiative or non-radiative decays back to the triplet ground state or reverse intersystem crossing [102]. Further criteria will be discussed in more detail in the following.

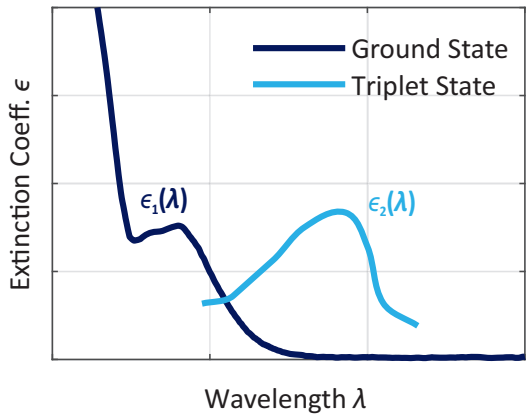

Figure 3.2: **Schematical extinction-coefficient plots for ground-state and triplet-state absorption.** The exemplary curves show the requirements of overlapping absorption bands positioned in the visible range. The curves follow roughly the real curves of benzil shown in Figure 3.5. Adapted from Ref. [31] with permission of Springer Nature.

3.4.1 *Absorption Bands*

At first, the two absorption bands involved in the two-step mechanism will be examined. One is the absorption band for the first transition from the ground-state to the first-excited state ($S_0 \longrightarrow S_1$) and the second band for the triplet excitation ($T_1 \longrightarrow T_n$). An overlap of the two is crucial for the two-step mechanism as discussed above, since it demands employing a single laser source, hence, a single wavelength. There are other approaches using two different or additional wavelengths for the two optical transitions [25, 26, 103]. This is what we refer to as *two-color* two-step absorption but will not be discussed in more detail here. In particular, because the second wavelength requires additional components and with that a more complex printing setup. In this chapter, two-step absorption will always refer to the one-color case.

Not only is the overlapping of the two absorption bands necessary, but also their absolute location is of importance. Figure 3.2 shows schematically desired extinction coefficient plots. As discussed in section 2.7, the resolution of a 3D laser printer is limited by the diffraction limit. Therefore, smaller wavelengths are desirable for a higher resolution. However, a lower limit is introduced by the device. Most of the optics used in a 3D laser printer, such as the high-NA microscope objective lens, are made out of special glasses. These objective lenses work perfectly well in the visible range to correct for different types of optical aberrations using lens groups [104], but for most glasses transmittance rapidly drops when going into the UV regime [105]. Thus, an absorption band at around 400 nm features a good compromise.

So far, only the positions of the absorption bands were discussed but not their strengths. The extinction coefficients ϵ of the two absorption processes, however, are elementary for the overall two-step excitation mechanism. At first sight, a high ground-state extinction coefficient ϵ_1 seems preferable. It allows for an efficient transition from the ground state to the intermediate state and could even

compensate for low solubilities of the photoinitiator in the photoresist. On the other hand, to polymerize material in a distance of d from the glass interface, the laser needs to be focused at this position. Thereby, the laser light propagates through distance d in the resist. Following Beer's law

$$P = P_0 \cdot 10^{-\epsilon_1 c d}, \tag{3.2}$$

the laser beam is attenuated while covering the distance d. The strength of the attenuation directly correlates with the extinction coefficient ϵ_1 and the concentration c of the photoinitiator. Using real numbers of $\epsilon_1 = 40\,\mathrm{M}^{-1}\,\mathrm{cm}^{-1}$ and $c = 100\,\mathrm{mM}$ for the photoinitiator benzil used in the resist system employed in chapter 4, a (decadic) extinction of $\epsilon_1 c = 4\,\mathrm{cm}^{-1}$ results. This effect is yet more pronounced employing dip-in 3D laser printing since the traversed distance through the photoresist gets significantly larger. Making use of the calculated examplaric values, a power of $P = 0.76 \cdot P_0$ remains in the focal spot using a common working distance of the objective lens of 300 µm in the real photoresist system. The absorbed photons add to the accumulated dose or introduce heat in the system. Therefore, actually a sufficiently small ground-state extinction coefficient is desirable.

The discussion on the triplet-state extinction coefficient ϵ_2 is yet more complex and not as easily explained by a similar gedankenexperiment. Following the rate-equation modeling in Ref. [31], it can be shown that at a fixed exposure time the nonlinearity exponent approaches $N = 1$ for both small and large ratios of ϵ_2/ϵ_1 having a maximum at $\epsilon_2/\epsilon_1 = 1$, i.e. for equal extinction coefficients [98]. This suggests an upper bound for ϵ_2 in two-step absorption. In contrast, a high extinction coefficient would be beneficial for a lower polymerization threshold. These trade-offs introduced by the two independent absorption steps are limits in two-step 3D printing and are not present for conventional two-photon printing. A more detailed discussion will follow in section 3.5.

3.4.2 *Triplet Ground-State Energy*

Up to now, we made use of the intermediate-state lifetime to explain various effects. However, underlying physical properties of the molecule the lifetime originates in were bypassed. One of these is the triplet ground-state energy. First, the energy of the triplet ground state T_1 together with the energy of the first excited singlet state S_1 impact the rate for the intersystem crossing among various other effects [106]. The so-called energy gap law shows an approximately exponential dependence of nonradiative transition rates – like for intersystem crossing – on the energy difference between initial and final state [107]. A more generalized energy gap law additionally involves temperature dependence and low-frequency modes [108]. This means that with increasing energy gap the probability for the corresponding

Table 3.1: **List of triplet-state energies E_T of selected aldehydes and ketones.** These groups form the majority of common one-photon photoinitiators [72]. The energies are taken from Ref. [110].

Molecule	E_T / eV	Molecule	E_T / eV
Xanthone	3.2	Michler' ketone	2.6
Acetophenone	3.2	1-Naphthaldehyde	2.4
Benzaldehyde	3.1	Biacetyl	2.4
Benzophenone	3.0	**Benzil**	**2.3**
Anthraquinone	2.7	Fluorescein (acid)	2.2

nonradiative transition decreases exponentially. Thus, two energetically nearby states S_1 and T_1 are desirable for efficient intersystem crossing in general.

At the same time, the absolute energy levels of S_1 and T_1 are important for two-step 3D laser printing in particular. Typical bond-cleavage energies of photoinitiator molecules are on the order of $3\,\mathrm{eV} = 290\,\mathrm{kJ\,mol^{-1}}$ [72]. Hence, intermediate-state energies below this value suppress bond-scission reactions starting from T_1, hindering radical formation. Such an intermediate-state bond cleavage would trigger the polymerization reaction after only having absorbed a single photon, thus, leading to an undesired nonlinearity exponent of $N = 1$.

Ketones and aldehydes with at least one carbonyl group form the majority of common one-photon photoinitiators [72] forming the pool of possibly suitable two-step initiator candidates. A selection of molecules is presented in Table 3.1 together with their triplet ground state energies E_T. It shows that there are quite a few candidates possessing low energies. However, to act as a good two-step photoinitiator, also the other aforementioned criteria have to be fulfilled. Fluorescein, for example, shows the lowest triplet energy level in this selection but is well known and extensively used as a marker in fluorescence microscopy due to its high fluorescence quantum yield [109]. This entails a small quantum yield for intersystem crossing, thus, rendering fluorescein useless as a two-step photoinitiator candidate. In contrast, benzil, which is so far the common two-step photoinitiator, also shows a low energy while having a high quantum yield for intersystem crossing. Two-photon 3D laser printing evades this constraint of low triplet ground state energies because it commonly employs this very bond cleavage from the T_1 state but at the same time features an inert intermediate state.

3.4.3 *Inert Intermediate State*

The theoretical model of two-step absorption as discussed at the beginning of this chapter also employs an inert intermediate state. The real system, however, differs from that assumption. Ketones and aldehydes as photoinitiator systems are known to trigger polymerization via a Norrish Type I or Norrish Type II reaction [74]. Both reaction types involve the formation of radicals in the first excited state [111]. Acting as a two-step photoinitiator, thus, they are prone to form radicals already from the intermediate state leading to the reviewed problem of a unity nonlinearity exponent.

As discussed in the previous subsection, low intermediate-state energies help to suppress bond cleavage, hence, direct formation of radicals in the intermediate state as in Norrish Type I reactions. However, reaction pathways like intramolecular hydrogen abstraction as in Norrish Type II reactions or intermolecular hydrogen abstraction reactions may still well be triggered. This harms the inertness of the intermediate state even at very low energies again shifting the nonlinearity exponent towards $N = 1$.

Therefore, additional ways need to be found to minimize these remaining unwanted side reactions which lead to a polymerization triggered from the intermediate state. The exploitation of a so-called triplet quencher is one option to suppress hydrogen-abstraction reactions [110]. These molecules foster the relaxation of the triplet state back to the ground state. One ubiquitous triplet quencher is molecular oxygen which is dissolved in every photoresist [59, 61, 112]. However, it is hard to control oxygen quenching since solvated oxygen molecules also scavenge free radicals, and thereby they are consumed during the printing process [59, 61].

As a result, additional quencher molecules need to be added to the resist. The group of hindered amine light-stabilizers, for example, provide the required properties being so-called persistent radicals [113]. The latter means they are not self-terminating but still react with other free radicals. The molecule (2,2,6,6-tetramethylpiperidin-1-yl)oxyl (TEMPO), being one representative of this group, is reported to efficiently suppress hydrogen-transfer reactions when being excited [114]. Furthermore, it is capable of quenching the triplet state of benzil [115] which allows for fine tuning benzil's triplet-state lifetime. A second promising candidate is bis(2,2,6,6-tetramethyl-4-piperidyl-1-oxyl) sebacate (BTPOS) which contains two TEMPO moieties. Thus, additional quencher molecules like TEMPO allow for minimizing unwanted side reactions from the intermediate state, and therefore have been required for two-step 3D laser printing until now.

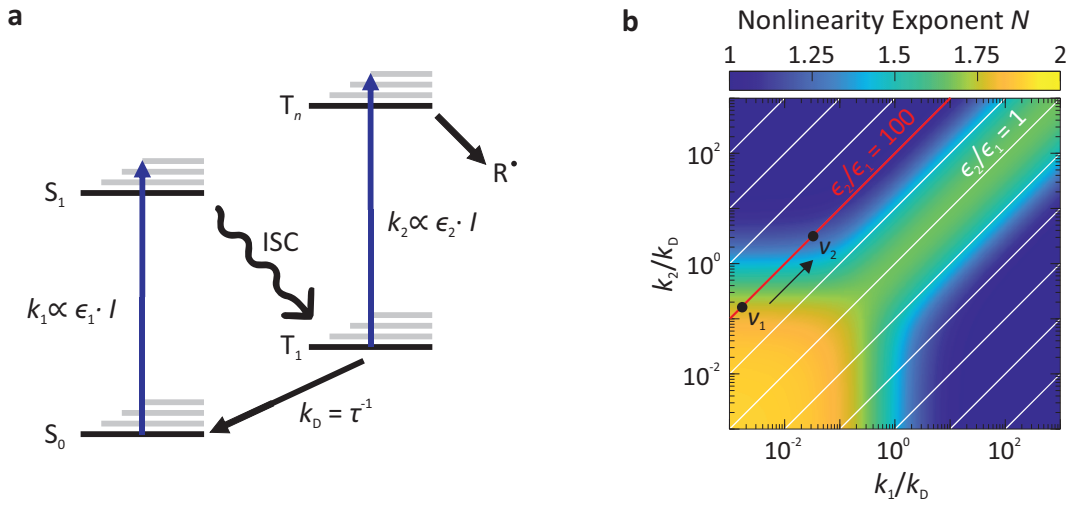

Figure 3.3: **a** Simplified energy-level diagram for rate-equation modeling following the diagrams in Figure 3.1. The molecule is optically excited by a first photon from its ground state S_0 to the first excited state S_1 with the rate coefficient k_1. After relaxation and intersystem crossing (ISC) to the lowest triplet state T_1 it is either optically excited by a second photon to a higher triplet state T_n with the rate coefficient k_2 from whereon it generates radicals or decays back to its ground state with the rate coefficient k_D. Both rate constants associated with the optical transitions are proportional to the respective extinction coefficients ϵ_1 and ϵ_2, and the laser intensity I. **b** False-color plot of the calculated nonlinearity exponent N. The two transition rates on the x- and y-axis are normalized with respect to the decay rate. The diagonals depict constant ratios of ϵ_2/ϵ_1. The red diagonal shows the real case of benzil at a wavelength of 405 nm. Moving along a diagonal implies a change in laser intensity which can be a result of a change in print speed v. Adapted from Ref. [31] with permission of Springer Nature.

3.5 Limitations in Two-Step Absorption 3D Printing

Previously discussed criteria for two-step photoinitiators fundamentally limit two-step absorption 3D printing in different ways. In particular, the limitation of the print speed by the intermediate-state lifetime is unknown from common two-photon 3D printing. This contradicts the ongoing research in two-photon 3D laser printing to boost print speeds to its limits by parallelization [5, 26, 116–118] for enabling printing of macroscopic structures with microscopic features at a tolerable duration of the print job. The different influences on the intermediate-state lifetime lead to a high complexity in terms of the resulting essential nonlinearity for the radical formation. Therefore, rate-equation calculations are employed for a more detailed discussion and a better understanding. They were predominantly performed by Vincent Hahn and are discussed in more detail in Ref. [31, 98]. We will focus on the limits of the print speed only, while the performed rate equation

model reveals many additional insights.

Figure 3.3 shows parts of the obtained results. In panel **a** on the left side, again a simple two-step-mechanism energy model including the rates for the different transitions is shown. Besides the two intensity-dependent rates k_1 and k_2, corresponding to the two optical excitations including their respective extinction coefficients, an additional decay rate k_D is implemented summarizing all reaction pathways from the intermediate state not resulting in a generation of radicals. This decay rate is the inverse of the intermediate-state lifetime τ. In panel **b**, the effective nonlinearity exponent N is plotted in false colors over the two excitation rates k_1 and k_2, both normalized with respect to k_D.

In fact, the plot shows areas where the nonlinearity exponent reaches $N = 2$ as desired. However, $N = 2$ is only reached for small ratios of both k_1/k_D and k_2/k_D in the lower left. Rather on the contrary the plot reveals that N can take all values between $1 < N < 2$ and most combinations of the normalized excitation rates lead to a nonlinearity exponent of $N \neq 2$.

For a given molecule, the two extinction coefficients ϵ_1 and ϵ_2 are constant at a fixed wavelength. Assuming a one-color two-step process, we additionally employ the same laser intensity to excite both transitions. Therefore, for a specific molecule, the parameter space in this plot is limited to a diagonal line. The real case for benzil is depicted with the red diagonal, where the triplet extinction coefficient ϵ_2 is a hundred times larger than the ground state extinction coefficient ϵ_1. Going along that diagonal starting from the lower left, the regime of $N = 2$ is exited quite rapidly. At the same time, the change of k_1 and k_2 while going along the diagonal relates to a change in laser intensity.

To form radicals for the polymerization reaction, we need to deposit a specific dose D larger than the threshold dose into a specific volume as discussed in section 2.5. Thus, scanning with a small print speed v_1 only demands for small laser intensities which in turn correlates to small rates k_1 and k_2. An increase of the print speed to v_2 involves an increase in the laser intensity. This corresponds to a motion toward the top right in the plot leading to a higher population of the intermediate state as discussed earlier. As a result, the nonlinearity exponent gets closer to $N = 1$.

3.6 The Two-Step Photoinitiator Benzil

Aldehydes and ketones are promising possible two-step photoinitiators as previously discussed. One representative of these groups is benzil. It nicely fulfills most of the reviewed characteristics. Benzil belongs to the α-diketones and consists of two adjacent carbonyl groups twisted by a dihedral angle of 117° in its ground state [120]. Panel **a** of Figure 3.4 shows its structural formula. Benzil is

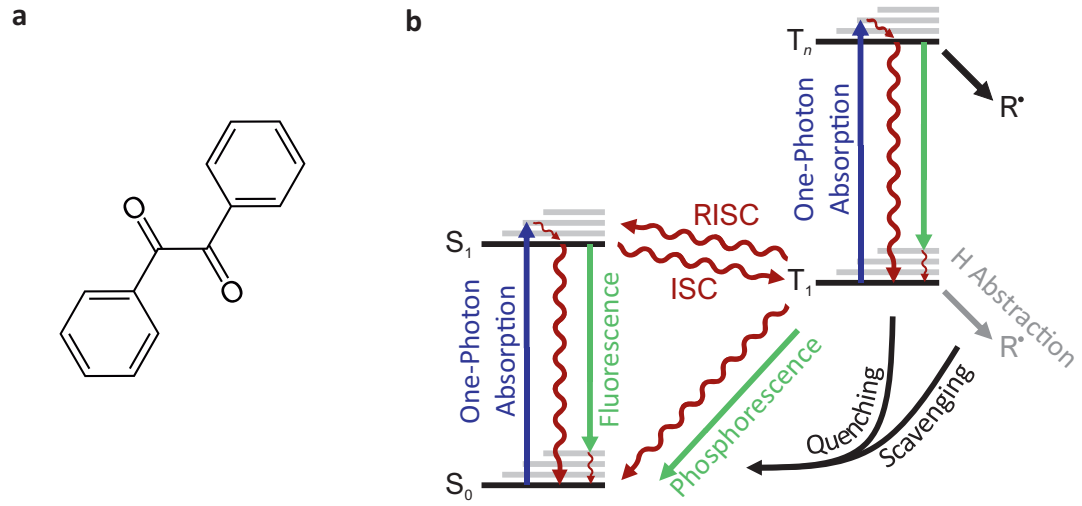

Figure 3.4: **Benzil and its Jabłoński diagram based on Ref. [119]. a** Structural formula of the benzil molecule. **b** Energy diagram showing the most important radiative and non-radiative transitions. Radiative transitions are depicted with straight arrows while waved arrows illustrate non-radiative transitions. The unintended radical formation via hydrogen abstraction from the lowest triplet state is added in gray. Additional quenching and scavenging is necessary to suppress this side reaction. Adapted from Ref. [31] with permission from Springer Nature.

seldomly used as a one-photon photoinitiator and is branded as a 'relatively poor' photoinitiator [72] in literature. The corresponding Jabłoński diagram based on Flamigni et al. [119] is shown in panel **b** of Figure 3.4. The main photophysical parameters of benzil are summarized in Table 3.2.

Benzil is readily optically excitable with UV- or blue light having an absorption band at 380 nm [121]. The tails extend to the visible range resulting in a molar decadic extinction coefficient of $\epsilon_1 = 40\,\mathrm{M}^{-1}\,\mathrm{cm}^{-1}$ at 405 nm wavelength. The corresponding ground-state-absorption spectrum is shown in Figure 3.5. The S_1-state energy numbers to $E_{S_1,a} = 3.3\,\mathrm{eV}$ as obtained by spectroscopy taking the longest-wavelength absorption band. Using the shortest-wavelength fluorescent band instead, an energy of only $E_{S_1,f} = 2.6\,\mathrm{eV}$ results. Normally those two bands lie close to each other. For benzil, this huge difference is explained with the change of conformation between the skew dicarbonyl (SK) and the trans-planar (PL) configuration [121]. This suggests, that benzil's optical transition from its twisted ground state to a first excited state in skew configuration is followed by a rapid rearrangement into a first excited state in trans-planar configuration. That hypothesis is backed by the small difference in energy between fluorescence and phosphoresence [122].

After excitation from the ground state to S_1 by absorption of UV- or blue light, benzil shows only faint fluorescence with a quantum yield of less than

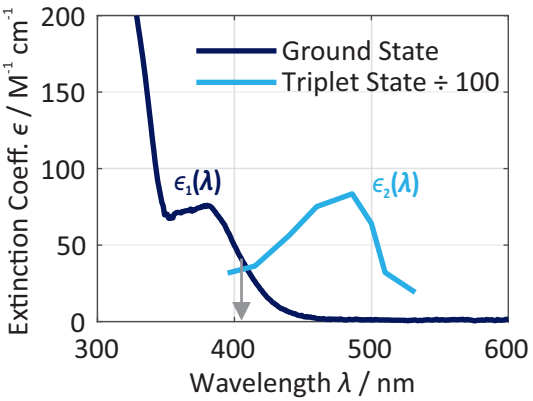

Figure 3.5: **Ground-state (dark blue) and triplet-state (light blue) molar decadic extinction coefficient of benzil.** Data for the triplet-state absorption are taken from Ref. [123]. It needs to be emphasized that the triplet-state extinction coefficient is scaled down by a factor of 100. Adapted from Ref. [31] with permission from Springer Nature.

$\Phi_F = 0.1\,\%$ [123] but in contrast with $\Phi_{ISC} = 92\,\%$ a high quantum yield for intersystem crossing to the energetically close triplet manifold [124]. The triplet ground-state energy is $E_T = 2.3\,eV$ as previously mentioned in Table 3.1. For T_1, the main deactivation channel is the radiationless reverse intersystem crossing while the radiative decay via phosphorescence plays a minor role with a quantum yield of only $\Phi_P = 0.3\,\%$ [119]. Since there is doubt on the direct reverse intersystem crossing $T_1 \longrightarrow S_1$ [125], a reverse intersystem crossing to a singlet state S_x is proposed [119].

Additionally, benzil allows for triplet-state absorption $T_1 \longrightarrow T_n$ with a maximum extinction coefficient of $\epsilon_{2,max} = 8 \cdot 10^3\,M^{-1}\,cm^{-1}$ at 480 nm wavelength. Remarkably, comparing both extinction coefficients at 405 nm, the triplet-state extinction coefficient is around a hundred times larger than the ground-state extinction coefficient. The triplet-state-absorption spectrum is plotted in Figure 3.5. It shows the overlap with the ground-state absorption which is inevitable for one-color two-step excitation. The excited triplet state has sufficient energy to decompose the molecule into two radicals [127–129] which is not achieved in the triplet ground state. However, benzil allows for hydrogen abstraction from its

Table 3.2: **Photophysical parameters of benzil.** The state energies E, the maximum wavelengths λ for the optical transitions together with the respective extinction coefficients ϵ, as well as quantum yields Φ for the main reaction pathways are given with their reference.

Singlet Parameters	Triplet Parameters
$E_{SK} = 3.3\,eV$, $E_{PL} = 2.6\,eV$ [121]	$E_T = 2.3\,eV$ [110]
$\lambda_{1,max} = 380\,nm$ [121]	$\lambda_{2,max} = 480\,nm$ [110]
$\epsilon_{1,405nm} = 40\,M^{-1}\,cm^{-1}$ [110]	$\epsilon_{2,405nm} = 4 \cdot 10^3\,M^{-1}\,cm^{-1}$ [110]
$\Phi_F = 9.4 \cdot 10^{-4}$ [123]	$\Phi_P = 3.1 \cdot 10^{-3}$ [119]
$\Phi_{ISC} = 0.92$ [124]	$\Phi_{RISC} < 3.1 \cdot 10^{-3}$ [126]

surrounding like from the monomer in its T_1-state terminating in free radicals [129, 130]. As discussed in section 3.4, additional quencher molecules like TEMPO or BTPOS can be added to the resist composition to effectively suppress these undesired side reactions.

In summary, benzil as a photoinitiator in combination with TEMPO or BTPOS as a quencher mixed in PETA as a common monomer forms a suitable photoresist for two-step 3D laser printing. The intermediate-state lifetime of benzil in such a resist is deduced to be $\tau = 80\,\mu s$ [31]. Approximating the voxel size with 160 nm as the calculated lateral full width at half maximum of a diffraction limited focus employing a 100 × / NA 1.4 microscope objective lens [131], this limits the print speed to about $v_{max} = 2\,mm\,s^{-1}$. Note that the rate equation calculations in Ref. [31] showed that the exposure time has to remain well above τ to obtain a nonlinearity exponent of $N \approx 2$. On the other hand, optical powers well below 1 mW are sufficient at such print speeds enabling the use of inexpensive and compact continuous-wave laser sources for excitation [31].

3.7 Alternative Two-Step Photoinitiators

Benzil is a well-established photoinitiator for two-step 3D laser printing and readily used [31, 103, 131]. Still, the hydrogen abstraction reaction from its intermediate state are adverse and require additional quencher molecules. Therefore, there is ongoing research on molecules possessing an inert intermediate state. Higher extinction coefficients and shorter intermediate-state lifetimes are also of great interest, possibly enabling faster printing.

We systematically survey further representatives of the group of ketones for their performance as two-step photoinitiator [132]. This work was predominantly performed by Maximilian Bojanowski and Aleksandra Vranic. Twenty-two alternative molecules having small modifications to already used benzil and biacetyl are investigated. Minor improvements can be achieved, yet no break-through until now. Still, suitable additional photoinitiator candidates for one-color two-step absorption, two-color two-step absorption, and newly, two-step absorption combined with a depletion mechanism are found. Furthermore, detailed and systematic studies help in better understanding two-step absorption to make use in 3D laser printing which is still in the early stages.

In addition, there are other possible candidates for two-step absorption. One of which is photochromic molecules which were reported in holography [133, 134] and lithography [25, 135–138]. The latter is commonly referred to as dual-color photopolymerization which was already proposed by Swainson [139] in the '70s. Here, the mechanism is mediated by a two-color photoinitiator which either inhibits or initiates the polymerization reaction after a photon of the first wavelength is absorbed. Often, a ring-opening reaction under UV-light exposure

is employed in a first step. The open-form isomer can further be excited by a second photon or reverts back to its original closed form. Research on different systems and their lifetime between microseconds to minutes is ongoing [140].

Alternatives to two-step absorption for 3D laser printing are the $(1+1)$-photon mechanisms employing upconversion luminescence [141, 142] and triplet-triplet annihilation [143]. A detailed discussion of their principles, advantages, and disadvantages is summarized in Ref. [100]. Additionally, chemical instead of optical nonlinearities can be applied to 3D laser print microstructures [144–146].

Chapter 4

4 A Shoe-Box-Sized 3D Laser Printer

All components that compose the shoe-box-sized 3D laser printer.

The utilization of two-step absorption as the excitation mechanism in 3D laser printing enables the use of low-power laser sources as presented in the previous chapter. This chapter discusses the design and implementation of a compact 3D laser printer at the size of a shoe box and analyses its performance.

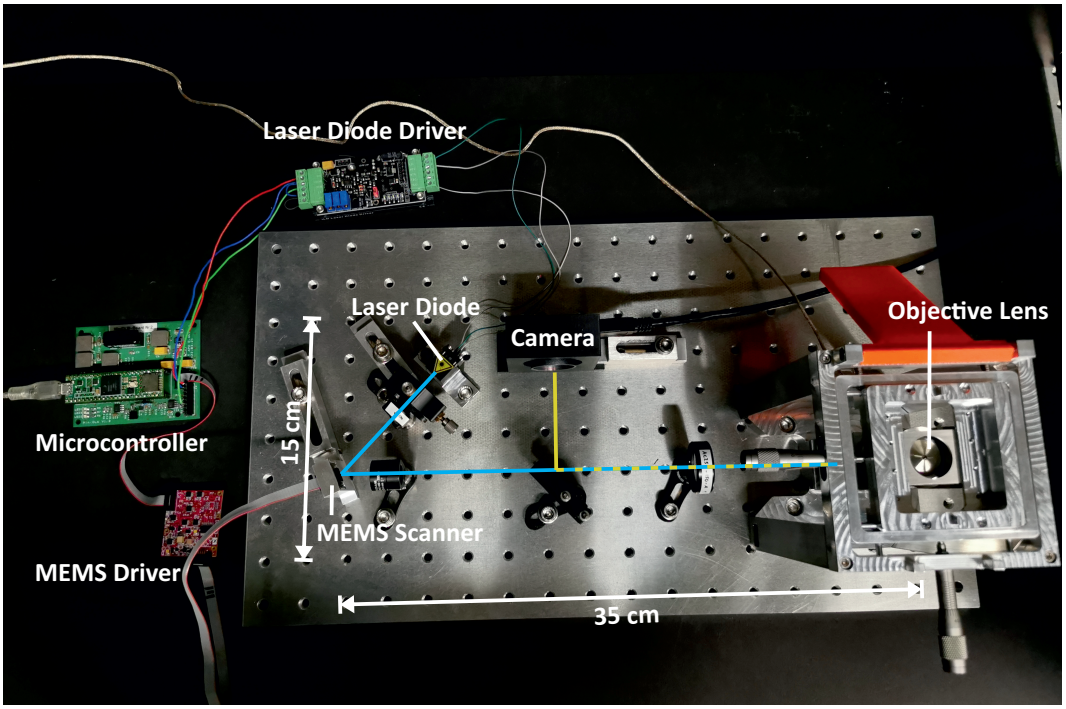

Figure 4.1: **Photograph of the shoe-box-sized 3D laser printer.** The main components are labeled and the optical beam path is depicted. With a total dimension of $35 \times 15\,\mathrm{cm}^2$ it fits well in a shoebox. The optical setup is mounted on a movable aluminum plate.

4.1 Compacting the Optical Setup

The setup of a common 3D laser printer and its components were discussed in section 2.1. The heart of every 3D laser printer is its light source. In a device utilizing two-photon absorption to trigger a polymerization reaction the light source is a femtosecond-pulsed laser. Their drawbacks feature high costs and a large size among other disadvantages of the high intensities in two-photon 3D laser printing. The previous chapter introduced two-step absorption as an alternative excitation mechanism and benzil as a suitable photoinitiator. As discussed, this allows for the utilization of low-power continuous-wave light sources which enables compact two-step 3D laser printers.

In general, four out of the five identified crucial elements (see section 2.1) relate to the optical setup: light source, power modulation, scan unit, and focusing unit. The overarching goal we set for our compact 3D laser printer is to minimize both the number of components and their cost, and at the same time to constrain the overall size of the printer to the size of a shoe box, while maintaining the previously achieved print quality and print speed with two-step absorption. A

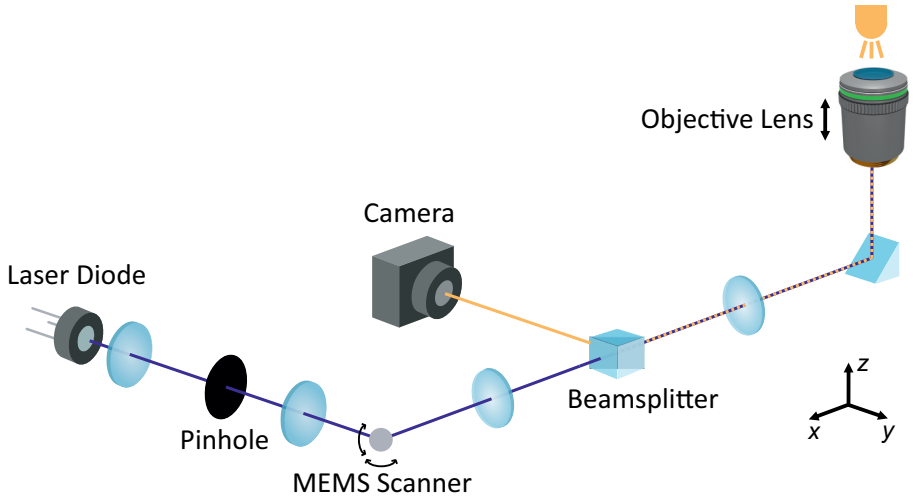

Figure 4.2: **Schematics of the optical beam path forming the shoe-box-sized 3D laser printer.** The divergent elliptical output beam (405 nm) of the low-cost edge-emitting semiconductor laser diode is spatially filtered by focusing through a 5 µm pinhole and collimated by a second lens. The 2D MEMS scanner deflects the laser beam along arbitrary 2D trajectories. The MEMS mirror is imaged onto the entrance pupil of a high-NA objective lens by the scan and tube lens. Additionally, they enlarge the beam to the desired diameter to fill the objective lens' entrance pupil. The objective lens is mounted onto a piezoelectric slip-stick stage for movement in vertical direction. Further, it focuses the laser into the liquid photoresist for printing and collects light of a transmission illumination simultaneously. The latter is separated by a beam splitter and detected by a camera for monitoring of the printing process. Adapted from [131].

photograph of the final setup is shown in Figure 4.1 while Figure 4.2 additionally shows a schematic of the beam path.

4.1.1 Light Source

The shoe-box-sized 3D laser printer builds on a continuous-wave edge-emitting semiconductor laser diode (LD-405-200MGS, Roithner Lasertechnik GmbH). It operates in single mode with a maximum optical output of 200 mW and a center wavelength of 405 nm. The laser diode is packed in a 3.8 mm transistor outline package (TO-can). Panel **a** of Figure 4.3 shows the tiny laser diode in size comparison to the laser head of a femtosecond-pulsed laser oscillator which is frequently used for custom two-photon lithography setups. The laser diode comes at a cost of only 38 € compared to the mentioned around 100 000 Euros for tunable femtosecond-pulsed lasers.

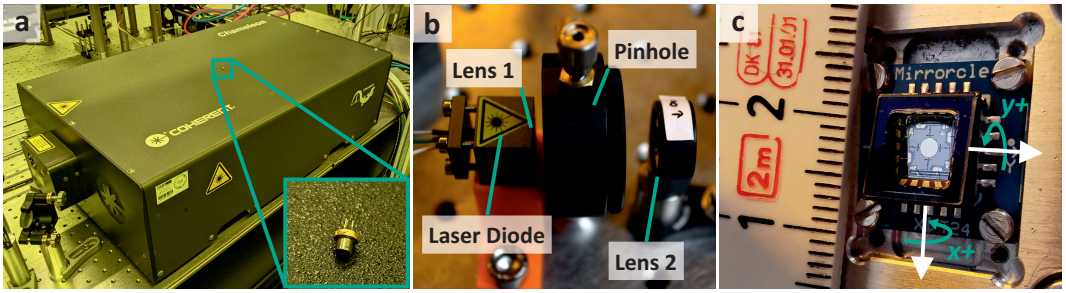

Figure 4.3: **Close-up photographs of selected crucial elements. a** Size comparison of the tiny laser diode as the shoe-box-sized 3D laser printer's light source and a femtosecond-pulsed laser oscillator as used in many home-built two-photon lithography setups. **b** Spatial filtering unit, where the elliptical output beam of the laser diode is focused through a 5 µm-sized pinhole by the first lens and collimated by the second lens at a beam diameter of 1.6 mm for further usage in the optical setup. **c** Detailed view of the MEMS scanner package with the 1.6 mm diameter aluminum-coated mirror in the center and a metric ruler on the side. The TINY20.4 package comprises the mirror, the mirror actuators, and an AR-coated protection window. Both rotation axes are indicated. Adapted from [131].

Being incorporated in optical pickup units of blue-ray players and gaming consoles [147–150] these InGaN laser diodes are mass-produced and the price per piece can easily get into the even single-digit Euro range for large amounts. Not only the built-in laser diode but even the full optical pickup units were employed for lithography [150–153] or other applications [154–158] due to their compact design and low cost. However, they only provide a rather small numerical aperture of NA = 0.85 [159] and come without a scan unit. Therefore, a pure laser diode is used instead of an optical pickup unit for the shoe-box-sized 3D laser printer and the remaining optical setup is customized.

The overall optical setup is designed for a minimum beam height. The smallest commercially available posts together with the smallest lens holders for 1/2 inch optics lead to an optical beam height of 36 mm. This favors stability of the system against vibrations but also exacerbates the use of some alignment tools and the utilization of other holders and components. The setup is built on a 1 cm thick aluminum plate which allows for moving the entire setup at once and mount it on an additional breadboard. This ensures flexibility and retains to employ alignment tools requiring larger beam heights.

In contrast to our first experiments on two-step 3D laser printing [31], the laser diode is mounted on a non-temperature-controlled laser mount (LDM-38, Lasertack GmbH) to study the necessity of a temperature control for high-resolution 3D printing. To match the desired beam height, the laser diode output height is fitted by an additional base for the mount.

Not only the beam height but also the beam shape needs to be adjusted. A

drawback of edge-emitting laser diodes is their elliptical output beam. The divergence angles usually range from around 5 deg to 15 deg in parallel orientation to about 15 deg to 25 deg in perpendicular orientation. The influence of the elliptical beam shape on high-resolution 3D laser printing is investigated and results will be discussed in section 4.3. One possible way to elude this problem is to fiber-couple the laser diode. Fiber-coupled laser diodes with integrated diode driver are commercially available and already used for two-step 3D laser printing [103]. However, they come at a cost of more than three thousand Euros. In our work, we decided to stay with the second solution: to spatially filter the elliptical beam by focusing it through a pinhole with an adequate diameter. This method was already employed in our first printer [31] and comes along with the advantage to easily remove the pinhole in case it turns out to be dispensable for good printing results.

Instead of collimating the beam, the first lens (C151TMD-A, Thorlabs) focuses it onto a pinhole with a diameter of 5 µm (P5HW, Thorlabs), from where it is collimated by a plastic aspheric lens (36-629, Edmund Optics) with a focal length of 18 mm. A photograph of the configuration is shown in panel **b** of Figure 4.3. One important constraint for the first lens is the desired beam diameter of $d_{1/e^2} \approx 1.6\,\text{mm}$ due to the limitations of the employed scan unit. This increases the natural divergence of the beam unintentionally and a short optical path is favored. Another restriction is the rule of thumb to pick the lens such that $\text{NA}_{\text{lens}} > 2 \cdot \text{NA}_{\text{LD}} = 2 \cdot 0.17$ is met [160]. Thus, the first lens has a numerical aperture of $\text{NA} = 0.5$ and a focal length of only 2 mm. This demands for special mounting implemented into the laser diode mount to get close enough to the window of the laser diode housing.

Crucial for the efficacy of the spatial filtering is the diameter and the exact positioning of the pinhole in the focal spot of the lens configuration. Calculations result in a required diameter of the pinhole of less than 10 µm, why we employ a diameter of 5 µm. To optimize the location, the position of the pinhole is changed by hand in steps of 1 mm starting from being in contact to the laser diode mount – which is the closest possible distance to the first lens. For each step, both the difference of the beam diameter in x and y, as well as the transmitted optical power are measured. The beam diameters are evaluated with a Shack-Hartmann wavefront sensor (WFS30-7AR/M, Thorlabs) driven close to its limits due to the small beam diameter. For measuring the transmitted optical power, a standard silicon photodiode is employed. The optimum position is reached, when the measured transmitted power is at its maximum and the difference in beam diameter is close to zero. The measured values are plotted in Figure 4.4.

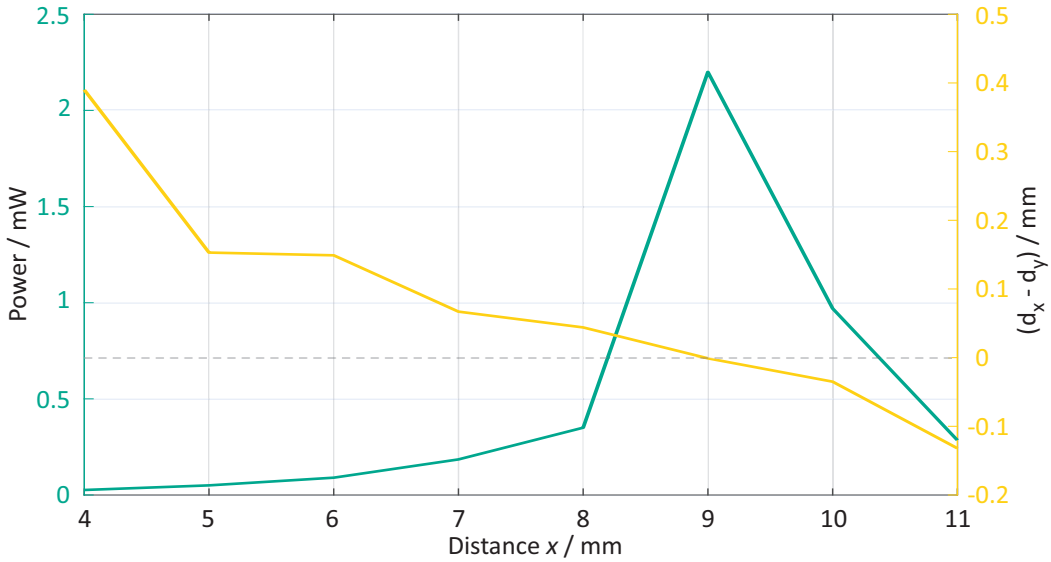

Figure 4.4: **Plot of the measured power throughput and difference in beam diameter for position optimization of the pinhole.** The pinhole is moved in steps of 1 mm starting from the closest possible distance to the first lens, corresponding to a distance of $x = 4$ mm. For each step, the power throughput is measured by a photodiode (green). The procedure can be stopped as soon as the maximum power is reached. Here, the pinhole is in the focal plane of the first lens. In parallel, the beam diameter in x and y direction are traced (yellow). At the focal plane, a perfect circular shape is expected, thus a value of zero in the used metric of the difference in the two lateral beam diameters.

4.1.2 *Power Modulation*

For 3D laser printing, the laser output needs to be modulated. Obviously, a high-speed shutter is needed and a fine tuning of the power is desirable to obtain best print results. Conveniently, the optical output of a laser diode can directly be adjusted by modulating the input current. Thus, the laser diode itself can be exploited as a shutter and power modulator at no cost. This obviates additional components like commonly used expensive acousto-optic modulators. Their advantage, however, is an extremely fast modulation which is only limited by the transit time of the acoustic wave within the crystal typically ranging from about 5 ns to 100 ns.

Therefore, we measure the temporal response of our laser diode with the help of a digital oscilloscope. One channel is connected to the modulation output channel of the control unit while a second channel is linked to an avalanche photodiode inside the optical beam path. The resulting oscillogram is shown in Figure 4.5. It reveals a constant delay time of about 13 µs and a rise time of around 5 µs. This is orders of magnitude larger than the modulation frequency of an acousto-optic

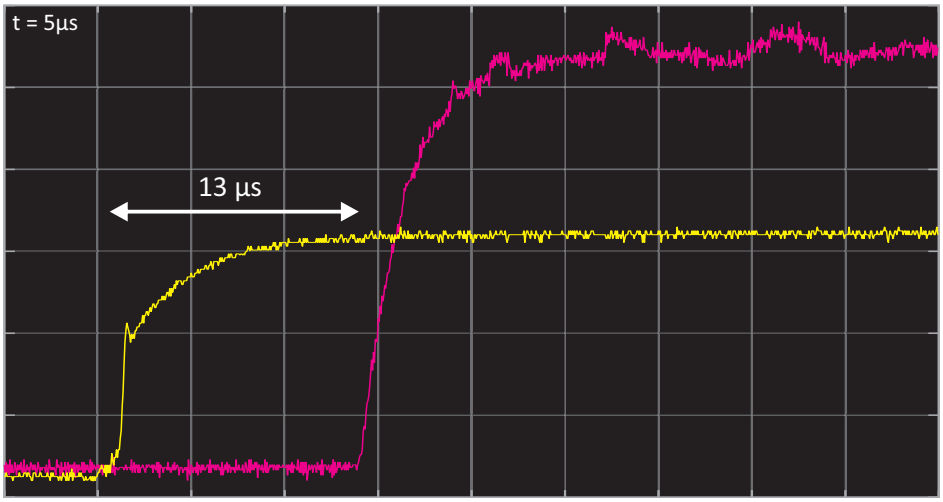

Figure 4.5: **Oscillogram of the temporal response of the laser diode.** Channel 1 (yellow) of a digital oscilloscope is connected to the modulation output channel of the control unit to identify the time at which the control unit outputs the electronic signal to the laser diode driver. The resulting optical output is measured by an avalanche photodiode which is placed in the optical path with additional neutral density filters to prevent damage of the diode. The measured signal from the photodiode is connected to channel 4 (magenta) of the oscilloscope. One scale on the x-axis corresponds to 5 µs. With this measurement setup, the temporal delay between the electronic output to the laser diode driver and the optical output of the laser diode can be deduced. The delay is measured to be around 13 µs.

modulator. However, at a common print speed of 1 mm s^{-1} the delay results in a constant misalignment of around 13 nm only. Additionally, comparing it with the 80 µs intermediate-state lifetime of benzil which limits the print speed anyway the delay time is not disrupting the 3D laser printing. Still, it has to be considered for synchronization with the scan unit.

4.1.3 Scan Unit

As discussed in Figure 2.1, there are three main methods for the scan unit. Here, we exploit 2D scanning of the laser beam employing a two-axes tip-tilt MEMS scanner (F1M16.2-1600AL, Mirrorcle Technologies). A close-up camera picture is shown in panel **c** of Figure 4.3. This solution is cheaper, more compact, and involves less components than scanning by galvanometric mirrors. Additionally, the internal electro-static acutators for such MEMS scanners dissipate less than a few milliwatts of power even at continuous full-speed operation [161] which allows for a low-power control unit as we will discuss later.

The low power consumption is achieved by Mirrorcle's bias-differential quad-

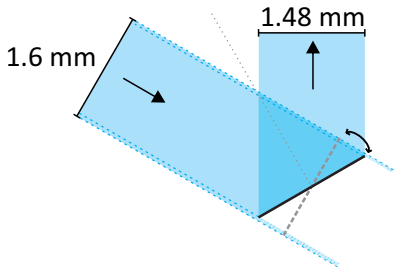

Figure 4.6: **Scheme of the beam clipping at the MEMS scanner.** Due to the angled incidence of the beam, not the full diameter of the MEMS mirror of 1.6 mm can be used. Instead, only a beam with 1.48 mm diameter will result for an incidence angle of 22.5 deg.

channel technology. Here, each of the two axes is rotated by two actuators at opposite sides. In neutral position, both actuators are biased with an applied potential of 90 V. For a certain tilt around one axis, the potential on one of the two actuators is lowered while the potential on the other actuator is increased by the same value originating in a voltage difference. In contrast, galvanometric mirrors employ the force on a rotatable magnet by a current-carrying coil. Operating them at high frequencies on a long-term, therefore, requires external cooling of the system [5] which is why we do not utilize them. The low power consumption due to the working principle is assisted by the tiny mirror, hence, small mass to be moved.

Our aluminum coated mirror of the MEMS scanner possesses a diameter of 1.6 mm only, which is the aforementioned restriction to the beam size. The measured $1/e^2$ beam diameter after the second lens amounts to 1.67 mm, therefore slightly over-illuminating the mirror as intended. They are designed for best performance at an incidence angle of 22.5 deg. Due to this angled incidence, the laser beam is clipped to $D_{\mathrm{max},1/e^2} = 1.48\,\mathrm{mm}$. The principle is shown in Figure 4.6 in a simplified scheme.

The mirror is directly integrated in the actuator device and monolithically fabricated [162]. The maximum mechanical angle for both directions is around ± 4.7 deg resulting in an optical scan angle of almost ± 10 deg. The angular resolution amounts to 0.6 mdeg for simultaneous gimbal-less beam steering in two dimensions. The resonance frequency of both axes is 2.3 kHz. The mirror and actuator device come mounted in the TINY20.4 package concluding the overall size of the mirror device to $15 \times 15\,\mathrm{mm}^2$. The connector to the MEMS driver is at the rear side while the mirror at the front side is covered by a wedged and AR-coated protection window.

The scan unit further comprises a compact linear piezoelectric stage (LPS 30-30-1-V3_O-S-N, NANOS-Instruments) for scanning in the third dimension, i.e. the z-direction. The piezoelectric stage is based on the slip-stick mechanism which combines small incremental steps with long travel ranges at high precision. Our

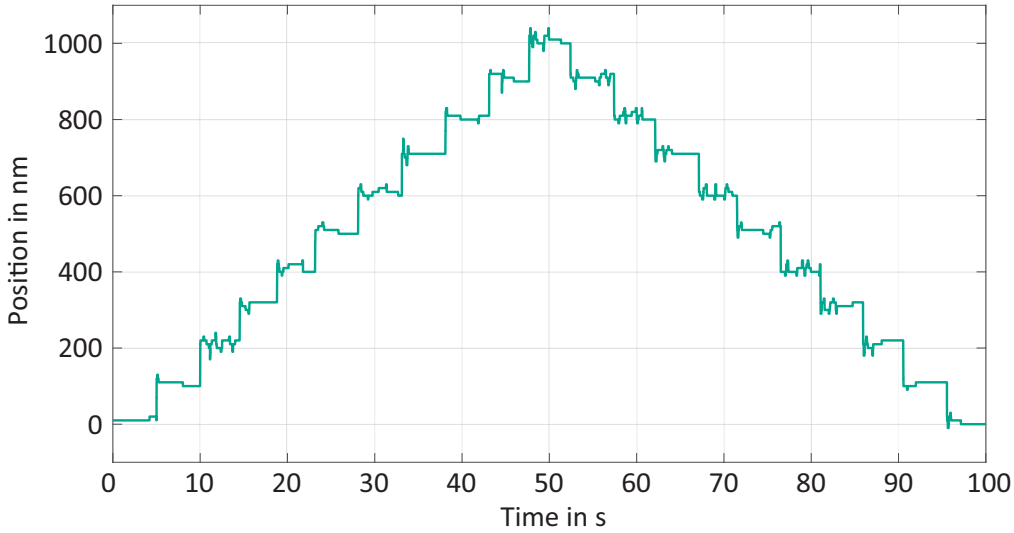

Figure 4.7: **Typical 100 nm step pyramide of the linear piezoelectric stage.** The used step-up and step-down routine is implemented in the software of the stage as provided by NANOS-Instruments. Here, it is run after optimizing the stage settings with 10 steps of 100 nm each and a delay time of 2 s. These values match the used 100 nm steps for slicing during printing and a common period for the printing of one layer. Only small fluctuations and overshoots within maximum three steps, i.e. 30 nm, around the desired position are visible. These deviations are rather small compared to the larger than 300 nm axial voxel size. No fluctuations of the height can be seen in the print results shown later in this chapter. Thus, a stable and precise positioning is ensured. Adapted from [131].

stage allows for a travel range of 15 mm with a minimum incremental step size of 10 nm. This leads to the amount of 1.5 million possible steps of 10 nm each. Thus, both coarse movements like approaching a sample and fine movements like the commonly used 100 nm slicing can be achieved with a single device.

The stage settings are fine-tuned for the application in 3D laser printing. Typical movements like the 100 nm steps for slicing during printing require fast step-settling without pronounced overshoots. Therefore, high values for maximum speed, acceleration, and deceleration are beneficial. By boosting these values too much, the stage gets into an unstable resonant mode causing large vibrations. Thus, a trade-off needs to be found. Additionally, position stability without any movement is of importance and also taken into account. A typical 100 nm step pyramide after optimization of the stage parameters is shown in Figure 4.7.

Since the 2D MEMS scanner only allows for scanning within the field of view of the focusing unit, a compact self-designed coarse stage is added to the setup as a mount for the sample. The CNC-drilled stage employs two micrometer screw gauges for manual movement in x- and y-direction enabling multiple structures

on the same sample with a precision in positioning of 1 µm having a steady hand.

4.1.4 *Focusing Unit*

For high-resolution 3D laser printing, the laser needs to be focused by a high-NA microscope objective lens. This results directly from the diffraction limit formula (see Figure 2.1). Such objective lenses are highly engineered lens groups correcting for various aberrations. However, they only achieve their maximum focusing power in case of a full illumination of their entrance pupil. Thus, they commonly are even slightly overilluminated for best performance in practice. Typical diameters for the back aperture for such lenses are around 5 mm. Therefore, the diameter of the laser beam needs to be expanded from the 1.5 mm behind the MEMS scanner to the respective diameter of the objective's entrance pupil.

Frequently used are 100 × / NA 1.4 oil immersion microscope objective lenses. They provide highest resolution both for microscopy or 3D laser printing. For the shoe-box-sized 3D laser printer, we use the same objective lens as in Ref. [31], a Leica HCX PL APO 100 × /1.4 − 0.7 Oil CS with the adjustable NA set to its maximum of NA = 1.4, to allow for direct comparison of the print results. Its diameter of the entrance pupil amounts to 5.6 mm. However, it comes at a cost of around five thousand Euros being one of the main cost drivers of a common 3D laser printer after the femtosecond laser. Thus, we test a second lens (EC PL 100 × /1.25 Oil, Motic) with a slightly smaller numerical aperture of NA = 1.25 but at a cost of only 140 € to investigate the influence of the lowered NA on the performance. The Motic lens comes with an entrance-pupil diameter of 4.5 mm.

Both objective lenses were characterized with respect to their achievable focus size. The employed setup bases on the one assembled by Joachim Fischer in 2011 [163] and was changed several times over the years. The latest large rearrangement was conducted in 2020 by me and Vincent Hahn. A detailed description can be found in Ref. [98]. To measure the point spread function, a sample containing 80 nm gold nanoparticles is used. We raster scan the laser focus within the *xy*-, *xz*-, and *yz*-plane over a single gold nanoparticle and measure the back-scattered light with a photodiode. This yields a reconstruction of the intensity profile of the laser focus in all three dimensions. The respective lateral and axial full width at half maxima (FWHM) can be deduced.

The resulting 2D intensity profiles for both objective lenses with their lateral and axial FWHM are shown in Figure 4.8. An increase in FWHM especially in axial direction is clearly visible but at the same time expected due to the lowered NA. In addition, alignment of this setup is very convenient with the help of the reconstructed light distribution. A tilt of the beam would directly translate to a tilt of the reconstruction and collimation can be optimized by reducing the tails of

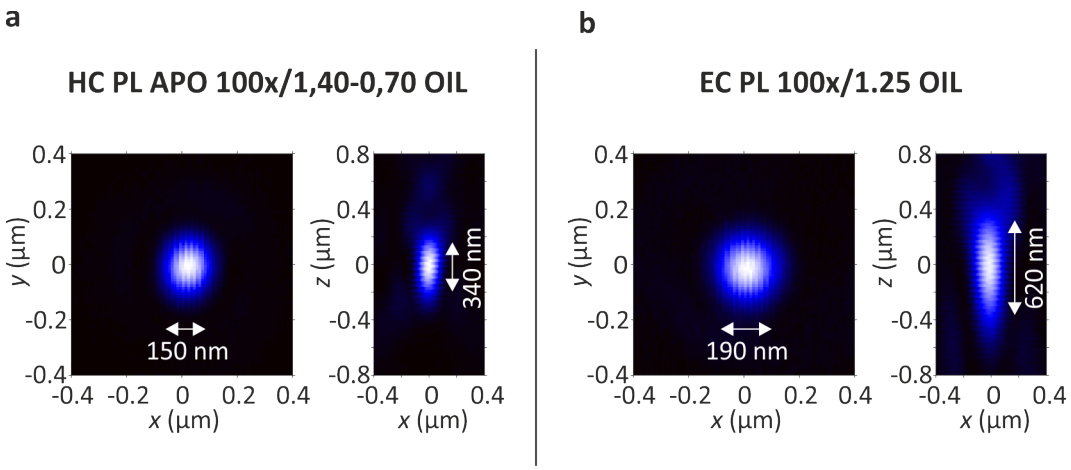

Figure 4.8: **Two-dimensional intensity profiles of the laser focus for the two microscope objective lenses. a** Leica HCX PL APO 100 × /1.4 − 0.7 Oil CS objective lens and **b** EC PL 100 × /1.25 Oil objective lens. To obtain the intensity profiles, the laser is raster scanned in in the *xy*-, *xz*-, and *yz*-plane across a gold nanoparticle. The resulting back-scattered light is detected by a photodiode and plotted. The calculated lateral and axial FWHM is depicted in the corresponding plot. Adapted from [131].

the reconstruction. Therefore, a focus measurement for the shoe-box-sized printer would ease the alignment as well but is not yet implemented.

For better comparison of the achieved lateral and axial FWHM, theoretical values for the point spread function are calculated by using the modified Richards & Wolf integrals [164] following the routine implemented by Richard Wagner [79]. The results are shown in Figure 4.9. All experimentally obtained values fit nicely to the calculations besides the axial FWHM for the lower-NA objective lens. This worse performance could be addressed to a less optimized lens group in case of the cheap objective lens but still is sufficient for most 3D laser printing applications being below 1 µm.

A second constraint to the remaining optical path is that the MEMS mirror has to be perfectly imaged onto the entrance pupil of the objective lens in a $4f$-configuration such that a tilt of the mirror translates to a displacement in the focal plane of the objective lens. The two lenses of this standard configuration are mostly referred to as *scan* and *tube* lens (see Figure 4.2) and often comprise a whole lens group each instead of a single lens [5, 96].

The most compact design is achieved by merging the two required lens systems for beam expansion and imaging of the MEMS mirror. Thus, a magnifying Keplerian telescope is used. Here, we employ achromatic doublet lenses for both scan (AC127-025-A-ML, Thorlabs) and tube (AC254-150-A, Thorlabs) lens. The magnification is determined to match the required beam expansion for a slight overillumination and a conservative calculation using the beam diameter at full

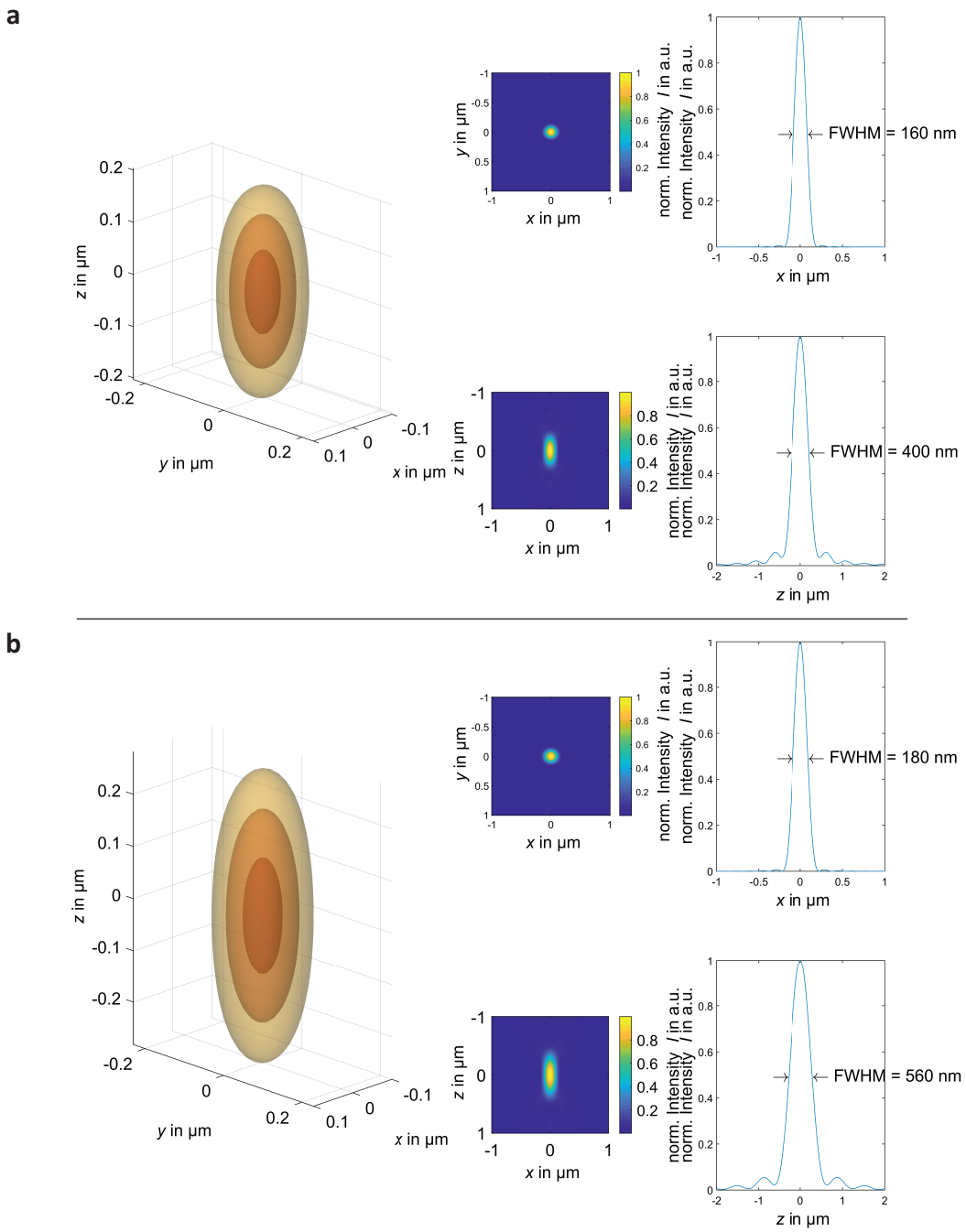

Figure 4.9: **Calculated point-spread-functions for the Leica NA = 1.4 (a) and the Motic NA = 1.25 (b) objective lens.** The underlying intensity distributions are calculated following the routine of Richard Wagner [79] using the modified Richards & Wolf integrals [164]. On the left side, the 3D iso-intensity surfaces at 90 %, 70 %, and 50 % of the maximum intensity are plotted. The center column shows 2D intensity cuts comparable to the measured 2D cuts in Figure 4.8 of the xy- (top) and xz-plane (bottom), respectively. On the right side, 1D cuts along both x- (top) and z-axis (bottom) are shown. The corresponding FWHM is calculated and indicated in the 1D plots. Adapted from [131].

width at half maximum instead of the one for $1/e^2$ resulting in $M = 6$. Therefore, focal lengths of $f_{\text{scan}} = 25\,\text{mm}$ and $f_{\text{tube}} = 150\,\text{mm}$ are selected.

The focal lengths of the two lenses limit the minimum outer dimensions of the compact 3D laser printer as they constitute the majority of the overall optical path length. The obvious optimization is to define these 350 mm along the diagonal of the printer. Real reduction of the printer size can be achieved in two ways though: First, it is convenient for application that the objective lens is mounted vertically. The obtained vertical optical beam path directly reduces the horizontal beam path, thus, decreasing the footprint of the 3D laser printer. A compromise must be found since increasing height also increases instabilities against vibrations as discussed. Second, beam folding would allow for additional miniaturization of the setup. However, this involves additional components and the alignment of the setup would render less convenient why we decide against it.

4.1.5 Additional Components

For convenience, the optical unit of the shoe-box-sized 3D laser printer comprises further components besides the crucial elements. One of them is a camera to real-time monitor the printing process. Therefore, a small light emitting diode (LED570L, Thorlabs) is placed on top of the stage illuminating the sample at a center wavelength of 570 nm. Note, the exploited wavelength has to be well above the ground-state absorption of the photoinitiator not to cause any polymerization. The light is collected by the focusing objective lens in transmission and separated between scan and tube lens using a chromatic beamsplitter (RGB-Strahlteiler, Lasertack GmbH). The camera (Chameleon3, Teledyne FLIR) is placed in the conjugated plane of the entrance pupil of the objective lens to display the focal plane.

Besides monitoring, the camera is also utilized for finding the right interface between substrate and liquid photoresist. This is important to nicely attach the printed structure to the substrate. One part of the master thesis of Jingya (Lilyn) Gao, which was supervised by me, was to implement an interface finder routine [165]. There are different options for a successful detection of the interface. The routine can either base on back-reflected light of the 405 nm excitation laser due to the refractive index difference of the substrate and the photoresist, or on fluorescence of the photoinitiator molecules. Additionally, the respective light can either be detected by the monitoring camera or by a separate photodiode.

The preferred solution is the detection of the vanishing amount of back-scattered light of the laser leaking through the beamsplitter as detected by the camera since no further components are required. Such an interface finder routine is successfully implemented. The routine scans the objective lens along the z-direction while the laser is turned on. A region of interest is defined in the camera picture and the

brightness values for each pixel is summed up. The maximum value of this sum is reached at the brightest spot, i.e. when the focal position matches the interface. The overall routine only takes some seconds which is well suitable for permanent usage during printing. It needs to be stressed, that during this procedure none of the pixels of the camera should be saturated. Hence, additional neutral density filters might be suitable. Further details are presented in Ref. [165].

4.2 A Compact Control Unit

While the heart of the shoe-box-sized 3D laser printer is the optical setup, its brain – the control unit – was not yet discussed. Usually, this comprises a lab computer and a rack full of bulky and expensive components such as controllers and power supplies. In contrast, we set the goal to compact not only the optical setup but also the control unit to acquire a compact and stand-alone setup.

The core of our control unit is an inexpensive but extremely powerful microcontroller (Teensy 4.1, PJRC). It is available for only 31 € with soldered pins and is based on an ARM Cortex-M7. The Teensy 4.1 possesses 55 digital input/output pins, 35 pulse-width modulation output pins, and 18 analog output pins. Additionally, the microcontroller has 3 serial peripheral interface (SPI) ports. Together with additional electronic components for example for voltage transformation, pin connections, or digital-to-analog conversion, it is mounted on a home-made printed circuit board (PCB).

The microcontroller serves as master for the compact 3D laser printer and as interface to a lab computer. The latter is connected via USB to transmit print job files and additional commands prior to printing, to monitor the printing process, and to provide electrical power for the Teensy 4.1. On the output side, the microcontroller is connected to the digital MEMS driver and the laser diode driver completing the simple version of the control unit. A photograph of the components with a metric ruler to better assess the sizes of the components is shown in Figure 4.10.

The common workflow in 3D laser printing was discussed in section 2.2. Most of it is mimicked and optimized for the operation on a microcontroller in a powerful code which is in-house developed and predominantly written by Michael Hippe. Early stages of the code were written by Andreas Naber during the Bachelor thesis of Philipp Ohl. Here, the proof of principle of controlling the MEMS scanner via a microcontroller has been demonstrated. A flowchart of the connections and conversions in the final setup is shown in Figure 4.11. The starting point builds a job file containing all points of the trajectories to be printed with four values each: x-, y-, z-coordinate, and the desired laser power at this point. This structure is common for other home-made 3D laser printers and ensures good compatibility

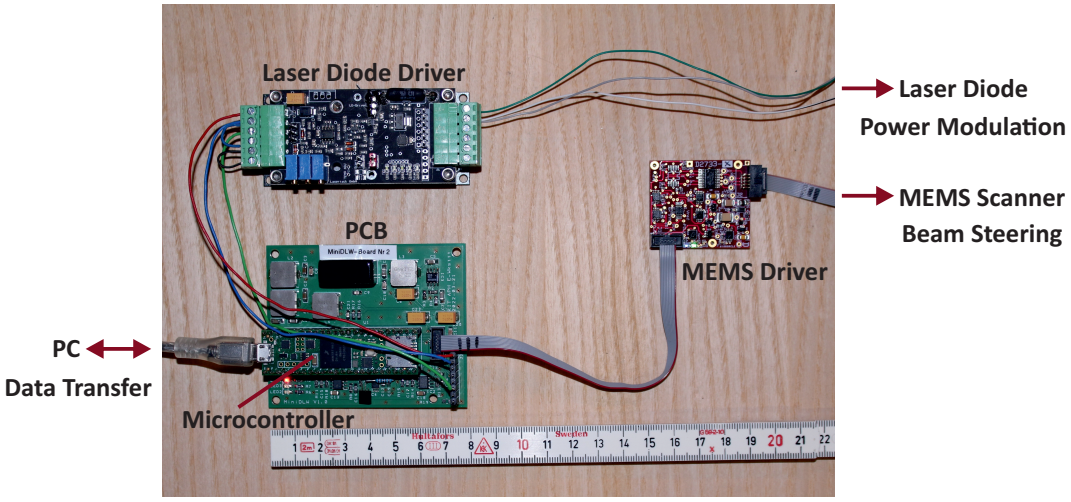

Figure 4.10: **Photograph of the compact control unit of the shoe-box-sized 3D laser printer.** The Teensy 4.1 microcontroller is the core of the control unit. It is mounted on a home-built printed circuit board (PCB) and is connected to the PC via USB for data transfer, to the MEMS driver, and to the laser diode driver. The digital output values for both MEMS scanner and laser diode are converted into analog voltages via digital-to-analog converters (DAC). One of them is included in the digital MEMS driver. Thus, it converts the digital input of the microcontroller into the high voltage signal for the four channels of the MEMS scanner for 2D beam steering. It is directly connected to the TINY20.4 package of the MEMS scanner. The second DAC is mounted on the PCB and applies its analog output signal to the pin connector on the bottom right of the PCB. The corresponding pin is connected to the modulation input of the laser diode driver. The latter is connected to the laser diode and converts the input modulation voltage to the corresponding drive current for the laser diode for optical power modulation. Adapted from [131].

of job files. The coordinates correlate with the desired position of the laser focus in the focal plane. Already small and simple structures can easily get to thousands of these points for smooth trajectories.

Additionally, the job file contains header lines where printing parameters like print speed or laser power – in case of not being defined in the points directly – are given. Therefore, the microcontroller program not only comprises the conversion calculations for the data points but also lots of additional commands and preset parameters for controlling the components of the 3D laser printer off the print. Examples are the update rate of the system, the conversion factors from positions in the job file to tilt angles of the MEMS scanner, the default excitation power if none is explicitly set in the job file, or other default values like the filter clock frequency of the digital MEMS driver.

The job file is transferred from a computer to the microcontroller via USB.

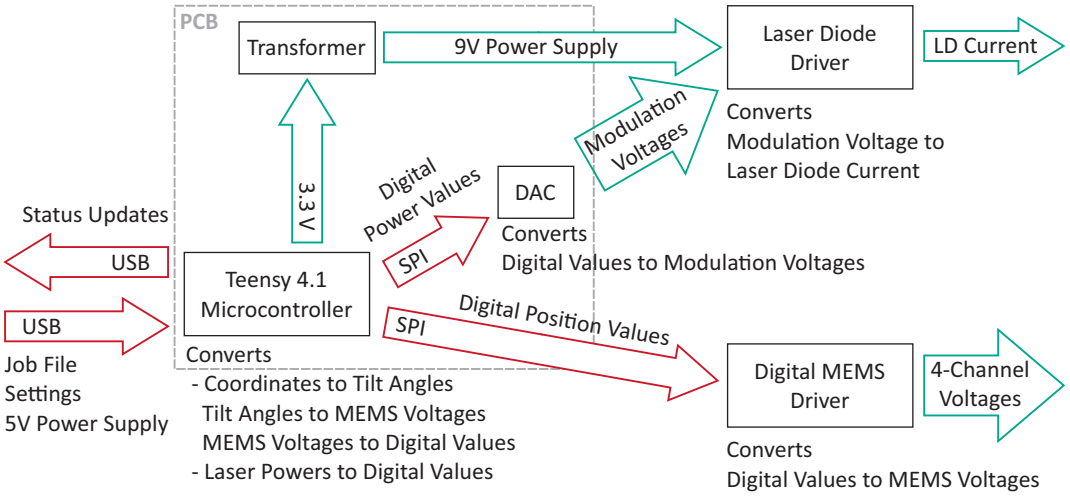

Figure 4.11: **Flowchart of the control unit.** Red arrows indicate digital data transfer, while green arrows indicate analog data transfer. The home-made printed circuit board (PCB) is indicated by the gray rectangle to show which components it comprises. The conversions performed by the different components are written underneath.

Here, we use a small MATLAB script on the lab computer. The Teensy 4.1 directly interpolates the points to connecting lines and converts them into digital values for the MEMS driver, accounting for the defined print speed. These converted values are buffered in the on-board memory of the microcontroller. To enable larger structures, hence, more data points, two additional 8 MByte dynamic random-access memory modules are soldered to the microcontroller. All together they allow for more than 600 000 points, i.e. lines with values for the three dimensions and the laser power. The pre-loaded print job can be started by sending 'run' as a text command to the microcontroller.

From this stage, printing runs in principle autonomously controlled by the microcontroller and certain feedback is returned to the computer for monitoring. One of which is important if not only a flat 2D structure like line gratings is to be printed but a real 3D structure. After a single layer is printed, the microcontroller returns a command to signal the end of the layer. This command is important for the change in z-position by the objective lens mounted on the small piezo stage. Until now, the control of the piezo stage is not implemented into the microcontroller code. Still, we already checked the feasibility of an implementation to the microcontroller and did several arrangements for the implementation. There is an option for a small PCB-controller of the stage. The required inputs can be generated by the microcontroller together with small additional electronics like voltage transformations. These electronics would be similar to what is already done on the home-made PCB for the laser diode driver and the digital MEMS driver. Also, the capacity of the Teensy 4.1 processor allows for the control. Until

then, the small MATLAB program on the lab computer supersedes the control of the piezo stage.

However, within a layer and when printing only single layer structures, the microcontroller controls the entire printing process. For that, the position values are transferred to the digital MEMS driver via SPI. In more detail, the xy-position output to the MEMS driver comprises four digital values each to address all four channels of the the bias-differential quad-channel technology of the MEMS scanner (X+, X-, Y+, and Y-). These values are further converted into output voltages in the range of $0 - 180\,\mathrm{V}$ by the DAC on the digital MEMS driver. The output voltages in turn are transferred to the MEMS scanner. Applied to the actuators, the output voltages lead to the desired tilt of the mirror. Thus, the position coordinates in the job file have to be converted into the respective tilt of the MEMS scanner via different intermediate steps which is all performed by the microcontroller in an open-loop control.

Simultaneously, the corresponding laser power of the current position needs to be sent to the laser diode. Here, another digital value is sent via a second SPI connection to a separate DAC on the home-made PCB. A digital output is used instead of an analog output of the microcontroller, because the analog outputs work on the pulse-width modulation principle. This could lead to undesired fluctuations of the laser power. The DAC in turn converts the digital output into a stable output voltage and applies it to the pin connector on the bottom right of the PCB.

The respective pin is connected to the modulation input on the laser diode driver (PD-01359, Lasertack GmbH). It converts the input modulation voltage to current for driving the laser diode. The output is directly connected to the laser diode. To enable this conversion, the driver requires a 9 V power supply and grounding. Both is provided by the microcontroller and accessed from other pins of the pin connector. The 9 V potential is transformed from the 3.3 V internal potential of the Teensy 4.1 on the home-made PCB. We want to emphasize that with that, both the high voltage output for the MEMS scanner and the laser diode is fully powered by the 5 V USB connection of the microcontroller. This also gives evidence about the low power consumption of the shoe-box-sized 3D laser printer.

4.3 Performance Tests

The compact and optimized design of both the optical setup and the control unit is a great achievement yet worthless depending on the performance of the system as a 3D laser printer. To evaluate the printing performance, we print different three-dimensional structures with special demands on the printer. Two challenging structures which are regularly used for performance evaluation are a chiral mechanical metamaterial unit cell [166] and the #3DBenchy [167]. The

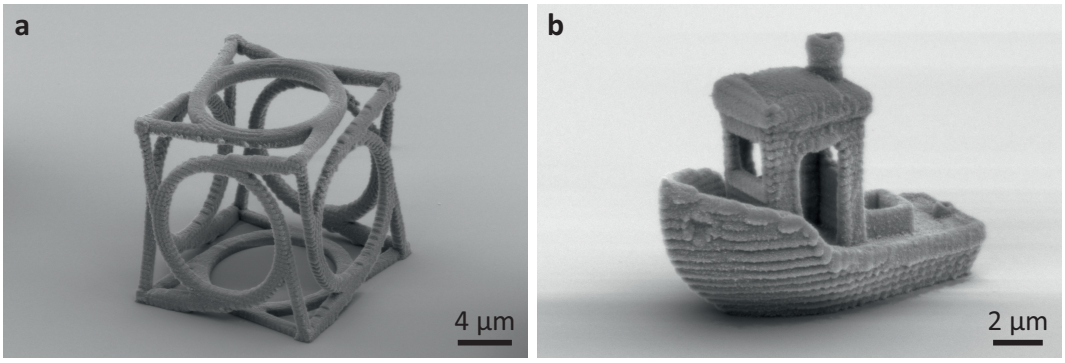

Figure 4.12: **Scanning electron micrographs of two selected challenging 3D structures printed after system optimization.** **a** One unit cell of a chiral mechanical metamaterial [166] with a dimension of $16 \times 16 \times 16\,\mu m^3$. **b** The #3DBenchy structure [167] with a dimension of $15 \times 8 \times 12\,\mu m^3$. Both structures are printed with a focus speed of $1\,mm\,s^{-1}$ while employing a hatching and slicing distance of 50 nm and 100 nm, respectively. The laser power is set to 700 µW for the metamaterial structure and 400 µW for the #3DBenchy as measured at the entrance pupil of the objective lens. Adapted from [131].

metamaterial unit cell has a very fragile architecture resulting in an extremely small filling fraction. We use a common dimension of the unit cell of $16 \times 16 \times 16\,\mu m^3$ [31]. In contrast, the #3DBenchy comprises a bulky hull with a very high filling fraction and additional fine features like the cabin. The dimensions of the #3DBenchy number $15 \times 8 \times 12\,\mu m^3$. For maximum comparability, the same resist system as used in previous work [31] is employed comprising benzil as a photoinitiator with BTPOS as a quencher mixed in TMPTA as the monomer [131].

Scanning electron micrographs of the printed structures with the optimized system are shown in Figure 4.12. They show comparable quality to the structures printed with the highly optimized setup in Ref. [31], evidencing an overall good performance of the shoe-box-sized 3D laser printer. All fine features are nicely resolved. Further, only a minor proximity effect can be observed at the roof of the #3DBenchy although high filling fractions are challenging for two-step 3D laser printing in general [31]. However, there are many parameters highly affecting the quality of the structures as explained in the following.

4.3.1 *Influence of Spatial Filtering*

The spatial filtering and its influence on the beam quality was discussed in subsection 4.1.1. In a set of experiments, its impact on the print quality is investigated. In case of no spatial filtering, i.e. no pinhole or one where the diameter is too large, we expect the elliptical beam shape to translate into an elliptical lateral profile of

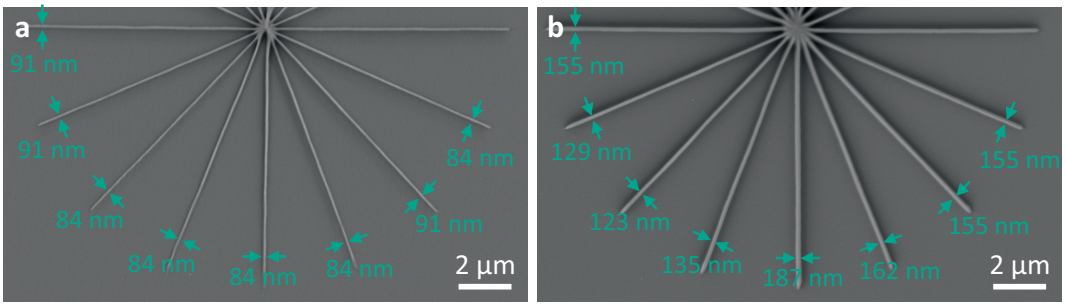

Figure 4.13: **Scanning electron micrographs of two starlike structures printed with (a) and without (b) pinhole.** The structure composes out of 8 simple lines rotated by an angle of 22.5 deg about their center. The absolute thickness of the lines is majorly influenced by the different laser power of 215 µW (**a**) and 270 µW (**b**) used for printing. The linewidths are deduced with the open-source image processing software Fiji. **a** The linewidth is independent on the scanning direction showing the quality of the spatial filtering of the elliptical output beam from the laser diode by the 5 µm-diameter pinhole. **b** A clear angular dependency of the linewidth is observable. The smallest line thickness of 123 nm along the bisectrix of the third quadrant infers the semi-major-axis direction of the elliptical beam. Adapted from [131].

the focus in the print plane. Since the laser diode is freely rotatable when mounting it into the holder, it is not guaranteed that the semi-minor and semi-major axes match the x- and y-axes of the print plane. Therefore, we consider printing a starlike structure as a suitable test. It is a single-layer structure composed of 8 simple lines each rotated by an angle of 22.5° about their center. Figure 4.13 shows scanning electron micrographs of the resulting structures with and without a 5 µm-diameter pinhole.

The absolute thickness of the lines is predominantly defined by the used laser power as discussed with the threshold model in section 2.5. However, it is visible that the widths of the lines vary significantly with the angle when printing without a pinhole, while they remain constant with the 5 µm-diameter pinhole. The corresponding linewidths are derived by the open-source image processing software Fiji by plotting the brightness profiles perpendicular to each printed line. The resulting thicknesses in pixels are then converted using the pixel size of the images as given by the scanning electron micrographs. The measurements with no pinhole in the optical beam path suggest that the direction of the semi-major axis of the elliptical beam roughly matches the bisectrix of the third quadrant (see Figure 4.13).

In conclusion, the spatial filtering using a 5 µm pinhole does influence the printed lines. When removing the pinhole from the beam path, the line thickness varies by about a third from the thickest to the thinnest line. However, in ordinary 3D laser printing, no free-form trajectories with changing print direction are

printed but the print direction remains the same throughout the print. Therefore, printing without a pinhole should work for most of the common applications, albeit spatial filtering will be useful for delicate structures.

4.3.2 *Run-up Printing Strategy*

As mentioned in subsection 4.1.3, the MEMS mirror can scan at very high speeds. However, it is important to employ a so-called *run-up* printing strategy. The run-up is necessary due to the inertia of the mirror. Assuming no run-up, this would result in a higher dose deposited at the starting point of each line since the laser is turned on but the mirror is still at zero velocity just starting to accelerate. This effect is most obvious when printing one layer of nicely seperated single lines without run-up (see panel **a** of Figure 4.14). Here, the direction of printing is alternated starting from right to left in the lowest row. The printed lines exhibit a blob-like structure at the ends where printing started. A run-up distance of 4 µm before turning on the laser is found experimentally to be sufficient when printing at 1 mm s^{-1}. Here, no difference can be seen anymore in the print results. Printing at smaller speeds of course requires smaller run-up distances.

4.3.3 *Setting the Filter Clock Frequency*

Setting the right filter clock frequency on the digital MEMS driver is at least of same importance than the run-up for good printing quality. The filter clock frequency defines the cut-off frequency of the filter used to prevent the mirror from running at too high frequencies. The latter would lead to a damage of the scanner. We find that when setting the filter clock frequency to the suggested default value of 60 kHz a shift of different layers remains even after optimizing the run-up distance. Panel **b** of Figure 4.14 shows top-view scanning electron micrographs of two #3DBenchy structures. The one on the left is the top-view of a well-printed boat. In contrast, the one on the right exhibits four chimneys and drains besides further downsides. The only difference for these two structures is the setting of the filter clock frequency.

A detailed look with a digital oscilloscope unveils its strong influence. If the value is small, a severe temporal delay between input and output signal of the digital MEMS driver is observed. At the default filter clock frequency of 60 kHz, the delay between the first input for a new position and a noticeable change of the output voltage is about 0.6 ms. This results in a considerable shift of 600 nm at a print speed of 1 mm s^{-1}. Going to the maximum value of 3 MHz for the filter clock frequency, the delay gets vanishingly small. However, the voltage channels already show hints of a step-like behavior. This again is undesired for smooth printing

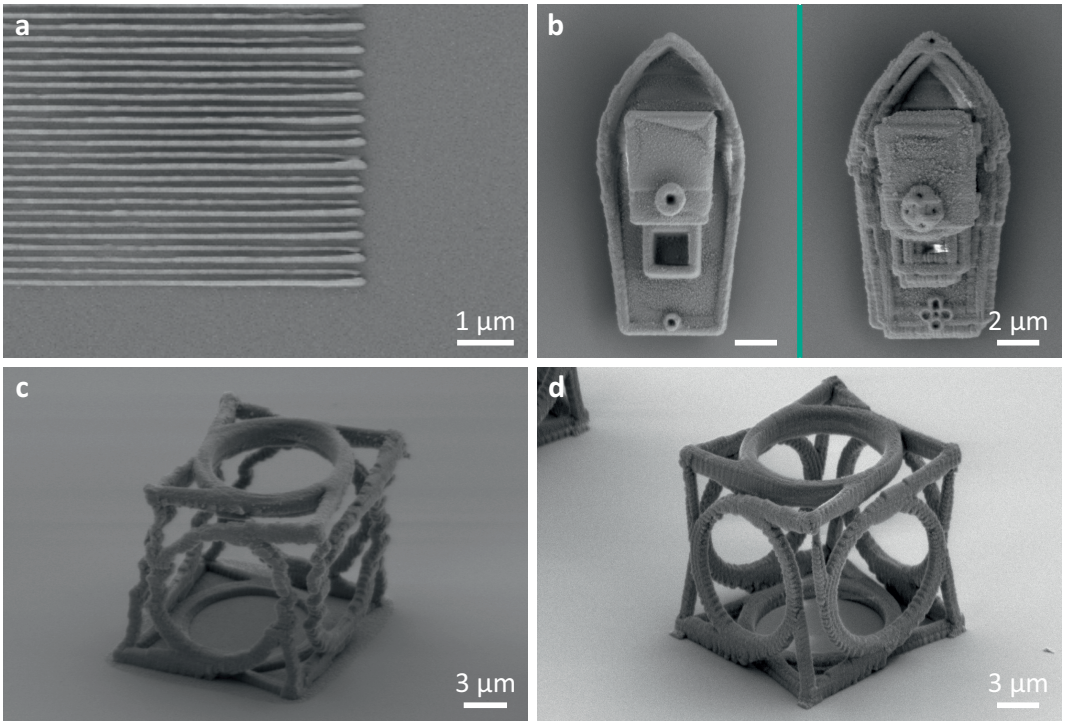

Figure 4.14: **Scanning electron micrographs of different test prints showing the importance of different settings to the print quality. a** A single-layer line grating with 200 nm grating constant shows the influence of a run-up distance. The meandering printing strategy (lowest row from right to left) nicely shows the thickening of the line ends where printing started. **b** Comparison of a well-printed #3DBenchy (left) and one, where the filter clock frequency is set to a too low value (right). Neighboring layers are always rotated by 90° with respect to each other. The small filter clock frequency delays the output of the digital MEMS driver to the MEMS scanner. Therefore, it seems like four #3DBenchy boats are printed in one another. **c** A metamaterial unit cell is printed with an extemporary, thus instable, holder for the objective lens. The curvy structure shows the vibrations during the print originating from a colleague mounting components at a different setup on the same optical table. **d** A metamaterial unit cell printed with a wrong collimation of the laser beam at the entrance pupil of the objective lens prior to final alignment of the 3D laser printer. As a result, the focus gets elongated which is visible from the thickened top of the structure.

with a constant velocity. Additionally, such high frequencies could damage the MEMS scanner especially on the turning point between two print trajectories. An intermediate filter clock frequency of 500 kHz seems to be a good compromise with a delay of around 100 µs. The corresponding oscillograms are shown in Appendix A.

4.3.4 *External Vibrations and Damping*

An intermediate version of the shoe-box-sized 3D laser printer contained an extemporary holder for the small piezo stage. It was 3D printed with a filament 3D printer and not optimized for stability. Print results with this component nicely show the influence of vibrations to the 3D printing quality. Panel **c** of Figure 4.14 shows a metamaterial structure printed in this configuration. A normal lab situation is present during printing: The setup is placed on a standard optical table with passive damping. Coworkers are working simultaneously at a different part of the same optical table mounting components and alike. The resulting curvy structure shows that vibrations obviously heavily influence the quality of printing. However, employing the final holder out of aluminum with a more solid base and a transverse structure solves this issues as the print results in Figure 4.12 under otherwise similar conditions proof. Due to its compact size, the shoe-box-sized 3D laser printer could additionally be mounted on an active vibration isolation system for further vibration reduction if necessary.

4.3.5 *Beam Collimation at the Entrance Pupil*

As discussed in subsection 4.1.4, the collimation of the beam at the entrance pupil of the microscope objective lens influences the quality of the focus. In particular, obtaining a good axial resolution is demanding [36]. Since the shoe-box-sized 3D laser printer does not include a focus measurement routine, the collimation is adjusted with a wavefront sensor. Here, the wavefront is measured and described by the Zernike polynomials. The Zernike mode 5 displays the defocus of the beam. Hence, its value is minimized for optimal collimation. Panel **d** of Figure 4.14 shows a metamaterial structure printed in this configuration. Especially the top circular part of the unit cell shows elongation along the z-direction.

Experimental investigations show that a perfectly collimated beam as optimized with the wavefront sensor does not necessarily lead to the best point spread function as measured in the mentioned highly-engineered laser printing setup. Therfore, we optimize the collimation with the described gold-bead-scanning method employing the other setup and measure the resulting Zernike mode 5 at the entrance pupil of the objective lens. A Zernike mode 5 of 2.1 is obtained. Hence, the scan and tube lens of the shoe-box-sized 3D laser printer are adjusted using the wavefront sensor to result in the acquired Zernike mode 5 of 2.1 as measured at the entrance pupil of the objective lens. This step significantly improves the printing quality.

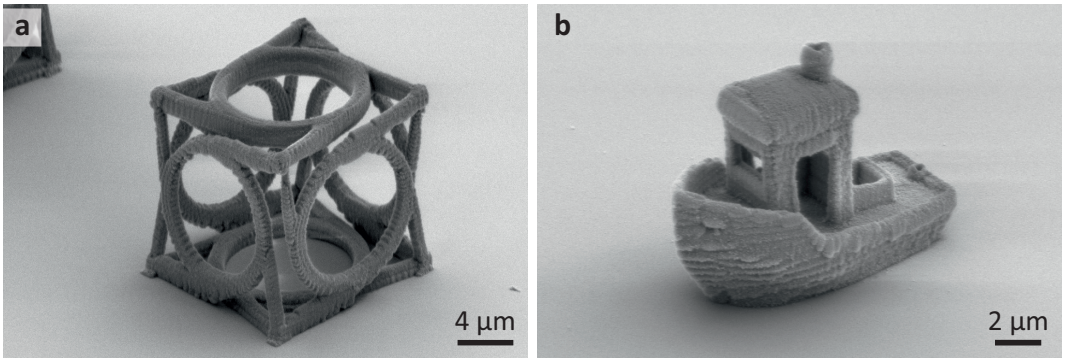

Figure 4.15: **Scanning electron micrographs of a metamaterial unit cell (a) and a #3DBenchy (b) printed with the NA = 1.25 Motic objective lens.** As expected, the axial definition of the print results is slightly worse compared to the results presented in Figure 4.12 as visible with the thickened upper part of the metamaterial structure. Still, the structures are reasonably well defined. Especially, since the dimensions of these two test structures are at the lowest end what is printed in 3D laser printing. Most common structures do not include such fine features, thus being more forgiving for the enlarged voxel. Adapted from [131].

4.3.6 Motic Objective Lens

So far, all presented experiments are performed employing the Leica NA 1.4 objective lens. In subsection 4.1.4, we further present a much less expensive objective lens with a slightly smaller numerical aperture of NA = 1.25. The performance is reviewed by printing the same two 3D test structures at the same print speed. Again, the laser power is optimized for the best print result. Scanning electron micrographs of the resulting metamaterial unit cell and #3DBenchy are shown in Figure 4.15.

As to be expected, the axial definition of the printed structures is worse than with the high-NA Leica objective lens. Hence, the upper part of the metamaterial structure looks similar to the result obtained with the wrong collimation instead. While the low-NA lens might not be suitable for delicate high-resolution 3D structures, it is still perfectly employable for 3D laser printing of larger structures as known for other low-NA objective lenses. We do not see any real disadvantage just because of its low cost.

4.4 Resolution of the Shoe-Box-Sized Printer

Besides the general performance tests, we thoroughly investigate the resolution of the shoe-box-sized 3D laser printer. Common structures for identifying the 2D and 3D resolution in 3D laser printing are line gratings and woodpile photonic

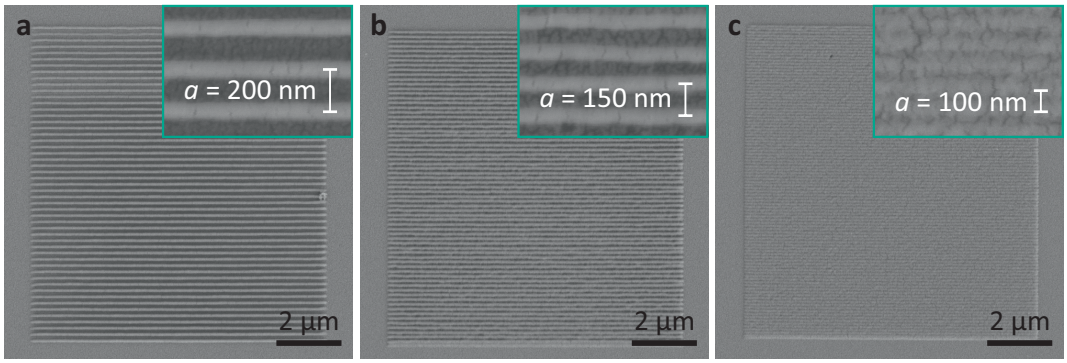

Figure 4.16: **Scanning electron micrographs of 2D line gratings with varying grating constant.** 2D line gratings with a side length of 10 µm are printed with varying grating constant to define the lateral resolution of the shoe-box-sized 3D laser printer according to the Sparrow criterion (see section 2.7). The insets are a zoom-in to better show the single lines with a line width of around 60 nm. The lines are still nicely separated for a grating constant of $a = 200$ nm (**a**) and $a = 150$ nm (**b**). In case of $a = 100$ nm grating constant (**c**), the single lines are not really separated anymore but still distinguishable from each other by a darker line in between. Thus, a local minimum is still preserved meeting the requirements of the Sparrow criterion. Adapted from [131].

crystals, respectively [13, 66]. As mentioned in section 2.7, resolution must not be confused with the minimal achievable line width. Instead, it is about how close two lines can be printed next to each other while they remain distinguishable [13, 168].

For optimal comparability of the shoe-box-sized 3D laser printer with the highly-engineered printer [31], we employ the same conditions. Therefore, the Leica NA 1.4 objective lens is used. Further, the print parameters like size of the structures as well as the print speed of 0.1 mm s^{-1} is chosen accordingly. Additionally, the same resist and evaluation procedure is employed.

Therefore, we analyze the 2D resolution of our compact printer by printing line gratings with 10 µm side length and a varying grating constant. Scanning electron micrographs of the resulting structures are shown in Figure 4.16. They infer achievable line widths of 60 nm and below. At the same time, a lateral resolution below 150 nm can be deduced from the insets of the particular panels. In panel **a** and **b**, the lines are still well separated at a grating constant of $a = 200$ nm and $a = 150$ nm, respectively. Only at a grating constant of $a = 100$ nm, the lines start to merge being not perfectly separated anymore (see panel **c**). Thus, the lateral resolution is found at around 100 nm according to the Sparrow criterion as discussed in section 2.7, or around 150 nm in case the criterion is a perfect separation of the lines.

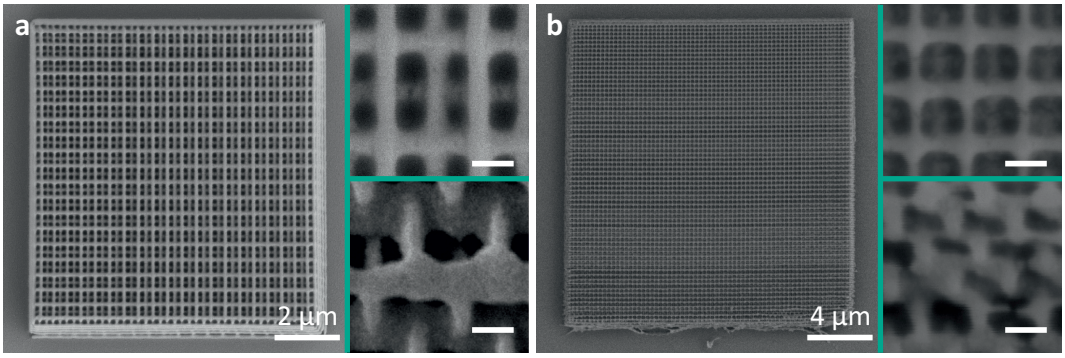

Figure 4.17: **Scanning electron micrographs of printed 3D woodpile photonic crystals with 24 layers. a** A woodpile with a side length of 10 µm and a rod spacing or grating constant of 500 nm. **b** A woodpile with a side length of 20 µm and a rod spacing or grating constant of 300 nm. The zoom-ins on the upper right, respectively, nicely show the separation of the lines. In addition, the half-pitch shift of subjacent next-nearest layers is observable. The zoom-ins on the lower right, respectively, show the side of the structure under an angle of 60°. Here, the good separation of the lines in axial direction is visible. Further, the lateral and axial voxel size can be derived from the images to best values of 80 nm and 275 nm, respectively. The scale bars in the zoom-ins correspond to a distance of 200 nm. Adapted from [131].

These results are in good agreement with our results obtained employing the same objective lens in the highly-engineered but bulkier setup [31]. At the same time it surpasses previously best results of 175 nm achieved by STED-inspired two-photon 3D laser printing at a fundamental wavelength of around 800 nm [13] and matches other best results of 110 nm obtained by two-photon absorption using the same fundamental wavelength of 405 nm as used here [12]. It even perfectly fits to the theroretically calculated value in section 2.7 of 102 nm.

The axial resolution is determined by printing 3D woodpile photonic crystals. Woodpile photonic crystals are a stack of line gratings. Here, neighboring layers are rotated by 90° while next-nearest neighbors are additionally shifted by half the grating constant of the underlaying line grating [169]. Scanning electron micrographs of a woodpile structure with 24 layers, a side length of 10 µm, and a rod spacing or grating constant of 500 nm is shown in panel **a** of Figure 4.17. A second woodpile structure with 24 layers, a side length of 20 µm, and a rod spacing or grating constant of 300 nm is shown in panel **b** of Figure 4.17. The zoom-ins on the respective upper right nicely show the well separated lines even revealing the half-pitch shift of subjacent next-nearest layers.

The oblique-view scanning electron micrographs on the respective bottom right show the separation of the lines in z-direction. Further, it allows to deduce the lateral and axial voxel size. Values of 80 nm and 275 nm are achieved, respectively, taking the best results achieved in panel **b**. Once more, the resulting numbers

match the previous results with the highly-engineered yet bulkier setup. In addition, the resulting spatial resolution matches again to the results obtained by STED-inspired two-photon 3D laser printing at a fundamental wavelength of around 800 nm [13] and the ones by two-photon absorption using the same fundamental wavelength of 405 nm [12].

4.5 Discussion and Outlook

In summary, the goal to confine a fully functional, low-cost, high-resolution 3D laser printer in the size of a shoe box is achieved. Two-step absorption as an alternative excitation mechanism fundamentally enables the drastic size-reduction of the optical setup and is deployed in our printer. Further, a miniaturized and powerful but low-power control unit is designed and successfully implemented. This opens the path for a final compact and stand-alone device.

Additionally, a drastic reduction of the cost is obtained. Here, only crucial elements are employed. Alignment tools like accessory mirrors or adjustable holders are evaded where possible coming along with a challenging alignment. At the same time, less expensive alternatives like plastic lenses and a home-made coarse translation stage are implemented where possible. Extra components for improved beam quality like lens groups instead of single lenses for the scan and tube lens are avoided at first and performance in this minimized configuration is investigated.

The performance is approved by two demanding three-dimensional structures. Further, the resolution of the system is analyzed. A lateral and axial resolution of below 150 nm and 400 nm is achieved, respectively, matching previously obtained results. Therefore, the beam quality seems adequate and no further components for beam optimization are necessary.

An inexpensive microscope objective lens with a slightly smaller numerical aperture is tested. As expected, it results in an elongated voxel for printing otherwise showing good performance. Taking this lens, the total costs of the compact 3D laser printer are estimated to about five thousand Euros.

Obvious next steps for the shoe-box-sized 3D laser printer are the final microcontroller implementation of the piezo stage for the movement in z-direction. In addition, the device can be battery-powered and data transfer can be changed to SD card for further autonomization. The implementation of a focus measurement routine is not crucial but would certainly improve the convenience of the alignment procedure when setting up the device. In addition, a 3D laser printed objective lens could be customized for the setup and further reduce the cost following the ongoing research on 3D laser printing compact multi-lens systems [170–174].

Up to now, two-step absorption is still stunted in increasing usage due to the limited speed and its accumulation problems connected to the non-inert intermedi-

ate state of current photoinitiators as discussed in section 3.5. Thus, more research on photoinitiators, quenchers, and scavengers is highly desired. Furthermore, the influence of oxygen to the two-step mechanism could be investigated by using the compact printer in a flow-box under nitrogen atmosphere. So far, experiments on oxygen influence always suffered from unknown remaining oxygen during the experiments under atmospheric conditions. Therefore, our shoe-box-sized low-cost 3D laser printer could help pushing the very recent field of two-step absorption and in general democratizing 3D laser printing in our view.

Part II

NOVEL MATERIAL

Chapter 5

5 Merging Additive and Subtractive Manufacturing

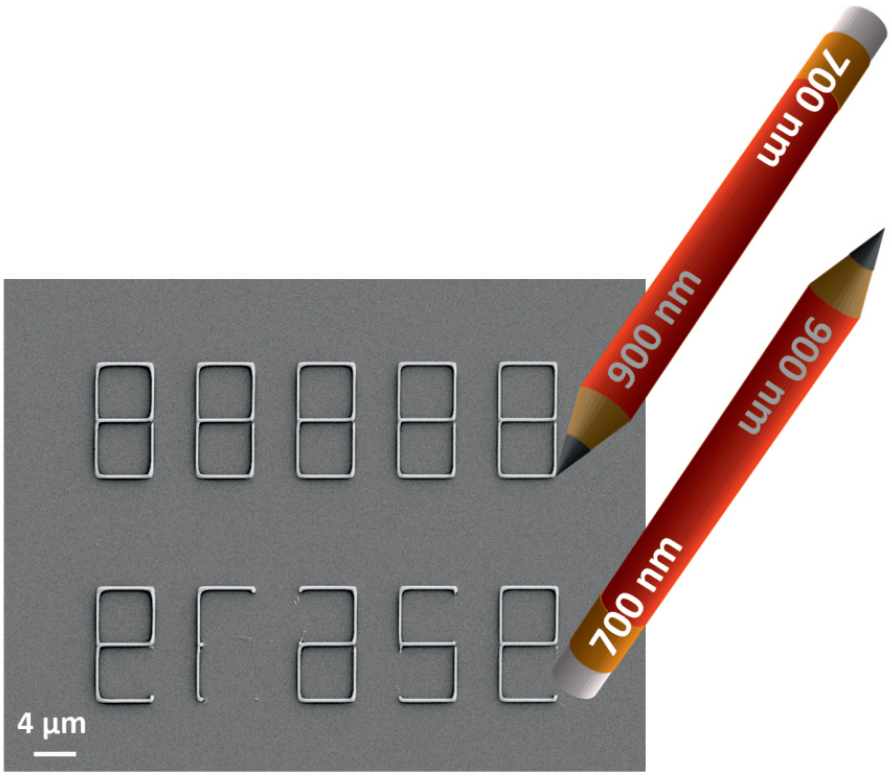

Artistic illustration of merging writing and erasing in a single tool.

Two-photon absorption employed in 3D laser printing is a powerful tool for additive manufacturing on the micro- and nanoscale. In this chapter, I will present our work on implementing two-photon absorption for subtractive manufacturing. Even further, our novel material acts as a single tool for additive and subtractive 3D laser manufacturing at the same time.

5.1 Introduction

A lot of simple pencils have a rubber on their end. What does not look special at a first view is very advantageous at the second: it enables both writing and erasing merged in a single tool. In terms of manufacturing, writing and erasing translates to additive and subtractive manufacturing, respectively. Nowadays, there are lots of tools for additive and subtractive manufacturing for different dimensions and materials [175–177]. Light is one of them, being employed in various devices. However, light is a tool that typically only allows for either addition or subtraction in a specific application.

One of these applications is 3D laser printing [7, 178, 179]. So far, the high spatial confinement of two-photon absorption has been exploited for the creation of structures in various fields [4]. Though, there is an ongoing demand to partially or fully erase features of the printed structures on demand [94]. New material systems have been developed employing high-resolution printing via two-photon absorption which can be erased on demand under specific conditions through network cleavage [180, 181]. However, the reported material systems rely on a chemical selectivity and do not allow for spatial confinement of the cleaving.

On the other hand, highly focused light has been exploited for subtractive manufacturing in multiphoton ablation processes [17, 182, 183]. Here, a high-power laser is focused onto the sample similar to 3D laser printing. However, there is no chemical reaction triggered. Instead the material heats up and vaporizes [184] resulting in a chemically undefined process [180]. This leads to rather rough and irregular structures on the microscale (see Figure 5.5). Thus, we introduce a new monomer system enabling both high-resolution additive and spatially selective subtractive manufacturing exploiting two-photon absorption.

5.1.1 The o-Nitrobenzyl System

Similar to most monomers used in 3D laser printing (see section 2.3), our newly designed monomer contains acrylate groups for crosslinking, i.e. the additive part. As a photocleavable linker, thus the subtractive part, the well-known photolabile *o*-nitrobenzyl ether (ONB) motif is chosen. The latter is able to cleave under UV irradiation. It undergoes a Norrish Type II reaction resulting in a photoisomerization. Therefore, the ONB motif is frequently used in polymer science [185–192]. However, it has not been used in a photoresist system before.

The monomer was synthesized in a three-step procedure by Rhiannon Batchelor. The chemical structural formula of the final *o*-nitrobenzyl (ONB) containing diacrylate and its residues after cleavage are shown in Figure 5.1 together with its absorption spectrum.

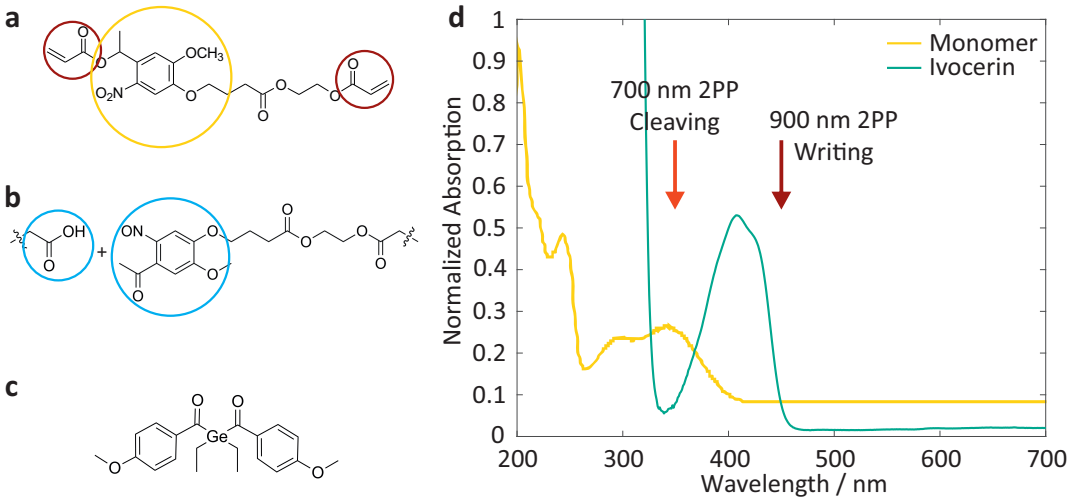

Figure 5.1: **Structural formulas and absorption spectra of the employed molecules.** **a** The synthesized monomer containing two acrylate groups as reactive units (red circles) and the well known ONB motif for cleaving (yellow circle). **b** The residues after cleavage with the opened part of the molecule encircled in blue. **c** The used photoinitiator Ivocerin. **d** Normalized one-photon absorption spectra of the monomer (yellow curve) and Ivocerin (green curve). The red-shifted absorption of Ivocerin enables 3D laser printing without triggering the cleavage reaction at the same time. The two arrows indicate the corresponding two-photon wavelength employed for writing (900 nm) and cleaving (700 nm). Adapted from Ref. [193].

5.2 Writing – The Additive Part

Having acrylate groups incorporated for crosslinking, the monomer is suitable for both two-photon and two-step 3D laser printing in principle. However, the 405 nm irradiation would already trigger the bond cleavage of the ONB motif, as it takes place after one-photon absorption at around 300 – 400 nm typically [192]. Therefore, a two-photon photoinitiator is needed with a one-photon absorption exceeding 400 nm – corresponding to a two-photon absorption above 800 nm – to prevent photocleavage during the writing process. The germane-based radical initiator Ivocerin is selected as it has been used as a visible light initiator at 408 nm wavelength for dental applications [194]. The absorption spectrum of Ivocerin is also shown in Figure 5.1.

Usually, the amount of photoinitiator is pushed close to saturation in the liquid monomer for most efficient 3D laser printing. Here, the diacrylate ONB monomer is solid. Thus an additional solvent is used for a final liquid photoresist. Different solvents are tested and dimethylformamide (DMF) is found to be most suitable. It combines a high boiling point of 153 °C with a good solubility for both solid components. As discussed in subsection 2.3.3, a minimal amount of solvent with a high boiling point is desired because of otherwise increased chances for

micro-explosions. Our final resist comprises 30 mg monomer and 1.5 mg Ivocerin dissolved in 30 µL DMF.

For printing, a home-built two-photon 3D laser printer is employed. It was originally built by Joachim Fischer and used in various work of our group with detailed descriptions in Ref. [14, 15, 97, 195, 196]. The setup follows the structure of a common 3D laser printing setup as explained in section 2.1.

It is based on a femtosecond-pulsed Ti:Sapphire oscillator (Chameleon Ultra II, Coherent). The main advantage of Ti:Sapphire oscillators is their potential to tune the wavelength from 680 nm to 1080 nm. The tuneable wavelength is crucial for our work as a separate wavelength for writing and erasing is elementary. The power modulation is performed by an acousto-optic modulator (MTS40-A3-750.850, AA Opto Electronic). The beam is expanded to match the width of the back aperture of the objective lens (HCX PL APO $100\times/1.4-0.7$ OIL CS, Leica).

Scanning in x- and y-direction is realized by a 2D piezo stage (P-734.2CD, Physik Instrumente) with a scan range of $100\times100\,\mu m^2$. The stage is mounted on a motorized stage (P-M-686, Physik Instrumente) for coarse movement. For scanning in z-direction, the objective lens is mounted onto a vertical linear piezo stage (P-733.ZCL, Physik Instrumente) with a range of 100 µm. Additional components for power measurement, focus measurement, interface search, and monitoring are employed.

In a first step, the adequate wavelength for 3D laser printing needs to be determined. It should efficiently excite the photoinitiator to trigger the radical polymerization reaction without degrading the photolabile ONB group. Thus, simple line structures are printed at different wavelengths of the laser. Since Ivocerin has not been used for two-photon 3D laser printing before, these preliminary experiments employ the well established PETA as a monomer instead of our resist containing ONB diacrylate. The wavelength is swept from 800 nm (to be above the corresponding 400 nm where one-photon degradation would start) to 900 nm where the optical output power of the laser drops and some of the optics in the beam path should be replaced by those with different coatings. All structures are developed for 5 min in dimethyl sulfoxide (DMSO), acetone, and water consecutively.

The best results with the PETA resist are obtained at a center wavelength of 900 nm and a print speed of $0.1\,mm\,s^{-1}$. Therefore, the same line patterns are printed at a wavelength of 900 nm using our ONB-containing resist. The threshold for printing is around $6-7$ mW under these conditions and best results are achieved at 8 mW. Further, optimum writing conditions are found by preheating the sample on a hotplate at 40 °C for 10 min prior to printing. A second cover slip is placed on top of the substrate with a spacer to prevent evaporation of DMF throughout printing, thereby preserving the composition of the resist. These writing parameters are employed for all printing experiments.

To further verify the printing capability of the resist, simple 3D structures are

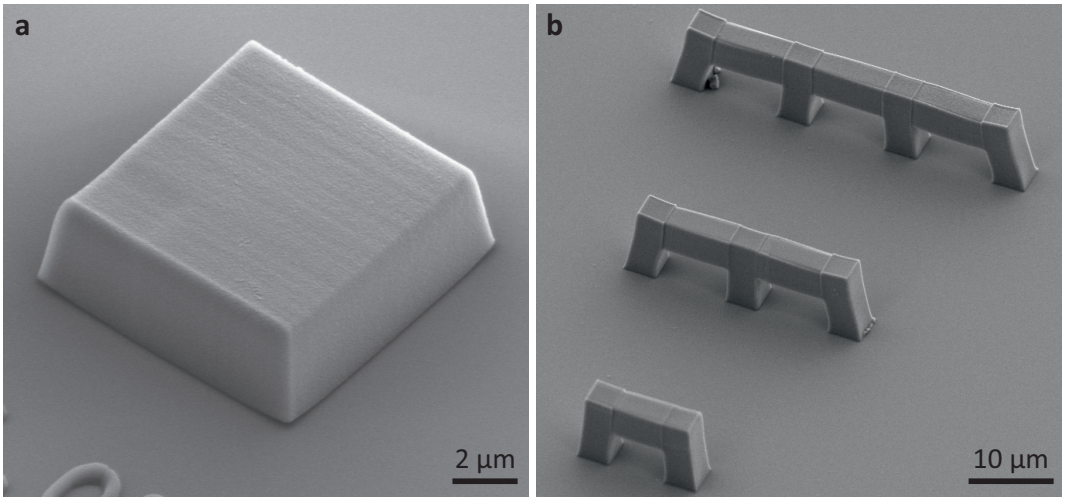

Figure 5.2: **Scanning electron micrographs of 3D printed samples with the ONB-containing resist.** **a** A simple block with a dimension of $15 \times 15 \times 5\,\mu m^3$. These cuboids are later used for 3D laser cleaving. **b** Three bridges with varying amount of bridge segments. All bridges have a height of 8 µm and one of the segments has a length of 15 µm. The bridges show that overhanging structures are feasible with our resist system. Hatching and slicing for all 3D structures are set to 200 nm and 300 nm, respectively.

printed. Scanning electron micrographs of a simple block and plain bridges are shown in Figure 5.2. The cuboids have a side length of 15 µm and a height of 5 µm. A hatching and slicing distance of 200 nm and 300 nm is employed, respectively. The bridges have a height of 8 µm and a length of 15 µm per segment using the same hatching and slicing. The results show good 3D laser printability of the ONB-containing resist at 900 nm wavelength.

5.3 Erasing – The Subtractive Part

Aside from printability, also the photodegradation of our monomer has to be shown. Thus, different experiments are conducted specifically to prove the mechanism to be photoinduced rather than thermally activated. The cleaving experiments comprise one-photon irradiation of both the pure resist and 3D laser printed microstructures as well as the desired two-photon induced cleaving.

5.3.1 One-Photon Cleaving

First, experiments on the non-crosslinked monomer are performed. Here, 7 mg ONB monomer is dissolved in 600 µL of deuterated chloroform ($CDCl_3$). In a

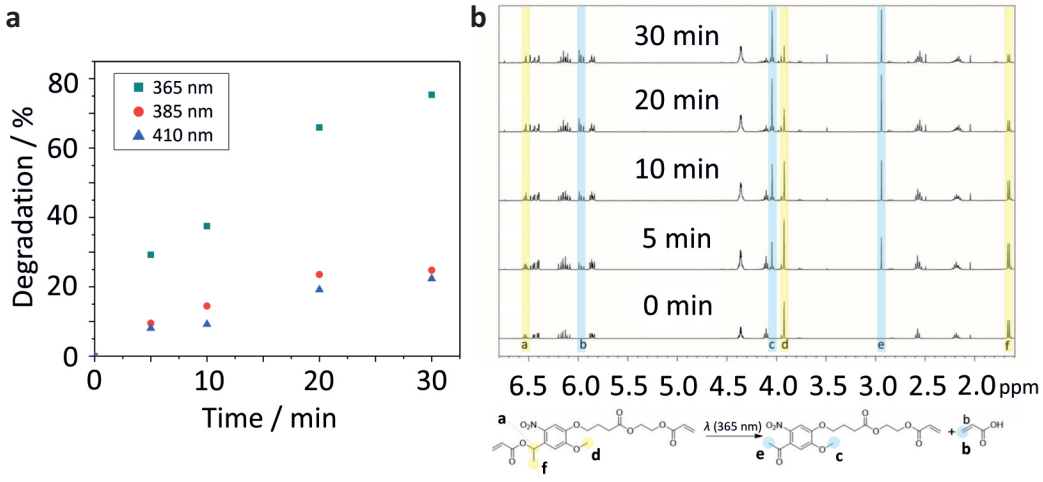

Figure 5.3: **^{1}H NMR spectrum analysis on one-photon degradation tests employing unpolymerized ONB monomer.** **a** Wavelength dependence of the degradation process. Highest degradation is yielded under illumination with a 365 nm LED. A red-shifted illumination drastically reduces the conversion of ONB monomer. **b** Exemplary temporal evolution of the measured ^{1}H NMR spectrum. Here, the sample is exposed with 365 nm wavelength light. Yellow areas mark characteristic resonances for the ONB monomer, blue areas for the residues. The decreasing signals especially for the α-proton and methyl protons resonances at 6.55 ppm and 1.68 ppm, respectively, are clearly visible. Together with the emerging methyl ketone resonance at 2.94 ppm this proofs the conversion of the ONB-containing monomer. Adapted from Ref. [193].

photoreactor, the solution is placed in a nuclear magnetic resonance (NMR) tube at a 5 cm distance of an LED. Different LEDs are employed to investigate the influence of the wavelength on the cleaving process. Three different wavelengths are tested: 365 nm (Nichia NVSU233B SMD-LED UV) with an intensity of 10.2 mW cm^{-2}, 385 nm (Avonec high powered LEDS) with an intensity of 5.02 mW cm^{-2}, and 410 nm (Avonec high powered LEDS) with an intensity of 10.1 mW cm^{-2}.

The samples are irradiated for specific time intervals and analyzed each by measuring the ^{1}H NMR spectrum. Panel **a** of Figure 5.3 shows the wavelength dependence of the light-induced degradation. The values of photocleavage are calculated from the ^{1}H NMR spectrum. The most rapid progress is found under irradiation at 365 nm, where 75 % of the monomer has undergone cleavage after 30 min. A red-shifted illumination causes a drastic decrease in conversion to only 25 % or 22 % after 30 min under illumination at 385 nm and 410 nm, respectively. Thus, shorter wavelengths are preferable for cleaving.

Panel **b** of Figure 5.3 shows one of the ^{1}H NMR time series under illumination at 365 nm. Characteristic resonances for monitoring are the disappearing α-proton

and methyl protons resonances at 6.55 ppm and 1.68 ppm, respectively, and the emerging methyl ketone resonance at 2.94 ppm.

Further, the influence of crosslinking to the photodegradation is investigated. Therefore, simple single-layer text structures are 3D laser printed at 900 nm wavelength employing our ONB-resist as well as a control resist containing PETA as the monomer and Ivocerin as the photoinitiator. Panel **a** of Figure 5.4 shows scanning electron micrographs of the resulting text structures after development.

The microstructures are immersed in liquid by placing a droplet of DMSO on top of the substrate and irradiated with light at 365 nm wavelength for four hours. The reasons for applying a solvent on top of the structures is two-fold: first, it helps dissipating the generated heat, and second, it dissolves the cleaved chemical fragments. Routinely, the sample is washed and inspected by scanning electron microscopy. The resulting structures are shown in panels **b** and **c** of Figure 5.4. While nothing changes for the control structure, first the thinning and later disappearance of the text structure written with the ONB resist is clear evidence of the photodegradation.

5.3.2 *Two-Photon Cleaving*

Finally, the two-photon induced photodegradation of the resist has to be verified. The receptiveness of the ONB motif for two-photon absorption enabling precise spatial degradation has been shown within hydrogels [197–199] but has not been investigated in dense polymer networks. Therefore, we start our two-photon cleaving experiments with simple 2D line structures printed at 900 nm wavelength. The distance between two neighboring lines is chosen to be 5 µm.

Subsequently, the laser is tuned to 700 nm wavelength and the same line pattern is traced perpendicular to the written lines at a focus speed of 20 µm s^{-1} and a power of 10 mW. The same experiment is conducted with the PETA control resist. Scanning electron micrographs of the results are shown in panel **a** of Figure 5.5. Noticeably, the surface of the cleaved segments is extremely smooth for the ONB-containing resist, while for the control structure irreproducible and rough surfaces result. We attribute the latter to ablation being the driving mechanism when irradiating the PETA structures.

Furthermore, we exploit the 3D capability of the two-photon cleaving. We start with printing 3D cuboids with a dimension of $15 \times 15 \times 5\,\mu m^3$ at 900 nm wavelength. After development and re-immersion in DMSO, different fine features are removed from these structures in a second two-photon lithography step at 700 nm wavelength. However, while erasing in the 2D experiments is readily possible at low focus speeds and high power, it is not as straightforward for 3D structures. A good cleaving strategy is crucial to not introduce too much heat to

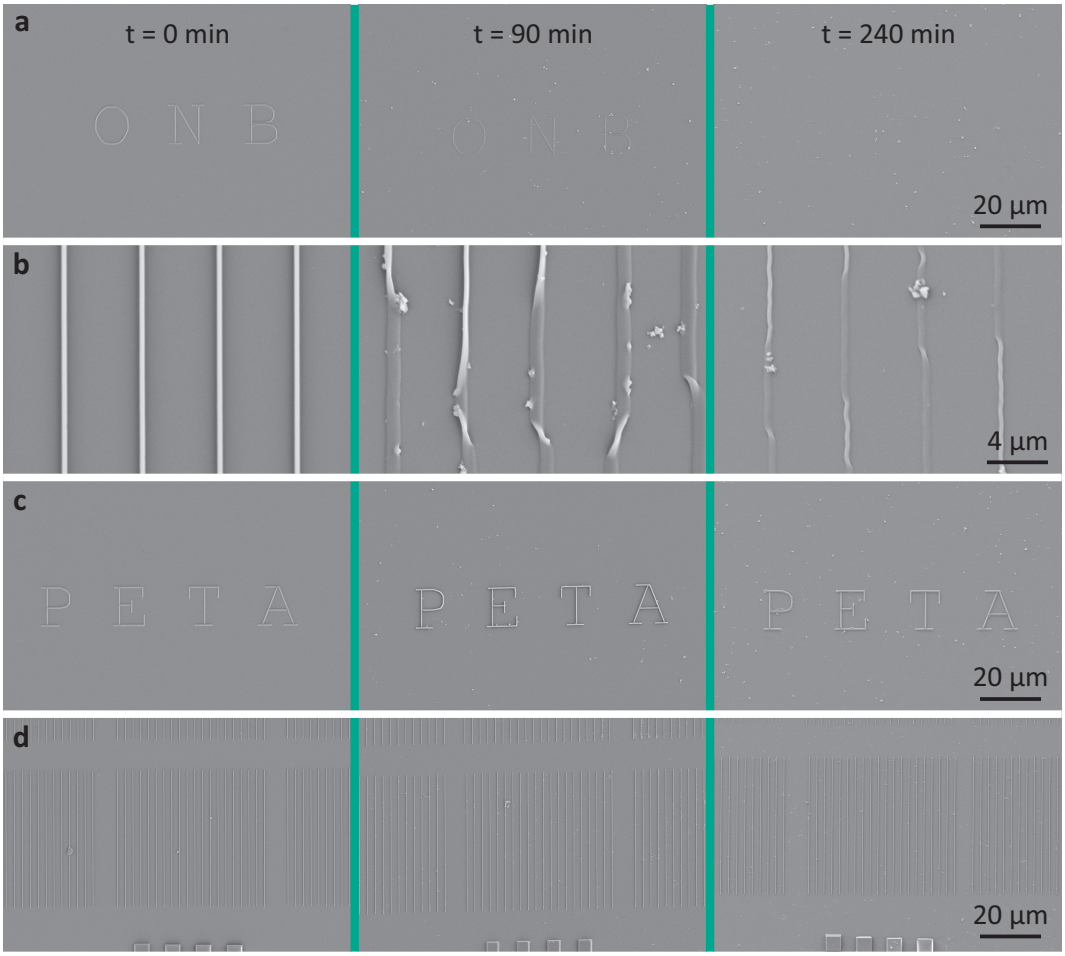

Figure 5.4: **Scanning electron micrographs of 2D line and text structures irradiated with 365 nm light for cleaving. a** 'ONB' written as text and **b** lines with a grating constant of 5 µm both printed with the ONB-containing monomer. **c** 'PETA' written as text and **d** lines with a grating constant of 5 µm both printed with PETA as a control experiment. Both samples are irradiated under the same conditions. The left row shows the initial structures before exposure. The center and right row show the structures after 90 min and 240 min, respectively. For the structures written with our monomer, a clear degradation over time is visible due to the thinning of the structures. The control with PETA does not show degradation under the same conditions. Adapted from Ref. [193].

the system causing explosions, and at the same time to allow for good carting off of the residues.

Therefore, different procedures are tested. The most effective strategy is found to be repeatedly scanning of the structure to be cleaved in a layer-by-layer mode starting at the outside wall of the printed cuboid. First, simple cylinders are removed starting from the top surface (see top row of panel **b** in Figure 5.5). Again,

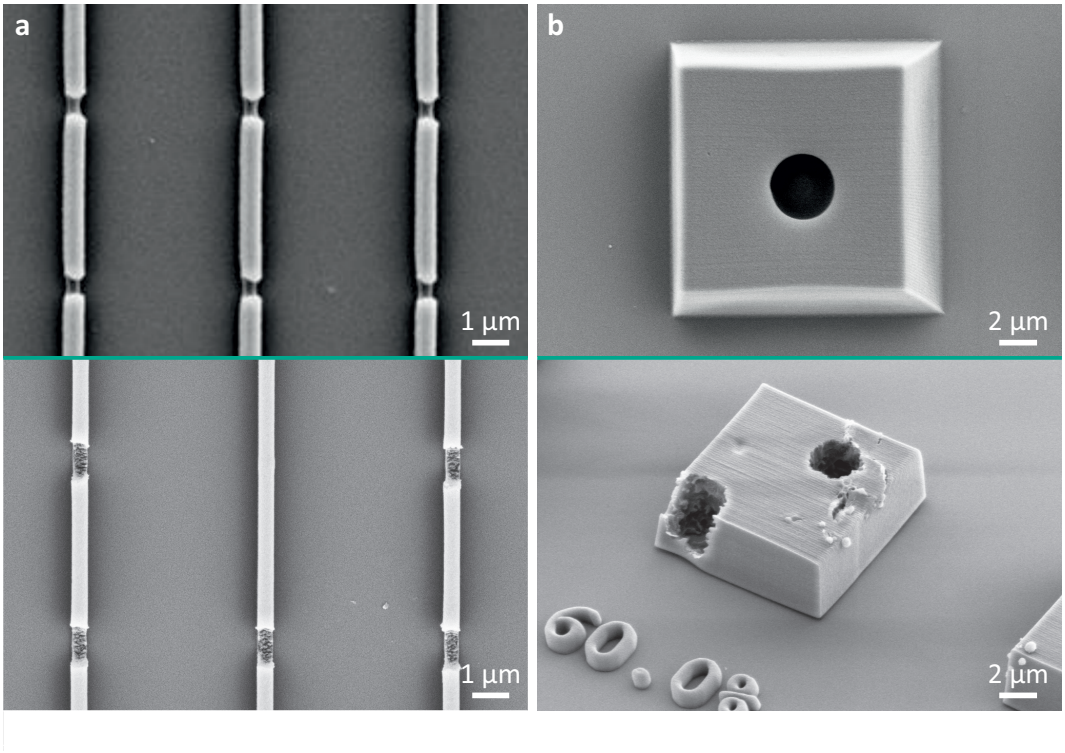

Figure 5.5: **Scanning electron micrographs of two-photon induced cleaving experiments on structures written with the ONB-containing resist (top row) and a PETA-based resist (bottom row) for comparison. Simple line structures (a) with a line grating of 5 µm and blocks (b) are written with both resists at 900 nm wavelength. a** The same line pattern is scanned rotated by 90° with the laser tuned to 700 nm wavelength for erasing. While the cleaving is steady and smooth for the lines written with our monomer, it is arbitrary and coarse for the PETA resist. **b** Small cylinders are scanned at 700 nm wavelength into the pre-written cuboids. Again, for the ONB-containing structure in the top row a smooth surface results, while the cleaving experiment on the PETA-written cuboid yields to severe debris. The results nicely show the difference between photodegradation in case of our resist in comparison to heat induced ablation in case of the PETA resist. Adapted from Ref. [193].

the same structure is scanned into a pre-written PETA cuboid for comparison (see bottom row). Note that slightly higher power is needed in case of the PETA resist for something to happen under otherwise identical conditions ($14 - 20$ mW), yet immediately coming along with micro-explosions indicating a different reaction. This translates again into rough surfaces and substantial debris in huge contrast to the smooth surfaces gained by employing the ONB-containing resist.

To sound out the opportunities of our resist, more demanding structures are tested. Here, delicate structures like channels with a diameter of only 1 µm in

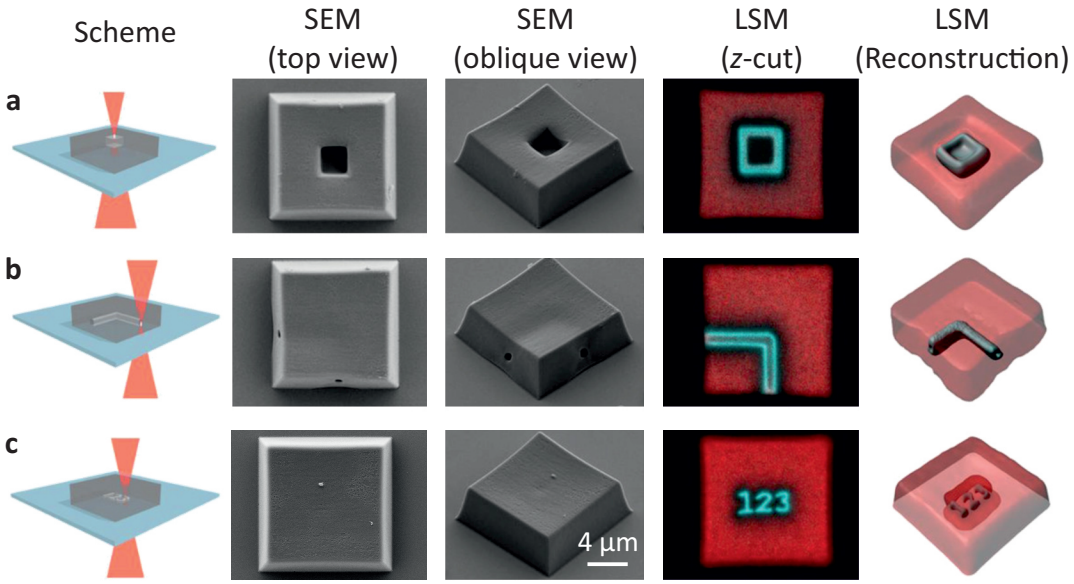

Figure 5.6: **Collection of different structures cleaved inside cuboids.** The cuboids were written at 900 nm with a dimension of $15 \times 15 \times 5\,\mu m^3$. Subsequently, a small block with $3 \times 3 \times 3\,\mu m^3$ (**a**), a 90° channel (**b**), and the numbers '123' (**c**) are cleaved inside at a wavelength of 700 nm. Adapted from Ref. [193].

various configurations are erased from the cuboids. Further, text and numbers are 'written' inside the structures. A collection of different structures two-photon cleaved inside two-photon printed cuboids is shown in Figure 5.6. The top- and oblique-view scanning electron micrographs prove that the outer structure remains intact with the exit holes of the channels clearly visible.

In addition, the fluorescent property of the residual nitrosobenzyl derivatives is exploited in a laser scanning microscope (Zeiss LSM 800) to visualize the surface of the cleaved parts. Here, we employ illumination at 561 nm, and a detection channel at $400 - 599$ nm. To resolve the non-cleaved structure in the laser scanning microscope, a fluorescent dye (Atto 647N, Merck) emitting in the red region is mixed into the resist prior to printing following the concept of Frederik Mayer et al. [200].

Both the laser scanning microscope z-cut as well as the 3D reconstruction enable an inside-view of the structure. The fluorescence of the residue depicted in blue nicely shows the surface of the smooth 90° channel in panel **b**. The strongly reduced blue intensity in the center of the channel proves the channel to be fully open. In addition, sub-micrometer features such as numbers are erased entirely inside the block showing a fully intact block in the corresponding scanning electron micrograph. Only the fluorescence measurement allows us to image the erased

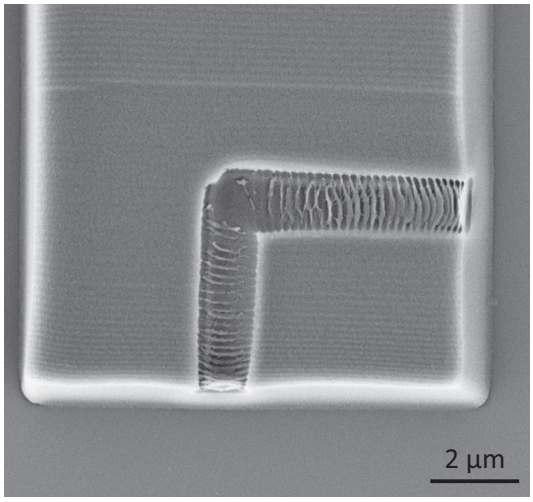

Figure 5.7: **Scanning electron micrograph of a cleaved cuboid cut open with two-photon cleaving.** The cuboid is printed and the 90° channel cleaved as usually. In addition, the laser at 700 nm wavelength is employed to cut the structure open. Here, the z-position of the focus is chosen to hit the center of the cuboid and a simple 2D plane is scanned across the structure. The result shows the fully open 90° channel.

parts.

Another option to look inside one of the blocks is to employ the two-photon cleaving itself for cutting the block open. A scanning electron micrograph of one of the attempts is shown in Figure 5.7. In addition to the laser scanning microscope cut, it proves the channel to be open. However, a lamella-like structure remains inside. The reason is a reduced slicing distance of 200 nm during cleaving in this specific experiment which is specially conducted to find the optimum slicing distance. With that result, all other experiments use a slicing distance of 100 nm. Still, cutting the structure open with two-photon cleaving is rather inconvenient because gravity forces pull the upper part downwards and commonly both parts remain stuck together.

5.4 A Multimaterial System

Besides two-photon cleaving arbitrary 3D structures inside of pre-printed structures, another advantage lies in the utilization in a multimaterial system. Here, we print an array of small patches with a dimension of $5 \times 5\,\mu m^2$ employing our ONB-containing resist at 900 nm wavelength in our home-built setup. These serve as sacrificial support structures. After development, a commercial acrylic photoresist (IP-L 780, Nanoscribe GmbH) is drop-casted. In a second 3D laser printing step, wire bonds are anchored to the pedestals using a commercial 3D laser printer (Photonic Professional GT, Nanoscribe GmbH) at 780 nm wavelength. Covalent binding between remaining acrylate groups within both structures is achieved, since the conversion of photocrosslinkable groups during printing is never 100 %.

After subsequent development, the structures are prepared for cleaving as

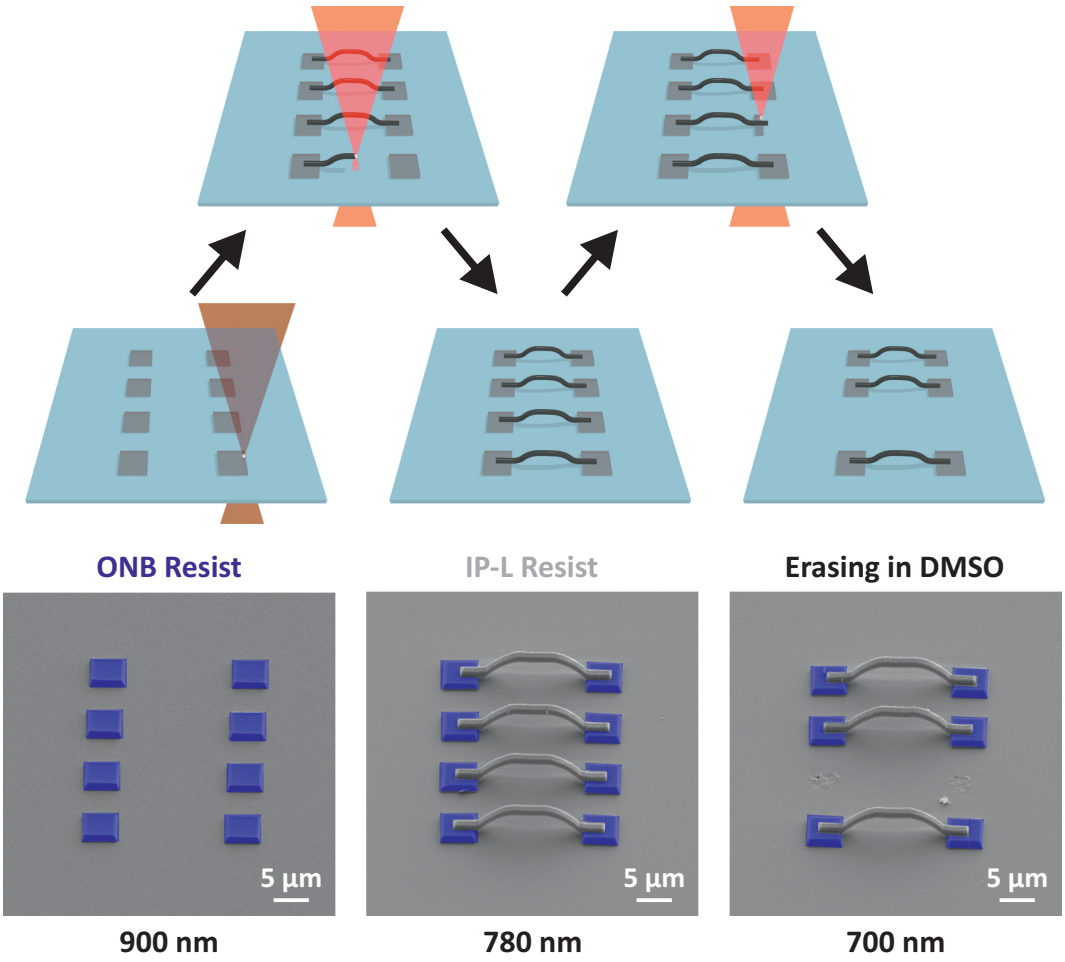

Figure 5.8: **Scheme of the multimaterial capability of the ONB-containing resist in a wire bond manufacturing example.** The upper part shows the principle of printing sacrificial structures with the cleavable resist, subsequent manufacturing of other structures with a commercial resist and a commercial 3D laser printer, and finally spatially controlled removal of parts of the structure. The lower part shows colored scanning electron micrographs as a proof for realization of the concept. Adapted from Ref. [193].

discussed in previous sections. In a next step, a specific wire bond is removed from the substrate in the home-built setup. Here, the femtosecond laser is tuned to 700 nm wavelength and scanned across the sacrificial patch leading to cleavage. In case both supporting patches are removed, the wire bond no longer attaches to the substrate and gets washed away with the solvent. New patches and a new wire bond could now be added. The full principle is depicted in Figure 5.8 together with scanning electron micrographs of intermediate steps in the real experiment.

5.5 Discussion and Outlook

Just as the simple pencil with a rubber end, introduced at the beginning of this chapter, is a single tool for writing and erasing at the same time, a single tool which allows for both 3D additive and subtractive manufacturing at high-resolution triggered by light is realized. A novel monomer containing acrylate groups and the known photolabile ONB motif is developed for the first time acting as a positive tone photoresist at one wavelength and as a negative tone photoresist at a second wavelength. Both manufacturing steps are spatially confined on a sub-micron scale via two-photon absorption processes.

To demonstrate the selective cleaving, well-defined delicate structures are erased from previously written microstructures out of the presented resist. Microchannels with 90° turns are fabricated being challenging for other manufacturing techniques. Going beyond, even more demanding structures for common subtractive manufacturing processes like curved or zigzag channels are easily possible with the developed system.

In addition, the capabilities of our ONB-containing resist system is proven in the context of multimaterial systems. Due to the good compatibility with common acrylate-based resists, it can be used as a cleavable support structure or sacrificial layer. Experiments demonstrate the concept of selectively erasing individual structures on demand, while other structures are preserved. In our view this opens up so far unattainable possibilities, where damaged devices could potentially be fixed instead of thrown away.

We need to emphasize that an access path is crucial to completely remove the residues of the cleaving process. Furthermore, shrinkage occurs in proximity to the erased structures. We attribute this to the fact that similar to the known dose accumulation for 3D laser printing also 3D laser cleaving is triggered in the tails of the laser focus to some extend. Having a close look at one of the tunnel exits in the scanning electron micrographs, a cone shape can be observed as the superposition of the single cone scanned in a circular shape.

Further searches for different monomers exploiting the same characteristics could include different resulting physical properties such as stiffness or flexibility. Finally, a perfect system would allow for a full reversibility of the writing and cleaving process. Such a resist would certainly boost the field of applications of 3D laser printing and 3D laser cleaving.

Part III

SPECIAL APPLICATIONS

Chapter 6

6 405 nm 3D Laser Printing of High-Resolution Kinoform Lenses

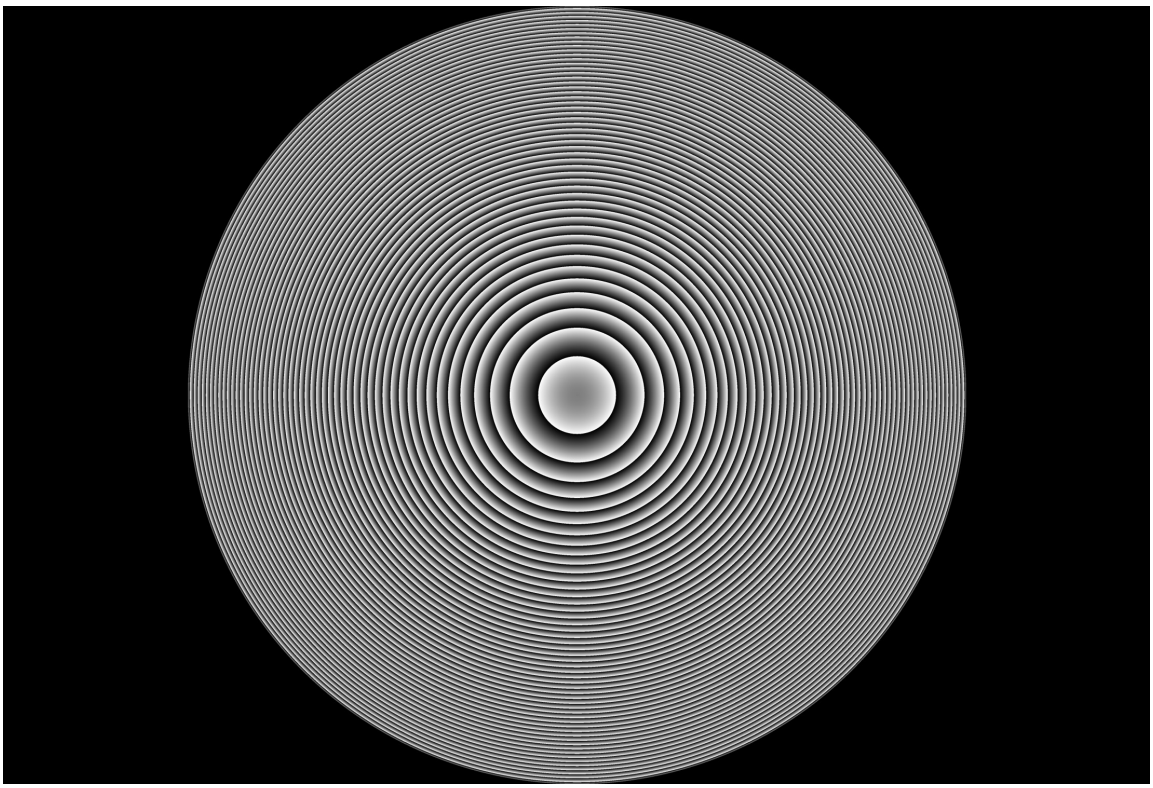

Grayscale image of the 3D laser printed kinoform.

In this chapter, I will demonstrate the capabilities of printing at 405 nm wavelength in terms of resolution. As an example, the printing of high-resolution kinoform lenses is discussed.

6.1 Motivation

The wavelength influence on the resolution of an optical system was outlined in section 2.7. According to the Sparrow criterion (see Equation 2.3), which is usually used as the resolution criterion in 3D laser printing, the lateral resolution scales linearly with the wavelength and inversely with the numerical aperture of the used lens. Thus, a fundamental improvement in lateral resolution can be achieved either by reducing the employed wavelength or by increasing the numerical aperture. This explains the drive in one-photon-based UV lithography to exploit ever shorter wavelengths [84] to fulfill the famous law of Gordon Moore [201]. Nowadays, even extreme ultraviolet lithography is used in semiconductor device fabrication at wavelengths near 13.5 nm [202], targeting $3-5$ nm nodes. The main drawback of these short wavelengths is that most materials – including air – are highly absorptive in this range [203]. Thus, no refractive optics like lenses can be used.

However, absorption already limits the use of lenses at wavelengths closer to the visible range. As briefly mentioned in section 3.4, the absoption of most glasses rapidly increases when going from the visible into the UV regime [105]. This sets a lower boundary for the wavelength used in 3D laser printing of about 400 nm. Therefore, highest resolution in 3D laser printing can be achieved exploiting a laser at around 400 nm focused by a high-NA objective lens. As just discussed, a wavelength reduction by a factor of two from the usually employed around 800 nm down to 400 nm directly correlates to an improvement of the 3D resolution by a factor of two at no additional cost. However, 3D laser printing at 405 nm is only rarely applied until now [12, 89]. For most applications, highest resolution is not necessary since the smallest features exceed the voxel size by far. Though, some special applications depend on every bit of achievable resolution. Woodpile photonic crystals for the low visible range as well as kinoform lenses are examples.

Kinoforms are a special variant of Fresnel zone plates (FZPs). Both are often used in X-ray microscopy [204, 205]. The easiest version of a FZP is a binary FZP. It comprises of concentric annuli which alternate between opaque zones and zones that are fully transparent for the used light. Thus, they form a diffraction pattern which is used to focus the light instead of utilizing a refractive optic. The focusing efficiency of such binary FZPs is very limited though and only reaches around 10 % in the theoretical limit. This low focusing efficiency can be explained by the fact that two rays within the same zone but at a different radial position get the same optical pathlength deviation.

Therefore, the binary FZP can be improved by introducing a surface profile to each zone. With that, the intra-periodic optical path-length difference can be corrected for each of the zones yielding to a focussing efficiency of 100 % in the theoretical lossless limit [206]. These specialized FZPs are called kinoforms [207, 208]. Usually, the correction exploits distinctive parabolic profiles within each

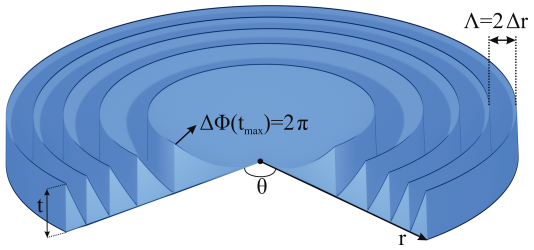

Figure 6.1: **Scheme of a kinoform.** The parabolic shape within each zone is illustrated. The resolution of the kinoform is mainly defined by the outermost period Λ which equals two outermost zone widths Δr of the corresponding binary FZP. Adapted from Ref. [90].

zone. The thickness t is calculated such that the optical path difference $\Delta\Phi$ at the maximum thickness amounts 2π. A schematic of the kinoform structure is shown in Figure 6.1.

The exact parameters of the kinoform directly translate into the focusing quality of the lens. Important are the outermost zone width Δr, the absolute diameter of the lens, and the total number of zones. The outermost zone width correlates linearly to the focal spot size, meaning a reduction of the outermost zone width by a factor of two results in a focal spot that is two times smaller, in theory. The diameter of the lens and the total number of zones associate with the focal plane intensity [206].

Hence, a small zone width, especially a small outermost zone width is highly desirable. This leads to a complex 3D profile and high aspect ratios on a nanoscale exacerbating the manufacturing of such lenses. Thus, they are usually manufactured with electron beam lithography. Due to the utilization of electrons instead of light, the diffraction limit is surpassing that of conventional light-based methods like 3D laser printing. However, it comes at the cost of extremely small print speeds in the range of $\mu m\,s^{-1}$, hence, high costs and a long waiting time for one lens to be manufactured. Not to mention that an iterative optimization process for the structure is inconceivable.

6.2 3D Laser Printing of a Kinoform

As an alternative to electron beam lithography, kinoforms can be manufactured by 3D laser printing [209]. Here, they employ a commercial Nanoscribe PPGT2 printer working at 780 nm wavelength for manufacturing. Given the limited resolution of the commercial system at 780 nm wavelength, the minimum outermost period they realize is 800 nm, which corresponds to an outermost zone width of 400 nm. The diameter of the lens results in 32 µm.

However, the resolution of the kinoform can be improved by a factor of two when reducing the outermost zone width by a factor of two. Therefore, we employ excitation at a reduced wavelength of 405 nm to print kinoforms. The

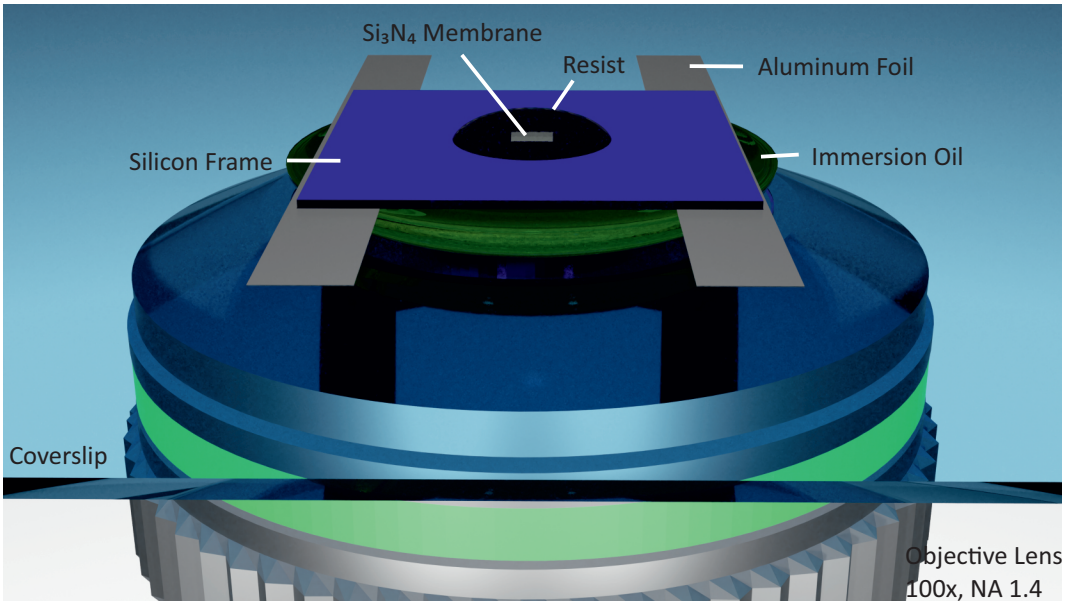

Figure 6.2: **Scheme of the intricate writing configuration.** The substrate comprising a $5 \times 5 \times 0.1\,\mathrm{mm}^3$ silicon frame containing a 100 nm thick silicon nitride membrane is glued on top of a standard glass coverslip with a thickness of 170 µm such that the silicon nitride membrane faces the coverslip. Small stripes of aluminum foil serve as spacers to prevent damage of the fragile membrane through contact. A high-NA oil-immersion objective lens focuses the light pulses at a center wavelength of 405 nm through the coverslip and the optically transparent membrane into the droplet of liquid photoresist. Refractive-index matching for high focus quality is guaranteed by immersion oil between the objective lens and the coverslip as well as between the coverslip and the substrate. Adapted from Ref. [90].

change of wavelength comes along with a change of the photoresist composistion, because common two-photon initiators work under one-photon absorption at this wavelength. However, common monomers such as PETA can be directly excited by two-photon absorption at 405 nm wavelength without the need for an additional photoinitiator [12]. Thus, the monomer itself can trigger the radical chain-growth reaction.

For fabrication, a home-built 3D laser printer is employed which allows for two-photon excitation at 405 nm wavelength. The setup is the same setup as used in chapter 4 for characterizing the objective lenses by a gold bead raster scanning method and bases on the setup originating from Joachim Fischer in 2011 [163] with additional modifications for accessing multiple wavelengths. In our application, a femtosecond-pulsed Ti:sapphire laser (MaiTai HP, SpectraPhysics) tuned to 810 nm wavelength is frequency doubled in a SHG crystal to a center wavelength of 405 nm. An acousto-optic modulator is used for power modulation. The laser is tightly focused by a 100 × / NA 1.4 oil immersion microscope objective lens (HCX

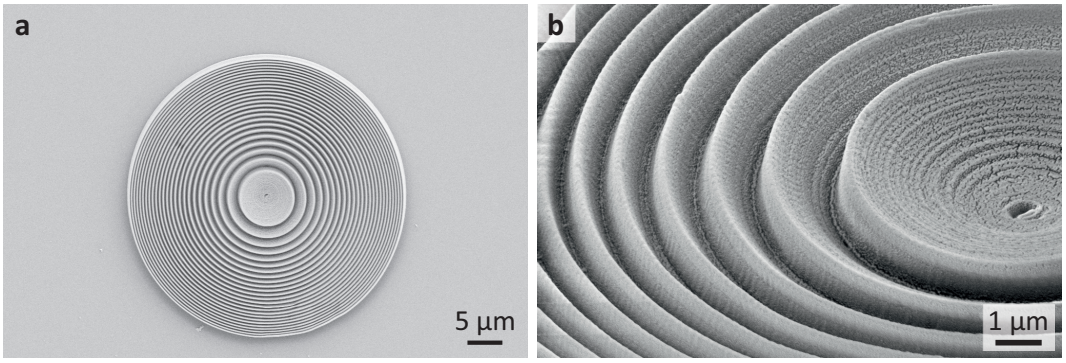

Figure 6.3: **Scanning electron micrographs of a fabricated kinoform. a** Top-view of the full kinoform with a diameter of 40 µm. **b** Oblique view of its first inner ridges in more detail. For scanning electron microscope investigation, the kinoform is printed directly on a glass coverslip instead of the silicon nitrid membrane. All other printing parameters remain the same. Adapted from Ref. [90].

PL APO 100 × /1.4 – 0.7 Oil CS, Leica, 230 µm free working distance). As scan unit, a three-dimensional piezoelectric stage (P-527.3CL, PhysikInstrumente) is employed.

The kinoforms are directly printed on silicon nitride membranes ($500 \times 500 \times 100\,\mathrm{nm}^3$) embedded in a silicon frame ($5 \times 5 \times 0.1\,\mathrm{mm}^3$) which are commonly used in X-ray microscopy setups. This enables characterization of the written and developed lenses in X-ray microscopy experiments without any further processing of the sample. To enable covalent binding between the structure and the substrate, the latter are silanized using a solution of 3-(trimethoxysilyl)propyl methacrylate in toluene. Due to the limited working distance of the objective lens, an intricate writing configuration was implemented shown in Figure 6.2.

The 3D models of the kinoforms are generated as STL files with a thickness of 2 µm, an outermost period of 400 nm, and an X-ray energy of 700 eV according to the usual set of parametric equations [210] using the *XYZ* Math Surface add-on of the free 3D graphics software Blender. Thus, resulting in an overall diameter of 40 µm and an aspect ratio of 5 for the smallest features. Following the procedure in section 2.2, the 3D models are converted into trajectories using the commercial software DeScribe (Nanoscribe GmbH). A slicing and hatching distance of 100 nm is chosen. The writing parameters are systematically optimized leading to best results for a mean laser power of 1.5 mW as measured at the entrance pupil of the objective lens and a writing speed of $25\,\mu\mathrm{m\,s}^{-1}$. Finally, the samples are developed in mr-Dev 600 (micro resist technology GmbH) for 15 min. After transfer to Aceton, they are dried in a critical point drying process. Scanning electron micrographs of the final structures are shown in Figure 6.3.

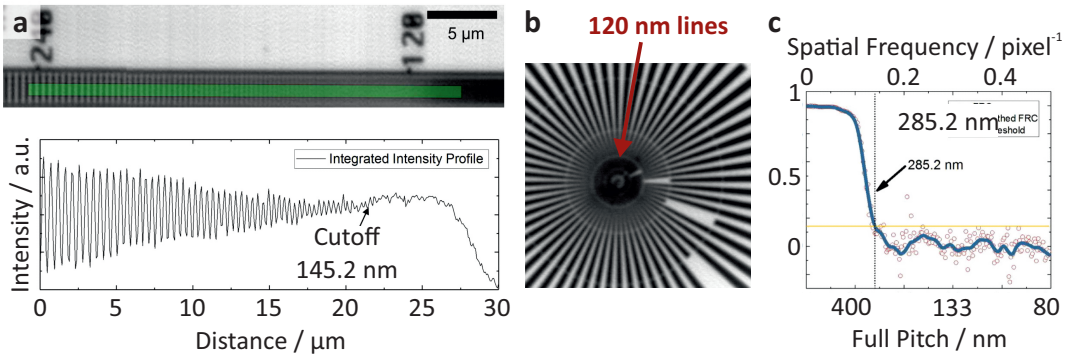

Figure 6.4: **Resolution tests in scanning transmission X-ray microscopy. a** A linear test sample comprised of gold strips with decreasing width and period is imaged (top) and evaluated along the integrated intensity profile of the green area (bottom). The cutoff resolution is found at 145 nm. **b** A Siemens star test sample is imaged. The red arrow indicates the second ring of the Siemens star corresponding to 120 nm lines and spaces. The spaces are not resolved anymore suggesting the resolution to be slightly worse than 120 nm. **c** Fourier ring correlation results from two images of the Siemens star acquired with the same parameters are plotted. The 1/7 threshold reveals a 285.2 nm full-pitch resolution corresponding to a 147.6 nm half-pitch resolution. Adapted from Ref. [90].

6.3 Focusing Performance in X-ray Microscopy

The performance of the 3D laser printed kinoform is tested at the magnetic X-ray microscope with UHV spectroscopy (MAXYMUS) at the UE46-PGMII beamline of BESSY II. This is a state-of-the-art scanning transmission X-ray microscope (STXM). These performance tests were conducted by Umut Sanli and Markus Weigand. Thus, this thesis will not present a detailed description of the conducted experiments and their results but only briefly summarize the main achievements.

The diffraction efficiency is measured in the photon energy range of 600 – 1100 eV, reaching 7.6 % at 700 eV as a maximum. Further, the cutoff resolution is deduced from three independent experiments: an STXM image of a linear test sample comprised from gold strips with decreasing width and period, an STXM image of a Siemens star test sample, and a Fourier ring correlation with a 1/7 threshold. The resulting half-pitch cutoff resolutions are estimated to 145 nm, 120 nm, and 147 nm, respectively, thus being very consistent.

Figure 6.4 summarizes the three different measurement results. The overall improvement in scanning transmission X-ray microscopy image resolution is 40 % as compared to the work employing the commercial 3D laser printer at a wavelength of 780 nm. In addition, the incident dose on the sample is a good figure-of-merit for the performance in ptychography [211], where the lens is made

for. Here, an improvement by a factor of 1.6 is obtained compared to the other work. In theory, an improvement by a factor of 2 is to be expected. However, the rather low diffraction efficiency of 7.6 % is strongly affecting this value. Looking only at the improvement for the half-pitch cutoff resolution, an improvement by roughly a factor of 2 is achieved, indeed.

6.4 Discussion and Outlook

In summary, we demonstrated the successful implementation of the direct two-photon excitation of the monomer PETA at a wavelength of 405 nm for printing a delicate kinoform. Up to now, this wavelength range is only exploited little in 3D laser printing. However, it comes along with great advantages compared to conventional 3D laser printing at 780 nm wavelength. The most important being the improvement in resolution by almost a factor of 2 at no other cost, just given by the diffraction limit of the optical system. This higher resolution is beneficial for the presented kinoforms. Their performance in direct scanning transmission X-ray microscopy is directly connected to the minimum outermost zone width. A reduction of the excitation wavelength for fabrication, hence, enables smaller outermost zone widths.

As presented, we successfully realized high-resolution kinoforms fabricated by 3D laser printing at 405 nm wavelength with a measured focusing efficiency of 7.5 % at 700 eV photon energy with a half-pitch resolution down to 145 nm. This results in a 1.6-fold improvement of the figure-of-merit for its performance in ptychography as compared to previous best results obtained by 3D laser printed kinoforms. We have to note, that an improvement by a factor of roughly 2 is expected in theory due to the halved outermost zone width.

We partly attribute the worse-than-expected performance to the measured nonconcentricity of 385 nm and slight tilt in the inner zones of the printed kinoform (see Figure 6.5). These effects are likely caused by a sample drift during the rather long fabrication process with about 3 h. The slow fabrication grounds in the low print speed which is necessary to nicely follow the small circular trajectories employing the piezoelectric stage. As discussed in Figure 2.1, scanning the light with a pair of galvanometric mirrors, for example, could drastically reduce the manufacturing time down to a few minutes or even less. This would certainly improve the performance of the 3D laser printed kinoforms. However, the beam-scanning option was not yet implemented in the used 3D laser printing setup during the experiments.

Still, compared to alternative manufacturing approaches like electron beam lithography and focused-ion-beam milling, the presented manufacturing times are small. In addition, the costs of our kinoforms are negligible against the

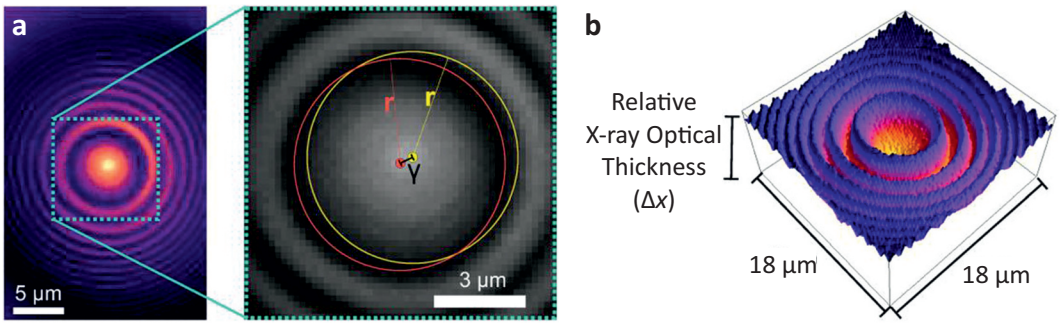

Figure 6.5: **Measurements showing imperfections in concentricity and a slight tilt.** **a** A scanning transmission X-ray micrograph of a 3D laser printed kinoform imaged employing a second nominally identical kinoform (left). The nonconcentricity is calculated to 385 nm by the difference between the brightest pixel of the image and the center of the innermost zone. For illustration the results are overlaid in the scanning electron micrograph of an identical kinoform (right). **b** A map of the optical thickness Δx is deduced from the STXM image in **a**. It reveals a slight tilt in the innermost zones of the kinoform. Adapted from Ref. [90].

costs of around ten thousand Euros of a kinoform with comparable resolution manufactured by the other means. Further, the achieved focusing efficiencies even surpass those obtained utilizing focused-ion-beam-milled gold kinoforms [212]. Thus, our results show that 3D laser printed kinoforms are a good choice especially for ptychographic applications.

A second small side effect of 3D laser printing at 405 nm excitation wavelength not having mentioned so far and rather unrelated to the presented usecase involves the change in the photoresist system, which in this case just consists of the pure monomer without any additional photoinitiator. The initiator molecules are chosen for a high quantum yield for radical formation, but usually still possess a non-vanishing autofluorescence in the visible range which is undesired especially in many biological applications [213–215]. Thus, even special photoresists with low autofluorescence are developed [216]. However, printing without any photoinitiator at 405 nm wavelength would also circumvent this problem. Therefore, adding another potential to 3D laser printing at 405 nm wavelength.

7 Chapter 7
Conclusions and Outlook

In this thesis, I have successfully addressed different open aspects in 3D laser printing which surpass the common. With the realization of a compact 3D laser printer and the utilization of smaller excitation wavelengths for printing, the challenges for physics towards improvements of the printing devices was worked on. Further, the novel resist system which merges additive and subtractive manufacturing together with adaptions on known resist system for enabling two-step-absorption-based or 405 nm-based 3D laser printing tackled the challenges for chemistry towards novel materials. The thesis was split into three parts accordingly.

In chapter 2, I have introduced the fundamentals of common 3D laser printing. I condensed state-of-the-art 3D laser printers to their five crucial components: light source, power modulation, focusing unit, scan unit, and control unit. These are also the elements which remained constant throughout the thirty years of 3D laser printing. Still, I showed the different possible solutions for each of the components which evolved over the years. Further, I addressed the common chemistry behind 3D laser printing including a detailed look at the standard excitation mechanism of two-photon absorption. In this regard, I presented important models for 3D laser printing with the threshold dose and dose accumulation. Finally, I concluded with discussions about the restrictions of 3D laser printing, where I focused on the resolution limit and its difference to the minimal obtainable feature size along with the discussions on placing heat into the resist during the printing process and other constraints for 3D laser printing resist systems.

In chapter 3, I have reviewed two-photon absorption as an alternative excitation mechanism for 3D laser printing as the basis to enable compact 3D laser printers. I showed the differences between common two-photon absorption and two-step absorption and their impact on the excitation process. I discussed the effective nonlinearity in two-step absorption in detail as it introduces limitations for the 3D printing process which are unknown from ordinary two-photon 3D laser printing. Therefore, I covered further important properties of two-step photoinitiators such as the importance of the absorption bands, the triplet ground-state energy, and an inert intermediate state. I finished this chapter by introducing the photoinitiator

benzil as a suitable candidate for two-step-absorption-based 3D laser printing and reviewed alternatives for both the group of molecules capable of two-step absorption and the generalized excitation principle of $(1 + 1)$-photon absorption.

In chapter 4, I have presented the realization of a low-cost 3D laser printer in the size of a shoebox on the basis of a tiny edge-emitting semiconductor laser diode and a MEMS scanner. I described the compacting of the optical setup and the involved components with their respective importance for the system. I address the draw-back of the elliptical beam shape of the employed laser diode by the need for spatial filtering and its influence on the print quality. Further, our approach also tackled the challenge for a compact control unit on the basis of a powerful microcontroller to step towards a stand-alone device. Thus, the implementation of the necessary hardware and software was described along with the different data connections and conversions of the involved components. In addition, the performance of the shoe-box-sized 3D laser printer was evaluated by printing different challenging three-dimensional structures. Here, I also addressed the possible replacement of the expensive NA 1.4 objective lens by a NA 1.25 objective lens at a cost of only 150 Euros and the difference in print quality. Finally, I studied the resolution of the shoe-box-sized 3D laser printer by printing two- and three-dimensional benchmark structures, proving the capability of achieving similar results as previously obtained in two-step-absorption 3D laser printing with a 3D laser printer at a cost of less than 10 000 Euros and the size of a shoe-box.

In chapter 5, I have introduced a novel material that enables both two-photon induced additive and subtractive manufacturing. I started with introducing the synthesized monomer and the underlying principle of the collaborative work with Rhiannon Batchelor. Next, I showed its ability for the utilization in high-resolution 3D laser printing at one wavelength by printed three-dimensional test structures and the involved optimization of the corresponding printing parameters. The cleaving at another wavelength was shown in different ways, to prove the mechanism being light-induced: One-photon experiments were conducted on the monomer in solution as well as on previously 3D laser printed structures. Further, two-photon induced cleaving of delicate three-dimensional structures inside of cuboids was presented and demarcated from thermally induced ablation with a control resist system treated under same condition but which does not allow for photoinduced bond-scission. Finally, I presented the capability of a multimaterial system comprising sacrificial structures out of the introduced resist for spatially controlled removal of additional structures printed on top.

In chapter 6, I have shown the implementation of a reduced excitation wavelength in a home-built 3D laser printer improving the resolution for printing. I presented the use-case of 3D laser printing kinoforms, a special type of Fresnel zone plates, used as lenses in X-ray microscopy with this device in a collaboration with Umut Sanli. I reviewed the importance of the improved resolution for such kind of structure due to the direct connection of the resolving power of the

kinoform to the width and period of the outermost rings. Further, I discussed the intricate writing configuration we developed to fabricate the structures directly on fragile silicon nitride membranes as they are commonly used in X-ray microscopy. I concluded this chapter with a brief summary of the focusing performance in scanning transmission X-ray microscopy experiments as conducted by the collaboration partner. The 3D printed kinoforms showed an improved performance compared to other lenses manufactured by conventional 3D laser printing. Still, imperfections of the manufacturing were discussed and open further improvement.

Outlook

In the discussions in chapter 4, chapter 5, and chapter 6, I have already addressed perspectives for future developments and improvements. I want to emphasize that all different projects I have presented in this thesis have in common that they feature novel concepts going beyond common 3D laser printing.

The shoe-box-sized 3D laser printer for example could help further spreading the technology of 3D laser printing since its low cost and size makes 3D laser printing more accessible to other communities. We discussed the inherent limitations of the alternative excitation mechanism due to the nature of the employed photoinitiator to date as an example. Still, two-step absorption is just at its beginning. So far, research focused mainly on the photoinitiator and swept already some possible candidates. However, the influence of different quencher molecules was not yet systematically investigated. In general, there are still fundamental open questions on the mechanism. Some of which are the interplay of the photoinitiator and the quencher, the mechanism of the quenching itself, and the influence of oxygen as a quencher. Especially the latter could be directly addressed with the shoe-box-sized 3D laser printer, since it could eventually be used in an inert atmosphere, such as in a glove box, which so far was hardly achievable due to the large setups. Thus, we expect a possible boost of the technology itself with more people working in this field and hope the compact and low-cost 3D laser printer can help with that.

Similarly, the presented results on spatially-controlled ligth-induced erasing of structures are the first ever attempts besides chemically uncontrolled ablation. The use of one single device just tuned to a different wavelength within seconds for both high-resolution three-dimensional additive structuring and high-resolution three-dimensional subtractive structuring will open new possibilities in 3D manufacturing. Yet, applications in microfluidics or biology have to establish. For the latter, it is of great importance that the residues of the cleaving process are compatible with the presence of cells. As mentioned in chapter 5, a fully reversible system would highly push the capabilities of such a system.

Finally, the potential of the improved resolution exploiting 405 nm excitation is unexhausted. Most of the common applications of 3D laser printing do not

rely on highest resolution. However, the resolution achieved by going to 405 nm wavelength gets more compatitive with other manufacturing techniques in this range of resolution like electron beam lithography or ion beam milling. The main advantage compared to those manufacturing techniques lies in the many orders of magnitude higher print speeds though. In principle, similar devices for rapid manufacturing as the ones to boost conventional 3D laser printing can be used by just adding a SHG crystal cavity for frequency doubling. Furthermore, the fact that monomers can directly be excited without the need of additional photoinitiator molecules can be of outmost interest for applications where autofluorescence of the resist comes relevant. This is true for many biological applications among others.

In summary, I had the chance to further develop a fascinating and still emerging technology in various aspects beyond the common during my PhD. Many of these things are just about to start with yet unknown full capabilities.

Appendix A

A Oscillograms for Setting the Filter Clock Frequency

As explained in subsection 4.3.3, setting the right filter clock frequency is crucial for the shoe-box-sized 3D laser printer. The measurements are performed with Michael Hippe using a digital oscilloscope. They all show a line scan of 5 µm. The yellow channel is connected to the output trigger of the microcontroller where each peak corresponds to sending a new data point to the digital MEMS driver. The magenta curve is connected to the laser output of the microcontroller. The blue and green channels are connected to the X+ and X- output channel of the digital MEMS driver. Figure A.1 shows a measurement for the standard filter clock frequency of 60 kHz, Figure A.2 shows the measurement for a standard filter clock frequency of 500 kHz, and Figure A.3 shows a measurement for the standard filter clock frequency of 3 MHz.

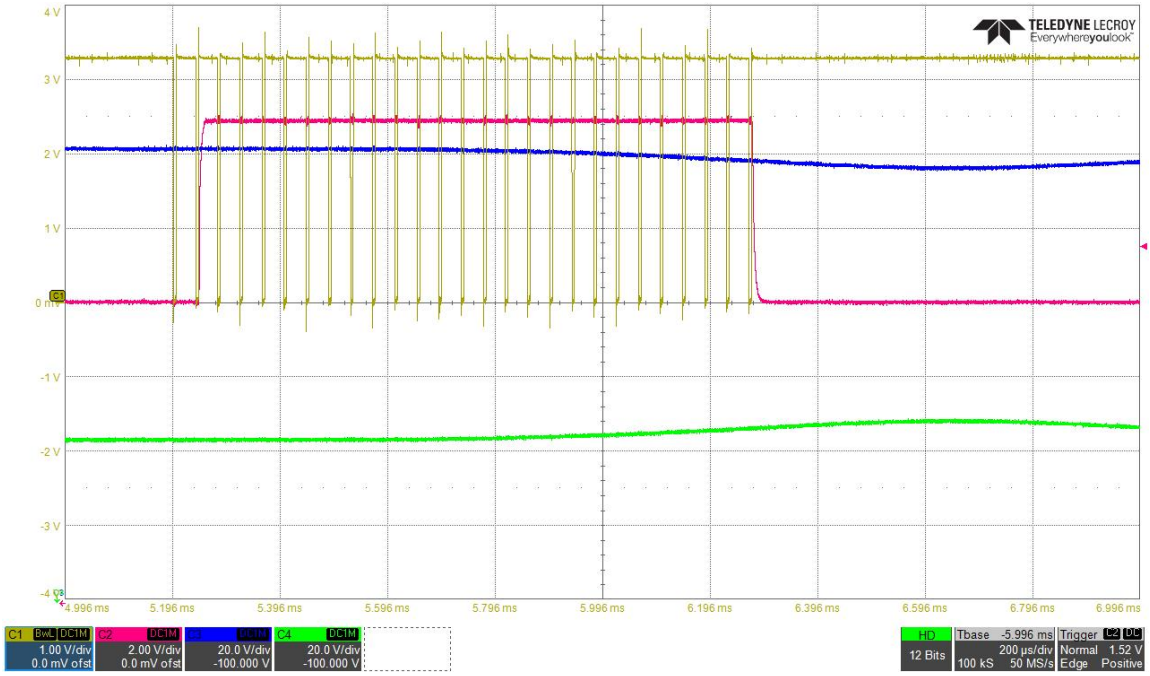

Figure A.1: **Measurement with filter clock frequency set to 60 kHz.**

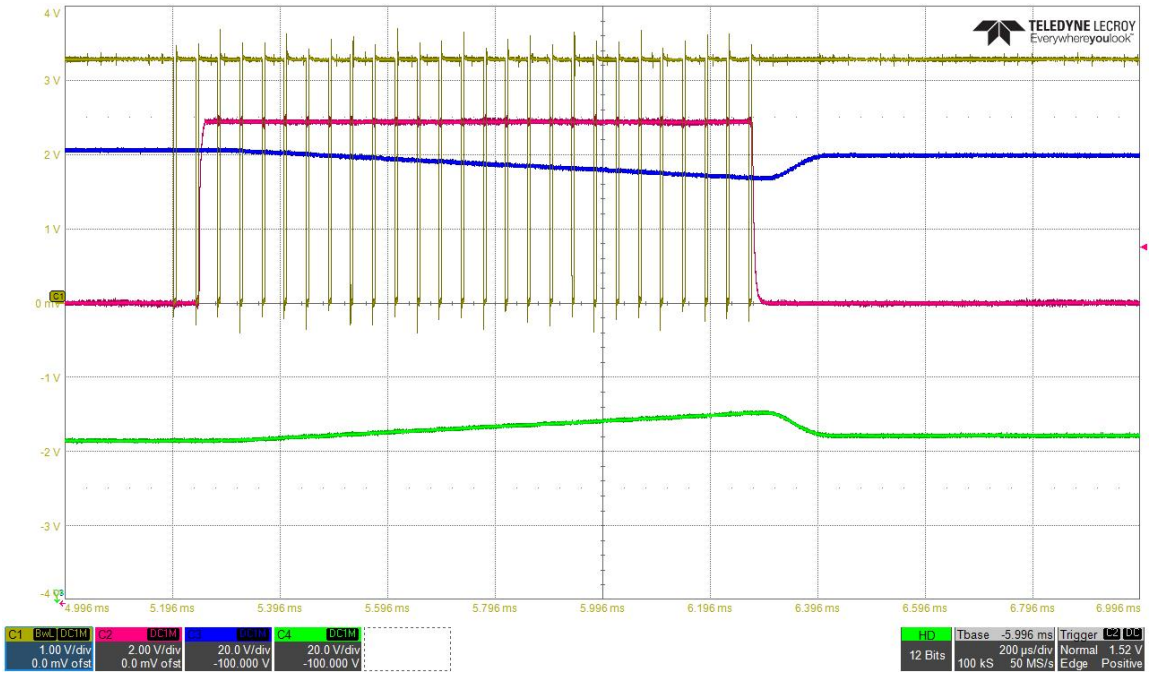

Figure A.2: **Measurement with filter clock frequency set to 500 kHz.**

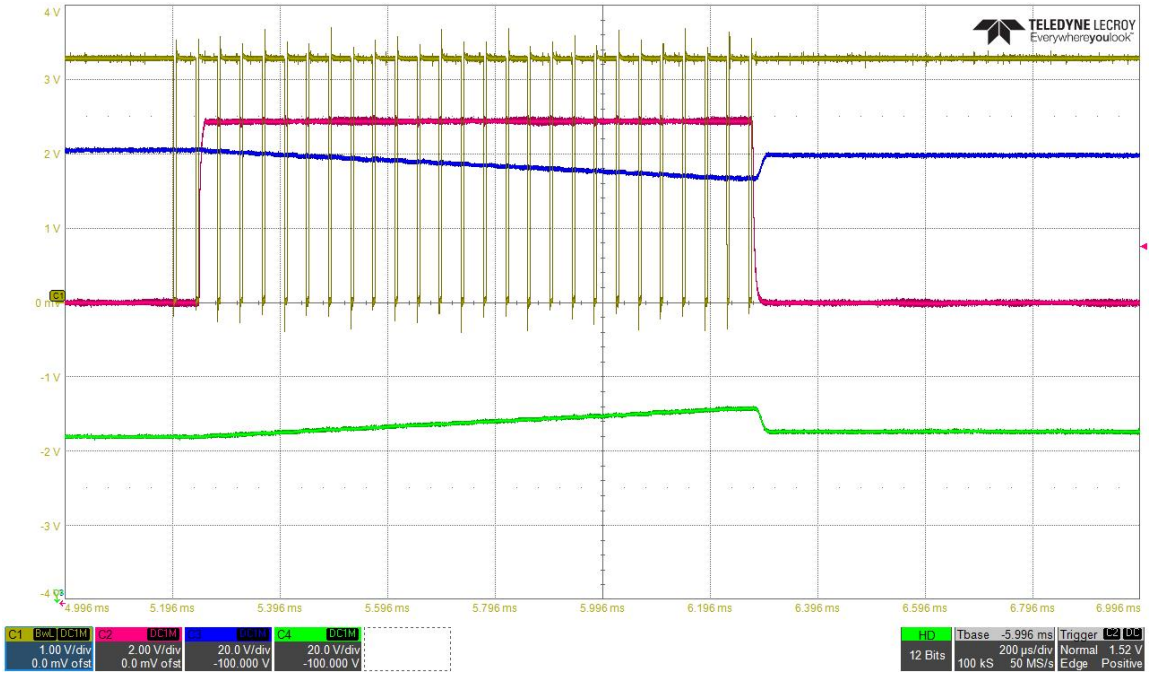

Figure A.3: **Measurement with filter clock frequency set to 3 MHz.**

Bibliography

[1] S. Maruo, "Three-dimensional microfabrication with two-photon absorbed photopolymerization", in 17th Congress of the International Commission for Optics: Optics for Science and New Technology, Vol. 2778 (SPIE, 1996), pp. 202–203 (cited on page 3).

[2] S. Maruo, O. Nakamura, and S. Kawata, "Three-dimensional microfabrication with two-photon-absorbed photopolymerization", Opt. Lett. **22**, 132–134 (1997) (cited on pages 3, 21).

[3] S. C. Gauci, A. Vranic, E. Blasco, S. Bräse, M. Wegener, and C. Barner-Kowollik, "Photochemically Activated 3D Printing Inks: Current Status, Challenges, and Opportunities", Advanced Materials, 2306468 (2023) (cited on pages 3, 28).

[4] H. Wang, W. Zhang, D. Ladika, H. Yu, D. Gailevičius, H. Wang, C.-F. Pan, P. N. S. Nair, Y. Ke, T. Mori, J. Y. E. Chan, Q. Ruan, M. Farsari, M. Malinauskas, S. Juodkazis, M. Gu, and J. K. W. Yang, "Two-Photon Polymerization Lithography for Optics and Photonics: Fundamentals, Materials, Technologies, and Applications", Advanced Functional Materials **33**, 2214211 (2023) (cited on pages 3, 8, 20, 28, 80).

[5] V. Hahn, P. Kiefer, T. Frenzel, J. Qu, E. Blasco, C. Barner-Kowollik, and M. Wegener, "Rapid Assembly of Small Materials Building Blocks (Voxels) into Large Functional 3D Metamaterials", Advanced Functional Materials **30**, 1907795 (2020) (cited on pages 3, 10, 42, 56, 59).

[6] X. Zhou, Y. Hou, and J. Lin, "A review on the processing accuracy of two-photon polymerization", Aip Advances **5**, 030701 (2015) (cited on pages 4, 28).

[7] V. Hahn, F. Mayer, M. Thiel, and M. Wegener, "3-D Laser Nanoprinting", Opt. Photon. News **30**, 28–35 (2019) (cited on pages 4, 21, 28, 80).

[8] V. Harinarayana and Y. Shin, "Two-photon lithography for three-dimensional fabrication in micro/nanoscale regime: A comprehensive review", Optics & Laser Technology **142**, 107180 (2021) (cited on pages 4, 28).

[9] L. Yang, F. Mayer, U. H. Bunz, E. Blasco, and M. Wegener, "Multi-material multi-photon 3D laser micro-and nanoprinting", Light: Advanced Manufacturing **2**, 296–312 (2021) (cited on pages 4, 28).

[10] C. A. Spiegel, M. Hippler, A. Münchinger, M. Bastmeyer, C. Barner-Kowollik, M. Wegener, and E. Blasco, "4D Printing at the Microscale", Advanced Functional Materials **30**, 1907615 (2020) (cited on pages 4, 28).

[11] E.-S. Wu, J. H. Strickler, W. R. Harrell, and W. W. Webb, "Two-photon lithography for microelectronic application", in Optical/Laser Microlithography V, Vol. 1674 (SPIE, 1992), pp. 776–782 (cited on pages 4, 27).

[12] P. Müller, M. Thiel, and M. Wegener, "3D direct laser writing using a 405 nm diode laser", Opt. Lett. **39**, 6847–6850 (cited on pages 4, 11, 28, 34, 73, 74, 96, 98).

[13] J. Fischer and M. Wegener, "Three-dimensional direct laser writing inspired by stimulated-emission-depletion microscopy", Opt. Mater. Express **1**, 614–624 (2011) (cited on pages 4, 11, 72–74).

[14] P. Müller, M. M. Zieger, B. Richter, A. S. Quick, J. Fischer, J. B. Müller, L. Zhou, G. U. Nienhaus, M. Bastmeyer, C. Barner-Kowollik, and M. Wegener, "Molecular Switch for Sub-Diffraction Laser Lithography by Photoenol Intermediate-State Cis–Trans Isomerization", ACS Nano **11**, 6396–6403 (2017) (cited on pages 4, 82).

[15] P. Müller, R. Müller, L. Hammer, C. Barner-Kowollik, M. Wegener, and E. Blasco, "STED-Inspired Laser Lithography Based on Photoswitchable Spirothiopyran Moieties", Chemistry of Materials **31**, 1966–1972 (2019) (cited on pages 4, 82).

[16] R. R. Gattass and E. Mazur, "Femtosecond laser micromachining in transparent materials", Nature photonics **2**, 219–225 (2008) (cited on page 4).

[17] W. Xiong, Y. S. Zhou, X. N. He, Y. Gao, M. Mahjouri-Samani, L. Jiang, T. Baldacchini, and Y. F. Lu, "Simultaneous additive and subtractive three-dimensional nanofabrication using integrated two-photon polymerization and multiphoton ablation", Light: Science & Applications **1**, e6–e6 (2012) (cited on pages 4, 80).

[18] Nanoscribe GmbH, *DataSheet QuantumX*, (2023) https://www.nanoscribe.com/en/products/quantum-x/ (cited on pages 4, 9).

[19] Femtika, *Laser Nanofactory - Multi-Photon Polimerization*, (2023) https://femtika.com/product/multiphoton-polimerization/#specifications (cited on pages 4, 9).

[20] UpNano GmbH, *UpNano Factsheet*, (2021) https://www.axt.com.au/products/nanoone-3d-printer/ (cited on pages 4, 9).

[21] M. Shusteff, A. E. M. Browar, B. E. Kelly, J. Henriksson, T. H. Weisgraber, R. M. Panas, N. X. Fang, and C. M. Spadaccini, "One-step volumetric additive manufacturing of complex polymer structures", Science Advances **3**, eaao5496 (2017) (cited on page 8).

[22] B. E. Kelly, I. Bhattacharya, H. Heidari, M. Shusteff, C. M. Spadaccini, and H. K. Taylor, "Volumetric additive manufacturing via tomographic reconstruction", Science **363**, 1075–1079 (2019) (cited on page 8).

[23] P. N. Bernal, P. Delrot, D. Loterie, Y. Li, J. Malda, C. Moser, and R. Levato, "Volumetric Bioprinting of Complex Living-Tissue Constructs within Seconds", Advanced Materials **31**, 1904209 (2019) (cited on page 8).

[24] D. Loterie, P. Delrot, and C. Moser, "High-resolution tomographic volumetric additive manufacturing", Nature communications **11**, 852 (2020) (cited on page 8).

[25] M. Regehly, Y. Garmshausen, M. Reuter, N. F. König, E. Israel, D. P. Kelly, C.-Y. Chou, K. Koch, B. Asfari, and S. Hecht, "Xolography for linear volumetric 3D printing", Nature **588**, 620–624 (2020) (cited on pages 8, 38, 46).

[26] V. Hahn, P. Rietz, F. Hermann, P. Müller, C. Barner-Kowollik, T. Schlöder, W. Wenzel, E. Blasco, and M. Wegener, "Light-sheet 3D microprinting via two-colour two-step absorption", Nature Photonics **16**, 784–791 (2022) (cited on pages 8, 38, 42).

[27] C. N. LaFratta, J. T. Fourkas, T. Baldacchini, and R. A. Farrer, "Multiphoton Fabrication", Angewandte Chemie International Edition **46**, 6238–6258 (2007) (cited on pages 9, 11).

[28] M. Malinauskas, P. Danilevičius, and S. Juodkazis, "Three-dimensional micro-/nano-structuring via direct write polymerization with picosecond laser pulses", Opt. Express **19**, 5602–5610 (2011) (cited on page 9).

[29] Coherent, *Chameleon Ultra Datasheet*, (2019) https://content.coherent.com/legacy-assets/pdf/COHR_ChameleonUltra_DS_0119_3.pdf (cited on page 9).

[30] Newport Corporation, *Mai Tai Datasheet*, (2021) https://www.spectra-physics.com/mam/celum/celum_assets/resources/Mai-Tai-Datasheet.pdf (cited on page 9).

[31] V. Hahn, T. Messer, N. M. Bojanowski, E. R. Curticean, I. Wacker, R. R. Schröder, E. Blasco, and M. Wegener, "Two-step absorption instead of two-photon absorption in 3D nanoprinting", Nature Photonics **15**, 932–938 (2021) (cited on pages 11, 36, 38, 39, 42, 44–46, 52, 53, 58, 66, 72, 73).

[32] M. Thiel, A. Bertoncini, T. Hoose, and M. Blaicher, "Advancement in two-photon grayscale lithography", in Advanced Fabrication Technologies for Micro/Nano Optics and Photonics XVI (International Society for Optics and Photonics, 2023) (cited on page 11).

[33] A. S. van de Nes, L. Billy, S. F. Pereira, and J. J. M. Braat, "Calculation of the vectorial field distribution in a stratified focal region of a high numerical aperture imaging system", Opt. Express **12**, 1281–1293 (2004) (cited on page 12).

[34] Nanoscribe GmbH, "Introducing Two-Photon Grayscale Lithography", White paper (2021) (cited on pages 11, 28).

[35] S. Rodríguez, "Redefining Microfabrication of High-Precision Optics", PhotonicsViews **17**, 36–39 (2020) (cited on pages 11, 28).

[36] J. Fischer and M. Wegener, "Three-dimensional optical laser lithography beyond the diffraction limit", Laser & Photonics Reviews **7**, 22–44 (2013) (cited on pages 11, 26, 70).

[37] S. J. Rupitsch, *Piezoelectric sensors and actuators* (Springer, 2019), 559 pp. (cited on page 13).

[38] K. Spanner and B. Koc, "Piezoelectric motors, an overview", Actuators **5**, 6 (2016) (cited on page 13).

[39] L. Jonušauskas, D. Gailevičius, S. Rekštytė, T. Baldacchini, S. Juodkazis, and M. Malinauskas, "Mesoscale laser 3D printing", Opt. Express **27**, 15205–15221 (2019) (cited on page 15).

[40] S. Kawata, H.-B. Sun, T. Tanaka, and K. Takada, "Finer features for functional microdevices", Nature **412**, 697–698 (2001) (cited on page 16).

[41] T. Bückmann, N. Stenger, M. Kadic, J. Kaschke, A. Frölich, T. Kennerknecht, C. Eberl, M. Thiel, and M. Wegener, "Tailored 3D Mechanical Metamaterials Made by Dip-in Direct-Laser-Writing Optical Lithography", Advanced Materials **24**, 2710–2714 (2012) (cited on page 16).

[42] A. Münchinger, V. Hahn, D. Beutel, S. Woska, J. Monti, C. Rockstuhl, E. Blasco, and M. Wegener, "Multi-Photon 4D Printing of Complex Liquid Crystalline Microstructures by In Situ Alignment Using Electric Fields", Advanced Materials Technologies **7**, 2100944 (2022) (cited on page 16).

[43] M. Farsari and B. N. Chichkov, "Two-photon fabrication", Nature photonics **3**, 450–452 (2009) (cited on page 17).

[44] L. Li and J. T. Fourkas, "Multiphoton polymerization", Materials Today **10**, 30–37 (2007) (cited on page 17).

[45] J. B. Müller, "Exploring the Mechanisms of Three-Dimensional Direct Laser Writing by Multi-Photon Polymerization", PhD thesis (Karlsruher Institut für Technologie (KIT), Karlsruhe, 2015), 161 pp. (cited on pages 17, 27).

[46] J. Crivello, "Photoinitiated cationic polymerization", Annual review of materials science **13**, 173–190 (1983) (cited on page 17).

[47] A. Ostendorf and B. N. Chichkov, "Two-photon polymerization: a new approach to micromachining", Photonics spectra **40**, 72 (2006) (cited on page 18).

[48] J. O'Brien, P. J. Hughes, M. Brunet, B. O'Neill, J. Alderman, B. Lane, A. O'Riordan, and C. O'Driscoll, "Advanced photoresist technologies for microsystems", Journal of Micromechanics and Microengineering **11**, 353 (2001) (cited on page 18).

[49] M. Farsari, M. Vamvakaki, and B. N. Chichkov, "Multiphoton polymerization of hybrid materials", Journal of Optics **12**, 124001 (2010) (cited on page 18).

[50] M. Hippler, E. Blasco, J. Qu, M. Tanaka, C. Barner-Kowollik, M. Wegener, and M. Bastmeyer, "Controlling the shape of 3D microstructures by temperature and light", Nature communications **10**, 232 (2019) (cited on page 18).

[51] E. Blasco, J. Müller, P. Müller, V. Trouillet, M. Schön, T. Scherer, C. Barner-Kowollik, and M. Wegener, "Fabrication of Conductive 3D Gold-Containing Microstructures via Direct Laser Writing", Advanced Materials **28**, 3592–3595 (2016) (cited on page 18).

[52] L. Yang, H. Hu, A. Scholz, F. Feist, G. Cadilha Marques, S. Kraus, N. M. Bojanowski, E. Blasco, C. Barner-Kowollik, J. Aghassi-Hagmann, and M. Wegener, "Laser printed microelectronics", Nature Communications **14**, 1103 (2023) (cited on pages 18, 28).

[53] F. Kotz, A. S. Quick, P. Risch, T. Martin, T. Hoose, M. Thiel, D. Helmer, and B. E. Rapp, "Two-Photon Polymerization of Nanocomposites for the Fabrication of Transparent Fused Silica Glass Microstructures", Advanced Materials **33**, 2006341 (2021) (cited on page 18).

[54] R. J. Young, *Introduction to polymers* (Chapman and Hall, 1983) (cited on page 18).

[55] H. R. Allcock, F. W. Lampe, and J. E. Mark, *Contemporary Polymer Chemistry*, 3rd edition (Pearson Prentice Hall, 2003) (cited on page 18).

[56] J. M. G. Cowie and V. Arrighi, *Polymers: chemistry and physics of modern materials*, 3rd edition (CRC press, 2007) (cited on pages 18, 19).

[57] A. Rudin, *The Elements of Polymer Science and Engineering* (Academic Press, 1982), pp. 209–211 (cited on page 18).

[58] B. Tieke, *Makromolekulare Chemie: eine Einführung*, 3rd edition (Wiley-VCH, Weinheim, 2014), 392 pp. (cited on page 19).

[59] C. Decker and A. D. Jenkins, "Kinetic approach of oxygen inhibition in ultraviolet- and laser-induced polymerizations", Macromolecules **18**, 1241–1244 (1985) (cited on pages 19, 41).

[60] S. C. Ligon, B. Husár, H. Wutzel, R. Holman, and R. Liska, "Strategies to Reduce Oxygen Inhibition in Photoinduced Polymerization", Chemical Reviews **114**, 557–589 (2014) (cited on page 19).

[61] J. B. Müller, J. Fischer, F. Mayer, M. Kadic, and M. Wegener, "Polymerization Kinetics in Three-Dimensional Direct Laser Writing", Advanced Materials **26**, 6566–6571 (2014) (cited on pages 19, 22, 24, 41).

[62] M. F. Mayer, "On Multi-Material 3D Laser Microprinting", PhD thesis (Karlsruher Institut für Technologie (KIT), Karlsruhe, 2020), 148 pp. (cited on page 19).

[63] W. Zhou, S. M. Kuebler, K. L. Braun, T. Yu, J. K. Cammack, C. K. Ober, J. W. Perry, and S. R. Marder, "An Efficient Two-Photon-Generated Photoacid Applied to Positive-Tone 3D Microfabrication", Science **296**, 1106–1109 (2002) (cited on page 20).

[64] P. Kiefer, V. Hahn, M. Nardi, L. Yang, E. Blasco, C. Barner-Kowollik, and M. Wegener, "Sensitive Photoresists for Rapid Multiphoton 3D Laser Micro- and Nanoprinting", Advanced Optical Materials **8**, 2000895 (2020) (cited on pages 20, 36, 37).

[65] L. Yang, A. Münchinger, M. Kadic, V. Hahn, F. Mayer, E. Blasco, C. Barner-Kowollik, and M. Wegener, "On the Schwarzschild Effect in 3D Two-Photon Laser Lithography", Advanced Optical Materials **7**, 1901040 (2019) (cited on pages 20, 22, 24, 27).

[66] C. Arnoux, T. Konishi, E. Van Elslande, E.-A. Poutougnigni, J.-C. Mulatier, L. Khrouz, C. Bucher, E. Dumont, K. Kamada, C. Andraud, P. Baldeck, A. Banyasz, and C. Monnereau, "Polymerization Photoinitiators with Near-Resonance Enhanced Two-Photon Absorption Cross-Section: Toward High-Resolution Photoresist with Improved Sensitivity", Macromolecules **53**, 9264–9278 (2020) (cited on pages 20, 72).

[67] M. Malinauskas, A. Žukauskas, G. Bičkauskaitė, R. Gadonas, and S. Juodkazis, "Mechanisms of three-dimensional structuring of photo-polymers by tightly focussed femtosecond laser pulses", Opt. Express **18**, 10209–10221 (2010) (cited on page 21).

[68] M. Göppert-Mayer, "Über Elementarakte mit zwei Quantensprüngen", Annalen der Physik **401**, 273–294 (1931) (cited on pages 21, 35).

[69] W. Kaiser and C. G. B. Garrett, "Two-Photon Excitation in CaF_2: Eu^{2+}", Phys. Rev. Lett. **7**, 229–231 (1961) (cited on page 21).

[70] F. H. M. Faisal, *Theory of Multiphoton Processes* (Springer Science+Business Media New York, 1987), 408 pp. (cited on page 21).

[71] S. Guérin and H. R. Jauslin, "Control of Quantum Dynamics by Laser Pulses: Adiabatic Floquet Theory", in *Advances in Chemical Physics* (John Wiley & Sons, Ltd, 2003) Chap. 3, pp. 147–267 (cited on page 21).

[72] W. A. Green, *Industrial photoinitiators: a technical guide* (CRC Press, 2010), 306 pp. (cited on pages 21, 40, 44).

[73] S. J. Blanksby and G. B. Ellison, "Bond Dissociation Energies of Organic Molecules", Acc. Chem. Res. **36**, 255–263 (2003) (cited on page 22).

[74] R. Norrish and C. Bamford, "Photo-decomposition of Aldehydes and Ketones", Nature **140**, 195–196 (1937) (cited on pages 22, 41).

[75] S. Koltzenburg, M. Maskos, and O. Nuyken, *Polymer Chemistry*, 2nd edition (Springer-Verlag GmbH Germany, 2023), 634 pp. (cited on page 22).

[76] L. J. Jiang, Y. S. Zhou, W. Xiong, Y. Gao, X. Huang, L. Jiang, T. Baldacchini, J.-F. Silvain, and Y. F. Lu, "Two-photon polymerization: investigation of chemical and mechanical properties of resins using Raman microspectroscopy", Opt. Lett. **39**, 3034–3037 (2014) (cited on page 22).

[77] R. Zvagelsky, F. Mayer, D. Beutel, C. Rockstuhl, G. Gomard, and M. Wegener, "Towards in-situ diagnostics of multi-photon 3D laser printing using optical coherence tomography", Light: Advanced Manufacturing **3**, 466–480 (2022) (cited on page 22).

[78] E. H. Waller and G. Von Freymann, "Spatio-Temporal Proximity Characteristics in 3D μ-Printing via Multi-Photon Absorption", Polymers **8**, 10.3390/polym8080297 (2016) (cited on page 23).

[79] R. Wagner, *On the Simulation of Dose Accumulation in 3D Laser Nanoprinting*, Bachelor thesis, Karlsruher Institut für Technologie (KIT), Karlsruhe, 2022 (cited on pages 23, 59, 60).

[80] S. Wang, Y. Yu, H. Liu, K. T. P. Lim, B. M. Srinivasan, Y. W. Zhang, and J. K. W. Yang, "Sub-10-nm suspended nano-web formation by direct laser writing", Nano Futures **2**, 025006 (2018) (cited on page 25).

[81] L. Mohr-Weidenfeller, A.-V. Häcker, C. Reinhardt, and E. Manske, "Two-photon direct laser writing beyond the diffraction limit using the nanopositioning and nanomeasuring machine", Nanomanufacturing and Metrology **4**, 149–155 (2021) (cited on page 26).

[82] E. Abbe, "Beiträge zur Theorie des Mikroskops und der mikroskopischen Wahrnehmung", Archiv für mikroskopische Anatomie **9**, 413–468 (1873) (cited on page 26).

[83] C. M. Sparrow, "On Spectroscopic Resolving Power", Astrophys. J. **44**, 76 (1916) (cited on page 26).

[84] T. Ito and S. Okazaki, "Pushing the limits of lithography", Nature **406**, 1027–1031 (2000) (cited on pages 26, 96).

[85] A. Reiser, *Photoactive Polymers: The Science and Technology of Resists* (John Wiley & Sons, Hoboken, NJ, 1989), 410 pp. (cited on page 26).

[86] J. A. Hoffnagle, W. D. Hinsberg, M. I. Sanchez, and F. A. Houle, "Method of measuring the spatial resolution of a photoresist", Opt. Lett. **27**, 1776–1778 (2002) (cited on page 26).

[87] U. Okoroanyanwu, *Chemistry and Lithography* (SPIE & John Wiley & Sons, Hoboken, NJ, 2010), 862 pp. (cited on page 26).

[88] M. He, Z. Zhang, C. Cao, G. Zhou, C. Kuang, and X. Liu, "3D Sub-Diffraction Printing by Multicolor Photoinhibition Lithography: From Optics to Chemistry", Laser & Photonics Reviews **16**, 2100229 (2022) (cited on page 26).

[89] A. Wickberg, A. Abass, H.-H. Hsiao, C. Rockstuhl, and M. Wegener, "Second-Harmonic Generation by 3D Laminate Metacrystals", Advanced Optical Materials **7**, 1801235 (2019) (cited on pages 28, 96).

[90] U. T. Sanli, T. Messer, M. Weigand, L. Lötgering, G. Schütz, M. Wegener, C. Kern, and K. Keskinbora, "High-Resolution Kinoform X-Ray Optics Printed via 405 nm 3D Laser Lithography", Advanced Materials Technologies **7**, 2101695 (2022) (cited on pages 28, 97–100, 102).

[91] D. M. Zuev, A. K. Nguyen, V. I. Putlyaev, and R. J. Narayan, "3D printing and bioprinting using multiphoton lithography", Bioprinting **20**, e00090 (2020) (cited on page 28).

[92] T. Abele, T. Messer, K. Jahnke, M. Hippler, M. Bastmeyer, M. Wegener, and K. Göpfrich, "Two-Photon 3D Laser Printing Inside Synthetic Cells", Advanced Materials **34**, 2106709 (2022) (cited on pages 28, 29).

[93] K. Sugioka and Y. Cheng, "Femtosecond laser three-dimensional micro- and nanofabrication", Applied Physics Reviews **1**, 041303 (2014) (cited on page 28).

[94] C. Barner-Kowollik, M. Bastmeyer, E. Blasco, G. Delaittre, P. Müller, B. Richter, and M. Wegener, "3D Laser Micro- and Nanoprinting: Challenges for Chemistry", Angewandte Chemie International Edition **56**, 15828–15845 (2017) (cited on pages 28, 80).

[95] S. Braun, R. Zvagelsky, T. Messer, M. Holsten, P. Kollenz, A. de la Cruz Garcia, C. Selhuber-Unkel, M. Mastalerz, J. Freudenberg, M. Wegener, and U. H. F. Bunz, *Vinylcyclopropane Inks for Direct Laser Writing: Shrinkage Reduction*, in preparation, 2023 (cited on page 29).

[96] P. Kiefer, V. Hahn, S. Kalt, Q. Sun, Y. M. Eggeler, and M. Wegener, "A multi-photon (7× 7)-focus 3D laser printer based on a 3D-printed diffractive optical element and a 3D-printed multi-lens array", Light: Advanced Manufacturing **4**, 28-41 (2024) (cited on pages 34, 59).

[97] J. Fischer, J. B. Mueller, J. Kaschke, T. J. A. Wolf, A.-N. Unterreiner, and M. Wegener, "Three-dimensional multi-photon direct laser writing with variable repetition rate", Opt. Express **21**, 26244–26260 (2013) (cited on pages 34, 82).

[98] V. M. Hahn, "On 3D Laser Micro-and Nanoprinting: Faster, Finer, and More Affordable", PhD thesis (Karlsruher Institut für Technologie (KIT), Karlsruhe, 2022), 188 pp. (cited on pages 34, 37, 39, 42, 58).

[99] M. Thiel, J. Fischer, G. von Freymann, and M. Wegener, "Direct laser writing of three-dimensional submicron structures using a continuous-wave laser at 532 nm", Applied Physics Letters **97**, 221102 (2010) (cited on page 34).

[100] V. Hahn, N. M. Bojanowski, P. Rietz, F. Feist, M. Kozlowska, W. Wenzel, E. Blasco, S. Bräse, C. Barner-Kowollik, and M. Wegener, "Challenges and Opportunities in 3D Laser Printing Based on (1+ 1)-Photon Absorption", ACS Photonics **10**, 24–33 (2022) (cited on pages 34, 47).

[101] N. Liaros and J. T. Fourkas, "Methods for Determining the Effective Order of Absorption in Radical Multiphoton Photoresists: A Critical Analysis", Laser & Photonics Reviews **15**, 2000203 (2021) (cited on page 36).

[102] P. Klán and J. Wirz, *Photochemistry of organic compounds: from concepts to practice* (John Wiley & Sons, 2009), 563 pp. (cited on page 37).

[103] X. Liu, C. Ding, X. Gao, X. Shen, M. Tang, Z. Yang, L. Xu, C. Kuang, and X. Liu, "High-resolution 3D nanoprinting based on two-step absorption via an integrated fiber-coupled laser diode", Opt. Lett. **48**, 4300–4303 (2023) (cited on pages 38, 46, 53).

[104] Y. Zhang and H. Gross, "Systematic design of microscope objectives. Part I: System review and analysis", Advanced Optical Technologies **8**, 313–347 (2019) (cited on page 38).

[105] Y. Zhang and H. Gross, "Systematic design of microscope objectives. Part II: Lens modules and design principles", Advanced Optical Technologies **8**, 349–384 (2019) (cited on pages 38, 96).

[106] C. M. Marian, "Understanding and Controlling Intersystem Crossing in Molecules", Annual Review of Physical Chemistry **72**, 617–640 (2021) (cited on page 39).

[107] R. Englman and J. Jortner, "The energy gap law for radiationless transitions in large molecules", Molecular Physics **18**, 145–164 (1970) (cited on page 39).

[108] S. J. Jang, "A simple generalization of the energy gap law for nonradiative processes", The Journal of Chemical Physics **155**, 164106 (2021) (cited on page 39).

[109] J. H. Brannon and D. Magde, "Absolute quantum yield determination by thermal blooming. Fluorescein", The Journal of Physical Chemistry **82**, 705–709 (1978) (cited on page 40).

[110] N. J. Turro, *Molecular Photochemistry* (W. A. Benjamin, New York, 1967) (cited on pages 40, 41, 45).

[111] IUPAC, *Compendium of Chemical Terminology: The Gold Book*, Compiled by A. D. McNaught and A. Wilkinson. Blackwell Scientific Publications, Oxford (1997). Online version (2019-) created by S. J. Chalk. Version 3.0.1 (cited on page 41).

[112] A. P. Darmanyan, C. S. Foote, and P. Jardon, "Interaction of singlet oxygen with peroxy and acylperoxy radicals", The Journal of Physical Chemistry **99**, 11854–11859 (1995) (cited on page 41).

[113] P. Gijsman, "A review on the mechanism of action and applicability of Hindered Amine Stabilizers", Polymer Degradation and Stability **145**, 2–10 (2017) (cited on page 41).

[114] L. J. Johnston, M. Tencer, and J. C. Scaiano, "Evidence for hydrogen transfer in the photochemistry of 2,2,6,6-tetramethylpiperidine N-oxyl", The Journal of Organic Chemistry **51**, 2806–2808 (1986) (cited on page 41).

[115] A. Tatikolov, P. Levin, T. Kokrashvili, and V. Kuz'min, "Quenching of the triplet states of carbonyl compounds by nitroxyl radicals", Bulletin of the Academy of Sciences of the USSR, Division of chemical science **32**, 465–468 (1983) (cited on page 41).

[116] S. K. Saha, D. Wang, V. H. Nguyen, Y. Chang, J. S. Oakdale, and S.-C. Chen, "Scalable submicrometer additive manufacturing", Science **366**, 105–109 (2019) (cited on page 42).

[117] B. Jiao, F. Chen, Y. Liu, X. Fan, S. Zeng, Q. Dong, L. Deng, H. Gao, and W. Xiong, "Acousto-optic scanning spatial-switching multiphoton lithography", International Journal of Extreme Manufacturing **5**, 035008 (2023) (cited on page 42).

[118] W. Ouyang, X. Xu, W. Lu, N. Zhao, F. Han, and S.-C. Chen, "Ultrafast 3D nanofabrication via digital holography", Nature Communications **14**, 1716 (2023) (cited on page 42).

[119] L. Flamigni, F. Barigelletti, S. Dellonte, and G. Orlandi, "Photophysical properties of benzil in solution: triplet state deactivation pathways", Journal of Photochemistry **21**, 237–244 (1983) (cited on pages 44, 45).

[120] Q. Shen and K. Hagen, "Gas-phase molecular structure and conformation of benzil as determined by electron diffraction", The Journal of Physical Chemistry **91**, 1357–1360 (1987) (cited on page 43).

[121] D. J. Morantz and A. J. C. Wright, "Structures of the Excited States of Benzil and Related Dicarbonyl Molecules", The Journal of Chemical Physics **54**, 692–697 (1971) (cited on pages 44, 45).

[122] H. L. Bäckström and K. Sandros, "Transfer of Triplet State Energy in Fluid Solutions. I. Sensitized Phosphorescence and Its Application to the Determination of Triplet State Lifetimes.", Acta Chemica Scandinavica **14**, 48–62 (1960) (cited on page 44).

[123] T.-S. Fang, R. E. Brown, C. L. Kwan, and L. A. Singer, "Photophysical studies on benzil. Time resolution of the prompt and delayed emissions and a photokinetic study indicating deactivation of the triplet by reversible exciplex formation", The Journal of Physical Chemistry **82**, 2489–2496 (1978) (cited on page 45).

[124] A. A. Lamola and G. S. Hammond, "Mechanisms of Photochemical Reactions in Solution. XXXIII. Intersystem Crossing Efficiencies", The Journal of Chemical Physics **43**, 2129–2135 (1965) (cited on page 45).

[125] C. Parker and T. A. Joyce, "Activation-controlled delayed fluorescence of benzil", Chemical Communications (London), 1421–1422 (1968) (cited on page 45).

[126] S. P. McGlynn, T. Azumi, and M. Kinoshita, *Molecular spectroscopy of the triplet state*, pp. 241 ff. (Prentice-Hall, Englewood Cliffs, NJ, 1969) (cited on page 45).

[127] T. Cáceres, M. Encinas, and E. Lissi, "Photocleavage of benzil", Journal of Photochemistry **27**, 109–114 (1984) (cited on page 45).

[128] W. G. McGimpsey and J. C. Scaiano, "A two-photon study of the "reluctant" Norrish type I reaction of benzil", Journal of the American Chemical Society **109**, 2179–2181 (1987) (cited on page 45).

[129] M. Mukai, S. Yamauchi, and N. Hirota, "A time-resolved EPR study of one- and two-photon processes in the photochemical reactions of benzil", The Journal of Physical Chemistry **93**, 4411–4413 (1989) (cited on pages 45, 46).

[130] H. L. Bäckström, K. Sandros, H. Haraldsen, A. Grönvall, B. Zaar, and E. Diczfalusy, "The quenching of the long-lived fluorescence of biacetyl in solutions", Acta Chemica Scandinavica **12**, 823–832 (1958) (cited on page 46).

[131] T. Messer, M. Hippe, J. Gao, A. Naber, and M. Wegener, "A shoe-box-sized 3D laser nanoprinter based on two-step absorption", Light: Advanced Manufacturing **5**, 269-276 (2024) (cited on pages 46, 51, 52, 57, 59, 60, 63, 66, 67, 71–73).

[132] N. M. Bojanowski, A. Vranic, V. Hahn, P. Rietz, T. Messer, J. Brückel, C. Barner-Kowollik, E. Blasco, S. Bräse, and M. Wegener, "Search for Alternative Two-Step-Absorption Photoinitiators for 3D Laser Nanoprinting", Advanced Functional Materials **33**, 2212482 (2023) (cited on page 46).

[133] M. Jeudy and J. Robillard, "Spectral photosensitization of a variable index material for recording phase holograms with high efficiency", Optics Communications **13**, 25–28 (1975) (cited on page 46).

[134] Y. Kobayashi, K. Mutoh, and J. Abe, "Stepwise two-photon absorption processes utilizing photochromic reactions", Journal of Photochemistry and Photobiology C: Photochemistry Reviews **34**, 2–28 (2018) (cited on page 46).

[135] T. F. Scott, B. A. Kowalski, A. C. Sullivan, C. N. Bowman, and R. R. McLeod, "Two-Color Single-Photon Photoinitiation and Photoinhibition for Subdiffraction Photolithography", Science **324**, 913–917 (2009) (cited on page 46).

[136] N. Liaros and J. T. Fourkas, "Ten years of two-color photolithography", Opt. Mater. Express **9**, 3006–3020 (2019) (cited on page 46).

[137] M. P. de Beer, H. L. van der Laan, M. A. Cole, R. J. Whelan, M. A. Burns, and T. F. Scott, "Rapid, continuous additive manufacturing by volumetric polymerization inhibition patterning", Science Advances **5**, eaau8723 (2019) (cited on page 46).

[138] H. L. van der Laan, M. A. Burns, and T. F. Scott, "Volumetric Photopolymerization Confinement through Dual-Wavelength Photoinitiation and Photoinhibition", ACS Macro Letters **8**, 899–904 (2019) (cited on page 46).

[139] W. K. Swainson, *Method, medium and apparatus for producing three-dimensional figure product*, US Patent 4,041,476, 1977 (cited on page 46).

[140] Y. Kobayashi, K. Mutoh, and J. Abe, "Fast Photochromic Molecules toward Realization of Photosynergetic Effects", The Journal of Physical Chemistry Letters **7**, 3666–3675 (2016) (cited on page 47).

[141] B. E. Saleh and M. C. Teich, *Fundamentals of photonics* (John Wiley & Sons, 2019) (cited on page 47).

[142] Q. Zhang, A. Boniface, V. K. Parashar, M. A. M. Gijs, and C. Moser, "Multi-photon polymerization using upconversion nanoparticles for tunable feature-size printing", Nanophotonics **12**, 1527–1536 (2023) (cited on page 47).

[143] D. K. Limberg, J.-H. Kang, and R. C. Hayward, "Triplet–Triplet Annihilation Photopolymerization for High-Resolution 3D Printing", Journal of the American Chemical Society **144**, 5226–5232 (2022) (cited on page 47).

[144] K. Ikuta, S. Maruo, and S. Kojima, "New micro stereo lithography for freely movable 3D micro structure-super IH process with submicron resolution", in Proceedings MEMS 98. IEEE. Eleventh Annual International Workshop on Micro Electro Mechanical Systems. An Investigation of Micro Structures, Sensors, Actuators, Machines and Systems (Cat. No.98CH36176 (1998), pp. 290–295 (cited on page 47).

[145] M. T. Do, T. T. N. Nguyen, Q. Li, H. Benisty, I. Ledoux-Rak, and N. D. Lai, "Submicrometer 3D structures fabrication enabled by one-photon absorption direct laser writing", Opt. Express **21**, 20964–20973 (2013) (cited on page 47).

[146] S.-H. Hsu, T. Chi, J. Kim, P. Somers, B. W. Boudouris, X. Xu, and L. Pan, "High-Speed One-Photon 3D Nanolithography Using Controlled Initiator Depletion and Inhibitor Transport", Advanced Optical Materials **10**, 2102262 (2022) (cited on page 47).

[147] A. A. Bergh, "Blue laser diode (LD) and light emitting diode (LED) applications", physica status solidi (a) **201**, 2740–2754 (2004) (cited on page 52).

[148] K.-S. Kim, S.-H. Lee, and C. C. Chung, "A Survey of Control Issues in Optical Data Storage Systems", IFAC Proceedings Volumes **44**, 854–868 (2011) (cited on page 52).

[149] A. K. Maini, *Lasers and optoelectronics: fundamentals, devices and applications* (John Wiley & Sons, 2013) (cited on page 52).

[150] T.-J. Chang, L. Vaut, M. Voss, O. Ilchenko, L. H. Nielsen, A. Boisen, and E.-T. Hwu, "Micro and nanoscale 3D printing using optical pickup unit from a gaming console", Communications Physics **4**, 23 (2021) (cited on page 52).

[151] H.-W. Kang, Y.-S. Jeong, S.-J. Lee, K.-S. Kim, and W.-S. Yun, "Development of a compact micro-stereolithography (MSTL) system using a Blu-ray optical pickup unit", Journal of Micromechanics and Microengineering **22**, 115021 (2012) (cited on page 52).

[152] C. A. Rothenbach and M. C. Gupta, "High resolution, low cost laser lithography using a Blu-ray optical head assembly", Optics and Lasers in Engineering **50**, 900–904 (2012) (cited on page 52).

[153] Y.-C. Lee, S. Chao, C.-C. Huang, and K.-C. Cheng, "A compact optical pickup head in blue wavelength with high horizontal stability for laser thermal lithography", Opt. Express **21**, 23556–23567 (2013) (cited on page 52).

[154] Y.-C. Lee and S. Chao, "A compact and low-cost optical pickup head-based optical microscope", IEEE transactions on magnetics **50**, 1–4 (2014) (cited on page 52).

[155] A. Ulčinas, L. M. Picco, M. Berry, J. Heinrich Hörber, and M. J. Miles, "Detection and photothermal actuation of microcantilever oscillations in air and liquid using a modified DVD optical pickup", Sensors and Actuators A: Physical **248**, 6–9 (2016) (cited on page 52).

[156] E. E.-T. Hwu and A. Boisen, "Hacking CD/DVD/Blu-ray for Biosensing", ACS Sensors **3**, 1222–1232 (2018) (cited on page 52).

[157] Y. C. Cho and S. I. Ahn, "Fabricating a Raman spectrometer using an optical pickup unit and pulsed power", Scientific reports **10**, 11692 (2020) (cited on page 52).

[158] H. Tobón-Maya, A. Gómez-Ramírez, C. Buitrago-Duque, and J. Garcia-Sucerquia, "Adapting a Blu-ray optical pickup unit as a point source for digital lensless holographic microscopy", Appl. Opt. **62**, D39–D47 (2023) (cited on page 52).

[159] Blu-ray Disc Association, "White Paper Blu-Ray Disc (TM) Format - Physical Format Specifications for BD-ROM", 1–48 (2010) (cited on page 52).

[160] Thorlabs, *Collimation Tutorial - Choosing a Collimation Lens for Your Laser Diode*, (1999-2023) https://www.thorlabs.com/newgrouppage9.cfm?objectgroup_id=5260 (cited on page 53).

[161] Mirrorcle Technologies, *MEMS Mirrors*, (2023) https://www.mirrorcletech.com/wp/products/mems-mirrors/ (cited on page 55).

[162] Mirrorcle Technologies, *Integrated MEMS Mirrors*, (2023) https://www.mirrorcletech.com/wp/products/mems-mirrors/dual/integrated/ (cited on page 56).

[163] J. Fischer, "Three-Dimensional Optical Lithography beyond the Diffraction Limit", PhD thesis (Karlsruher Institut für Technologie (KIT), Karlsruhe, 2012), 141 pp. (cited on pages 58, 98).

[164] B. Richards and E. Wolf, "Electromagnetic diffraction in optical systems, II. Structure of the image field in an aplanatic system", Proceedings of the Royal Society of London. Series A. Mathematical and Physical Sciences **253**, 358–379 (1959) (cited on pages 59, 60).

[165] J. Gao, *On improving printing capabilities of two-step 3D laser nanoprinting*, Master thesis, Karlsruher Institut für Technologie (KIT), Karlsruhe, 2023 (cited on pages 61, 62).

[166] T. Frenzel, M. Kadic, and M. Wegener, "Three-dimensional mechanical metamaterials with a twist", Science **358**, 1072–1074 (2017) (cited on pages 65, 66).

[167] #3DBenchy, https://www.3dbenchy.com/ (cited on pages 65, 66).

[168] M. Malinauskas, A. Žukauskas, S. Hasegawa, Y. Hayasaki, V. Mizeikis, R. Buividas, and S. Juodkazis, "Ultrafast laser processing of materials: from science to industry", Light: Science & Applications **5**, e16133–e16133 (2016) (cited on page 72).

[169] K. Ho, C. Chan, C. Soukoulis, R. Biswas, and M. Sigalas, "Photonic band gaps in three dimensions: New layer-by-layer periodic structures", Solid State Communications **89**, 413–416 (1994) (cited on page 73).

[170] T. Gissibl, S. Thiele, A. Herkommer, and H. Giessen, "Sub-micrometre accurate free-form optics by three-dimensional printing on single-mode fibres", Nature Communications **7**, 11763 (2016) (cited on page 74).

[171] T. Gissibl, S. Thiele, A. Herkommer, and H. Giessen, "Two-photon direct laser writing of ultracompact multi-lens objectives", Nature photonics **10**, 554–560 (2016) (cited on page 74).

[172] S. Thiele, K. Arzenbacher, T. Gissibl, H. Giessen, and A. M. Herkommer, "3D-printed eagle eye: Compound microlens system for foveated imaging", Science Advances **3**, e1602655 (2017) (cited on page 74).

[173] P.-I. Dietrich, M. Blaicher, I. Reuter, M. Billah, T. Hoose, A. Hofmann, C. Caer, R. Dangel, B. Offrein, U. Troppenz, et al., "In situ 3D nanoprinting of free-form coupling elements for hybrid photonic integration", Nature Photonics **12**, 241–247 (2018) (cited on page 74).

[174] B. Li, C. Liao, Z. Cai, J. Zhou, C. Zhao, L. Jing, J. Wang, C. Xiong, L. Xu, Y. Wang, and Y. Wang, "Femtosecond laser 3D printed micro objective lens for ultrathin fiber endoscope", Fundamental Research, in press, doi:10.1016/j.fmre.2022.05.026 (2022) (cited on page 74).

[175] I. Gibson, D. W. Rosen, B. Stucker, and M. Khorasani, *Additive manufacturing technologies*, Vol. 17 (Springer, 2021), 685 pp. (cited on page 80).

[176] A. Gebhardt, *Understanding additive manufacturing* (Hanser publications Munich, Germany, 2011), 173 pp. (cited on page 80).

[177] V. Hahn and M. Wegener, *Comparing 3D Printers*, (2023) https://3dprintingspeed.aph.kit.edu (cited on page 80).

[178] T. Baldacchini, *Three-dimensional microfabrication using two-photon polymerization: fundamentals, technology, and applications* (William Andrew, 2015), 486 pp. (cited on page 80).

[179] J. Stampfl, R. Liska, and A. Ovsianikov, *Multiphoton lithography: Techniques, materials, and applications* (John Wiley & Sons, 2016), 386 pp. (cited on page 80).

[180] M. M. Zieger, P. Müller, E. Blasco, C. Petit, V. Hahn, L. Michalek, H. Mutlu, M. Wegener, and C. Barner-Kowollik, "A Subtractive Photoresist Platform for Micro- and Macroscopic 3D Printed Structures", Advanced Functional Materials **28**, 1801405 (2018) (cited on page 80).

[181] D. Gräfe, A. Wickberg, M. M. Zieger, M. Wegener, E. Blasco, and C. Barner-Kowollik, "Adding chemically selective subtraction to multi-material 3D additive manufacturing", Nature communications **9**, 2788 (2018) (cited on page 80).

[182] M. Malinauskas, S. Rekštytė, L. Lukoševičius, S. Butkus, E. Balčiūnas, M. Pečiukaitytė, D. Baltriukienė, V. Bukelskienė, A. Butkevičius, P. Kucevičius, V. Rutkūnas, and S. Juodkazis, "3D Microporous Scaffolds Manufactured via Combination of Fused Filament Fabrication and Direct Laser Writing Ablation", Micromachines **5**, 839–858 (2014) (cited on page 80).

[183] C. Liao, W. Anderson, F. Antaw, and M. Trau, "Maskless 3D Ablation of Precise Microhole Structures in Plastics Using Femtosecond Laser Pulses", ACS Applied Materials & Interfaces **10**, 4315–4323 (2018) (cited on page 80).

[184] W. Xiong, L. Jiang, T. Baldacchini, and Y. Lu, "9 - Laser additive manufacturing using nanofabrication by integrated two-photon polymerization and multiphoton ablation", in *Laser Additive Manufacturing*, edited by M. Brandt, Woodhead Publishing Series in Electronic and Optical Materials (Woodhead Publishing, 2017), pp. 237–256 (cited on page 80).

[185] J. Jiang, X. Tong, D. Morris, and Y. Zhao, "Toward Photocontrolled Release Using Light-Dissociable Block Copolymer Micelles", Macromolecules **39**, 4633–4640 (2006) (cited on page 80).

[186] D. Saran and D. H. Burke, "A Versatile Photocleavable Bifunctional Linker for Facile Synthesis of Substrate-DNA Conjugates for the Selection of Nucleic Acid Catalysts", Bioconjugate Chemistry **18**, 275–279 (2007) (cited on page 80).

[187] J. A. Johnson, M. G. Finn, J. T. Koberstein, and N. J. Turro, "Synthesis of Photocleavable Linear Macromonomers by ATRP and Star Macromonomers by a Tandem ATRP-Click Reaction: Precursors to Photodegradable Model Networks", Macromolecules **40**, 3589–3598 (2007) (cited on page 80).

[188] S. M. Jay and W. M. Saltzman, "Shining light on a new class of hydrogels", Nature biotechnology **27**, 543–544 (2009) (cited on page 80).

[189] A. M. Kloxin, M. W. Tibbitt, and K. S. Anseth, "Synthesis of photodegradable hydrogels as dynamically tunable cell culture platforms", Nature protocols **5**, 1867–1887 (2010) (cited on page 80).

[190] A. Shigenaga, J. Yamamoto, Y. Sumikawa, T. Furuta, and A. Otaka, "Development and photo-responsive peptide bond cleavage reaction of two-photon near-infrared excitation-responsive peptide", Tetrahedron Letters **51**, 2868–2871 (2010) (cited on page 80).

[191] J. A. Johnson, Y. Y. Lu, A. O. Burts, Y.-H. Lim, M. G. Finn, J. T. Koberstein, N. J. Turro, D. A. Tirrell, and R. H. Grubbs, "Core-Clickable PEG-Branch-Azide Bivalent-Bottle-Brush Polymers by ROMP: Grafting-Through and Clicking-To", Journal of the American Chemical Society **133**, 559–566 (2011) (cited on page 80).

[192] H. Zhao, E. S. Sterner, E. B. Coughlin, and P. Theato, "o-Nitrobenzyl Alcohol Derivatives: Opportunities in Polymer and Materials Science", Macromolecules **45**, 1723–1736 (2012) (cited on pages 80, 81).

[193] R. Batchelor, T. Messer, M. Hippler, M. Wegener, C. Barner-Kowollik, and E. Blasco, "Two in One: Light as a Tool for 3D Printing and Erasing at the Microscale", Advanced Materials **31**, 1904085 (2019) (cited on pages 81, 84, 86–88, 90).

[194] N. Moszner, F. Zeuner, I. Lamparth, and U. K. Fischer, "Benzoylgermanium Derivatives as Novel Visible-Light Photoinitiators for Dental Composites", Macromolecular Materials and Engineering **294**, 877–886 (2009) (cited on page 81).

[195] A. S. Quick, H. Rothfuss, A. Welle, B. Richter, J. Fischer, M. Wegener, and C. Barner-Kowollik, "Fabrication and Spatially Resolved Functionalization of 3D Microstructures via Multiphoton-Induced Diels–Alder Chemistry", Advanced Functional Materials **24**, 3571–3580 (2014) (cited on page 82).

[196] J. Fischer, J. B. Müller, A. S. Quick, J. Kaschke, C. Barner-Kowollik, and M. Wegener, "Exploring the Mechanisms in STED-Enhanced Direct Laser Writing", Advanced Optical Materials **3**, 221–232 (2015) (cited on page 82).

[197] I. Aujard, C. Benbrahim, M. Gouget, O. Ruel, J.-B. Baudin, P. Neveu, and L. Jullien, "o-Nitrobenzyl Photolabile Protecting Groups with Red-Shifted Absorption: Syntheses and Uncaging Cross-Sections for One- and Two-Photon Excitation", Chemistry – A European Journal **12**, 6865–6879 (2006) (cited on page 85).

[198] C. A. DeForest and K. S. Anseth, "Photoreversible patterning of biomolecules within click-based hydrogels", Angewandte Chemie **124**, 1852–1855 (2012) (cited on page 85).

[199] M. Lunzer, L. Shi, O. G. Andriotis, P. Gruber, M. Markovic, P. J. Thurner, D. Ossipov, R. Liska, and A. Ovsianikov, "A Modular Approach to Sensitized Two-Photon Patterning of Photodegradable Hydrogels", Angewandte Chemie International Edition **57**, 15122–15127 (2018) (cited on page 85).

[200] F. Mayer, S. Richter, J. Westhauser, E. Blasco, C. Barner-Kowollik, and M. Wegener, "Multimaterial 3D laser microprinting using an integrated microfluidic system", Science Advances **5**, eaau9160 (2019) (cited on page 88).

[201] G. E. Moore, "Cramming more components onto integrated circuits", Proceedings of the IEEE **86**, 82–85 (1998) (cited on page 96).

[202] G. O'Sullivan, B. Li, R. D'Arcy, P. Dunne, P. Hayden, D. Kilbane, T. McCormack, H. Ohashi, F. O'Reilly, P. Sheridan, E. Sokell, C. Suzuki, and T. Higashiguchi, "Spectroscopy of highly charged ions and its relevance to EUV and soft x-ray source development", Journal of Physics B: Atomic, Molecular and Optical Physics **48**, 144025 (2015) (cited on page 96).

[203] D. Bratton, D. Yang, J. Dai, and C. K. Ober, "Recent progress in high resolution lithography", Polymers for Advanced Technologies **17**, 94–103 (2006) (cited on page 96).

[204] C. Chang and A. Sakdinawat, "Ultra-high aspect ratio high-resolution nanofabrication for hard X-ray diffractive optics", Nature communications **5**, 4243 (2014) (cited on page 96).

[205] U. T. Sanli, C. Jiao, M. Baluktsian, C. Grévent, K. Hahn, Y. Wang, V. Srot, G. Richter, I. Bykova, M. Weigand, G. Schütz, and K. Keskinbora, "3D Nanofabrication of High-Resolution Multilayer Fresnel Zone Plates", Advanced Science **5**, 1800346 (2018) (cited on page 96).

[206] D. Attwood, *Soft x-rays and extreme ultraviolet radiation: principles and applications* (Cambridge University Press, 2000), 470 pp. (cited on pages 96, 97).

[207] L. B. Lesem, P. M. Hirsch, and J. A. Jordan, "The Kinoform: A New Wavefront Reconstruction Device", IBM Journal of Research and Development **13**, 150–155 (1969) (cited on page 96).

[208] D. A. Buralli, G. M. Morris, and J. R. Rogers, "Optical performance of holographic kinoforms", Appl. Opt. **28**, 976–983 (1989) (cited on page 96).

[209] U. T. Sanli, H. Ceylan, I. Bykova, M. Weigand, M. Sitti, G. Schütz, and K. Keskinbora, "3D Nanoprinted Plastic Kinoform X-Ray Optics", Advanced Materials **30**, 1802503 (2018) (cited on page 97).

[210] B. Morgan, C. Waits, J. Krizmanic, and R. Ghodssi, "Development of a deep silicon phase Fresnel lens using Gray-scale lithography and deep reactive ion etching", Journal of Microelectromechanical Systems **13**, 113–120 (2004) (cited on page 99).

[211] A. Schropp, R. Hoppe, J. Patommel, D. Samberg, F. Seiboth, S. Stephan, G. Wellenreuther, G. Falkenberg, and C. G. Schroer, "Hard x-ray scanning microscopy with coherent radiation: Beyond the resolution of conventional x-ray microscopes", Applied Physics Letters **100**, 253112 (2012) (cited on page 100).

[212] K. Keskinbora, C. Grévent, M. Hirscher, M. Weigand, and G. Schütz, "Single-Step 3D Nanofabrication of Kinoform Optics via Gray-Scale Focused Ion Beam Lithography for Efficient X-Ray Focusing", Advanced Optical Materials **3**, 792–800 (2015) (cited on page 102).

[213] M. T. Raimondi, M. M. Nava, S. M. Eaton, A. Bernasconi, K. C. Vishnubhatla, G. Cerullo, and R. Osellame, "Optimization of Femtosecond Laser Polymerized Structural Niches to Control Mesenchymal Stromal Cell Fate in Culture", Micromachines **5**, 341–358 (2014) (cited on page 102).

[214] M. Schmid, D. Ludescher, and H. Giessen, "Optical properties of photoresists for femtosecond 3D printing: refractive index, extinction, luminescence-dose dependence, aging, heat treatment and comparison between 1-photon and 2-photon exposure", Opt. Mater. Express **9**, 4564–4577 (2019) (cited on page 102).

[215] G. Flamourakis, A. Kordas, G. D. Barmparis, A. Ranella, and M. Farsari, "Low-autofluorescence, transparent composite for multiphoton 3D printing", Opt. Mater. Express **11**, 801–813 (2021) (cited on page 102).

[216] Nanoscribe GmbH, *New IP-Visio photoresin*, (2023) https://www.nanoscribe.com/en/products/ip-photoresins/ip-visio/ (cited on page 102).

Acknowledgments

Such a work is not the achievement of a single person. Thus, I would like to take the chance to thank all the people that have contributed to this thesis in various ways.

First, I want to thank Prof. Dr. Martin Wegener for the opportunity to join his group for this exciting research. His support has been outstanding throughout the years. I would also like to thank for the opportunities we got to present our work on international conferences. Furthermore, he enabled my participation in the two graduate schools Karlsruhe School of Optics and Photonics (KSOP) and the cluster of excellence "3D Matter Made to Order" which was time consuming but led to many great collaborations, discussions, and even friends, thus being more than worth it. Both institutions also granted funding during my thesis.

Second, I want to thank Prof. Dr. Eva Blasco for kindly agreeing to co-referee my thesis. Beyond that, I am incredibly grateful for the continuous collaboration on the chemistry related topics and that I could learn a lot from her chemical expertise – back at the beginning even lots of hours together in the lab.

Further, I want to explicitly thank all my collaborators I had the opportunity to work with on various challenging but great projects. Starting in the early days with Dr. Sabrina Bialas and Dr. Rhiannon Batchelor with whom I had the pleasure to conduct the first projects on novel material systems. I would like to gratefully thank Dr. Vincent Hahn not only as a scientific collaborator but even more for all the fruitful discussions and for sharing his outstanding knowledge. It was a great pleasure to share office throughout the years and work on different projects. Further, I want to thank Dr. Marc Hippler for sharing all his expertise at the LSM and AFM and the great input he always had at hand. Next, I would like to thank Dr. Christian Kern for the many discussions and his continuous advice within our collaboration and beyond. I want to thank Dr. Umut Sanli for the nice collaboration on laser printed kinoforms. In addition, I thank Tobias Abele for the enjoyable time we always had during our collaboration which led to such a nice result. Finally, I thank Dr. Maximilian Bojanowski, Anna Mauri, Dr. Mariana Kozlowska, and Dr. Saskia Braun for further great collaborations. I learned a lot about the chemistry and processes of two-photon absorption in our discussions. I would particularly like to thank Michael Hippe for all the discussions and his outstanding involvement in my last project of the PhD.

Maybe most importantly, I would like to show my gratitude to everyone I could work with on a daily basis at the Institute of Applied Physics. Former members

starting back in 2014, as well as the more recent members of the group. I always had an enjoyable time with you. Out of the more recent members I especially thank Dr. Patrick Müller, Dr. Tobias Frenzel, Dr. Andreas Niemeyer, Dr. Julian Köpfler, Dr. Alexander Münchinger, Pascal Kiefer, Sebastian Kalt, and Pascal Rietz to whom I was closest besides the ones already listed as collaborators. It was always a great pleasure to work with everyone in the group and was definitely one of the decisive factors to stay within the group for all my theses over the years.

Furthermore, I want to thank Philipp Ohl and Julian Haarer as well as Lilyn Gao for their enthusiasm they put in during their Bachelor and Master theses, respectively. In this context, I would also like to thank PD Dr. Andreas Naber for his help during the thesis of Philipp Ohl. Without his help, this project would have not come to the successful result. He wrote the initial microcontroler code for steering the MEMS scanner which served as the basis for Michael Hippe's work on the later program for the shoe-box 3D laser printer control.

Additionally, I thank all people working in the background. Therefore, I want to thank our technician Johann Westhauser, Werner Gilde and Helmut Lay from the electronics workshop, Maik Nothdurft and Mario Nusche from the mechanical workshop for all their work and grateful discussions on the self-made stage, Melissa Baumgärtner from the carpenter's workshop, and Petra Bauer and Gloria Zanda from the secretary to handle German bureaucracy.

I am also thankful to everybody, who went through the critically proofreading of this thesis, especially standing at my side in this final and exhausting stage of my thesis. Namely, these are Samantha Catt, Sebastian Kalt, Michael Messer, Andreas Niemeyer, and Pascal Rietz in the alphabetic order.

Finally, I want to express my deepest gratitude to my family and friends for their limitless support. You all contributed to what I am today.